| REPORT DOCUMENTATION PAGE | | Form Approved OMB NO. 0704-0188 |
|---|---|---|

The public reporting burden for this collection of information is estimated to average 1 hour per response, including the time for reviewing instructions, searching existing data sources, gathering and maintaining the data needed, and completing and reviewing the collection of information. Send comments regarding this burden estimate or any other aspect of this collection of information, including suggesstions for reducing this burden, to Washington Headquarters Services, Directorate for Information Operations and Reports, 1215 Jefferson Davis Highway, Suite 1204, Arlington VA, 22202-4302. Respondents should be aware that notwithstanding any other provision of law, no person shall be subject to any oenalty for failing to comply with a collection of information if it does not display a currently valid OMB control number.
PLEASE DO NOT RETURN YOUR FORM TO THE ABOVE ADDRESS.

| 1. REPORT DATE (DD-MM-YYYY) 19-08-2014 | 2. REPORT TYPE Final Report | 3. DATES COVERED (From - To) 15-Sep-2011 - 14-Sep-2014 |
|---|---|---|

| 4. TITLE AND SUBTITLE Globally Convergent Methods for Solving Coefficient Inverse Problems for Time Dependent Maxwell Equations | 5a. CONTRACT NUMBER W911NF-11-1-0399 |
|---|---|
| | 5b. GRANT NUMBER |
| | 5c. PROGRAM ELEMENT NUMBER 611102 |
| 6. AUTHORS Michael V. Klibanov | 5d. PROJECT NUMBER |
| | 5e. TASK NUMBER |
| | 5f. WORK UNIT NUMBER |

| 7. PERFORMING ORGANIZATION NAMES AND ADDRESSES University of North Carolina - Charlotte 9201 University City Boulevard Charlotte, NC          28223 -0001 | 8. PERFORMING ORGANIZATION REPORT NUMBER |
|---|---|

| 9. SPONSORING/MONITORING AGENCY NAME(S) AND ADDRESS (ES) U.S. Army Research Office P.O. Box 12211 Research Triangle Park, NC 27709-2211 | 10. SPONSOR/MONITOR'S ACRONYM(S) ARO |
|---|---|
| | 11. SPONSOR/MONITOR'S REPORT NUMBER(S) 60035-MA.35 |

12. DISTRIBUTION AVAILIBILITY STATEMENT

Approved for Public Release; Distribution Unlimited

13. SUPPLEMENTARY NOTES
The views, opinions and/or findings contained in this report are those of the author(s) and should not contrued as an official Department of the Army position, policy or decision, unless so designated by other documentation.

14. ABSTRACT

   This is an interdisciplinary project. The main results of the project are:

1.The analytical proof of the global convergence property using a sophisticated mathematical apparatus.

2.The development of a sophisticated analytical apparatus for establishing the relaxation property of the adaptivity technique.

15. SUBJECT TERMS

coefficient inverse problems, globally convergent numerical methods, adaptive finite element method, performance verification on experimental data, imaging of explosive devices, comparison with the classical Krein equation method, working with experimental

| 16. SECURITY CLASSIFICATION OF: | | | 17. LIMITATION OF ABSTRACT | 15. NUMBER OF PAGES | 19a. NAME OF RESPONSIBLE PERSON Michael Klibanov |
|---|---|---|---|---|---|
| a. REPORT UU | b. ABSTRACT UU | c. THIS PAGE UU | UU | | 19b. TELEPHONE NUMBER 704-687-2645 |

**Report Title**

Globally Convergent Methods for Solving Coefficient Inverse Problems for Time Dependent Maxwell Equations

**ABSTRACT**

This is an interdisciplinary project. The main results of the project are:

1.The analytical proof of the global convergence property using a sophisticated mathematical apparatus.

2.The development of a sophisticated analytical apparatus for establishing the relaxation property of the adaptivity technique.

3.Numerical implementations of resulting algorithms.

4.Numerical verifications of resulting algorithms on computationally simulated data.

5.Assembling an experimental apparatus in Microwave Laboratory of University of North Carolina at Charlotte.

6.Verification of the globally convergent numerical method on backscattering experimental data for targets standing in air. Targets mimic explosives.

7.Verification of the globally convergent numerical method on backscattering experimental data for targets buried in the ground. This case is much more complicated than the case of targets in air.

8.An experimental and numerical reconstruction evidence of the super resolution phenomenon.

9.Addressing a need of the Army via successful work with experimental data collected by the Forward Looking Radar of US Army Research Laboratory (ARL). The globally convergent method of this project was used.

10.Transfer of a ready-to-use software to ARL resulting from item #9. This software works with the real data of the Forward Looking Radar of ARL.

11.The use of experimental data of item #9 for a comparison of performances of the globally convergent numerical method of this project and the classical Krein equation method. It was established that while the first method works well, the second one fails for these data.

12.Four (4) presentations to Mr. Brian Burns, Drs. Anders Sullivan and Lam Nguyen, ARL engineers, and to Dr. Joseph D. Myers, the Program Manager of the Numerical Analysis Program of ARO.

13.Three joint publications with ARL engineers Drs. Anders Sullivan and Lam Nguyen.

14.A new globally convergent numerical method based on the Carleman Weight Function.

15.The first solution of a long standing problem about uniqueness of a phaseless 3-d inverse problem of quantum scattering. This was an open question since the publication in 1977 of the well known book of K. Chadan and P. Sabatier "Inverse Problems in Quantum Scattering Theory", Springer, New York.

16.Publication of a book summarizing some results of the project up to 2012. This book was published by Springer, the World most prestigious publisher of the scientific literature.

17.Publication of twenty two papers. Two of them are survey papers.

The target application of this project is in the standoff detection and identification of explosives, such as IEDs and antipersonnel land mines, using electric signals propagations. The numerical methods developed in this project use experimental data to image both dielectric constants and shapes of small inclusions buried in a sand box. Inclusions mimic explosives. A systematic study of twenty five cases was performed.

Conventional least squares cost functionals for solving Coefficient Inverse Problems (CIPs) face the fundamental obstacle: the phenomenon of multiple local minima and ravines. This results, in turn in the local convergence of conventional numerical methods for CIPs. Therefore, the following question is both the most crucial and the most challenging one in a numerical treatment of any CIP: How to rigorously obtain a good approximation for the unknown coefficient without any advanced knowledge of a small neighborhood of the solution? A numerical method providing such an approximation is called globally convergent. As soon as this approximation is found, some conventional locally convergent numerical methods can be used as refinement tools.

This project has been focused on the development of a globally convergent numerical method for a hyperbolic CIP. The crucial advantage of this method is that it does not need a good first guess for the solution, unlike all existing ones. Both analytical and numerical issues were addressed. It was observed that the best is a two-stage numerical procedure: On the first stage the globally convergent numerical method delivers a good approximation for the solution. And on the second stage the adaptivity technique refines the solution obtained on the first stage.

**Enter List of papers submitted or published that acknowledge ARO support from the start of the project to the date of this printing. List the papers, including journal references, in the following categories:**

**(a) Papers published in peer-reviewed journals (N/A for none)**

<u>Received</u>    <u>Paper</u>

01/28/2013 13.00  Michael V. Klibanov. Thermoacoustic tomography with an arbitrary elliptic operator,
Inverse Problems,  (02 2013): 1. doi:

02/21/2014 24.00  Michael Klibanov, Michael Fiddy, Nguyen Thanh, Larisa Beilina. Reconstruction from blind experimental data for an inverse problem for a hyperbolic equation,
Inverse Problems,  (02 2014): 1. doi:

02/27/2013 15.00  Larisa Beilina, Michael V. Klibanov. Relaxation property for the adaptivity for ill-posed problems,
Applicable Analysis, published online of this journal, DOI: :10.1080/00036811.2013.768339,  (02 2013): 1. doi:

02/27/2013 16.00  Jianzhong Su, Michael V. Klibanov, Yueming Liu, Zhijin Lin, Natee Pantong, Hanli Liu. Optical imaging of phantoms from real data by an approximately globally convergent inverse algorithm,
Inverse Problems in Science and Engineering online, DOI:10.1080/17415977.2012.743126,  (11 2012): 1. doi:

03/30/2012  3.00  Larisa Beilina and Michael V. Klibanov. The philosophy of the approximate global convergence for multidimensional coefficient inverse problems,
Complex Variables and Elliptic Equations,  (02 2012): 0. doi:

04/10/2014 26.00  Larisa Beilina, Michael V. Klibanov. Relaxation property for the adaptivity for ill-posed problems,
Applicable Analysis,  (02 2014): 223. doi:

04/10/2014 25.00  Michael V. Klibanov. Phaseless inverse scattering problems in three dimensions,
SIAM Journal on Applied  Mathematics,  (02 2014): 392. doi:

05/08/2014 27.00  Larisa Beilina, Nguyen Trung Thành, Michael V. Klibanov, Michael A. Fiddy. Reconstruction of the refractive index from experimental backscattering data using a globally convergent inverse method,
SIAM J Scientific Computing,  (02 2014): 273. doi:

08/14/2014 30.00  Michael Klibanov. On the first solution of a long standing problem: uniqueness of thephaseless quantum inverse scattering problem in 3-d
,
Applied Mathematics Letters,  (11 2014): 82. doi:

08/24/2013 17.00  Michael V. Klibanov. Carleman estimates for global uniqueness, stability and numerical methods for coefficient inverse problems,
Journal of Inverse and Ill-Posed Problems,  (08 2013): 477. doi:

08/24/2013 18.00  Michael V. Klibanov. Uniqueness of two phaseless non-overdetermined inverse acoustics problems in 3-d
,
Applicable Analysis,  (06 2013): 0. doi:

09/06/2012  4.00  Andrey V. Kuzhuget, Larisa Beilina, Michael V. Klibanov, Anders Sullivan, Lam Nguyen. Blind experimental data collected in the field and an approximately globally convergent inverse algorithm,
Inverse Problems,  (09 2012): 1. doi:

09/06/2012  6.00  Andrey V. Kuzhuget, Larisa Beilina, Michael V. Klibanov, Anders Sullivan, Lam Nguyen, Michael A. Fiddy.
Quantitative image recovery from measured blind backscattered data using a globally convergent inverse
method,
IEEE TRANSACTIONS ON  GEOSCIENCE AND REMOTE SENSING,  (10 2012): 0. doi:

09/07/2012 11.00  Andrey V. Kuzhuget, Larisa Beilina,  Michael V. Klibanov . Approximate global convergence and quasi-
reversibility for a coefficient inverse problem with backscattering data,
Journal of Mathematical Sciences,  (02 2012): 126. doi:

10/19/2013 23.00  . Uniqueness of two phaseless non-overdetermined inverse acoustics problems,
Applicable Analysis,  (06 2013): 0. doi:

10/19/2013 22.00  Michael V. Klibanov. Carleman estimates for global uniqueness, stability and numerical methods for
coefficient inverse problems ,
Journal of Inverse and Ill-Posed Problems,  (08 2013): 477. doi:

   **TOTAL:**      **16**


**Number of Papers published in peer-reviewed journals:**

---

## (b) Papers published in non-peer-reviewed journals (N/A for none)


<u>Received</u>        <u>Paper</u>


02/22/2012  2.00  Andrey Kuzhuget, Larisa Beilina, Michael Klibanov. Approximate global convergence and
quasireversibility for a coefficient inverse problem with backscattering data,
Journal of Mathematical Sciences,  (02 2012): 0. doi:

02/27/2013 14.00  Larisa Beilina, Michael V. Klibanov. A new approximate mathematical model for global convergence for a
coefficient inverse problems with backscattering data,
Journal of Inverse and Ill-Posed Problems,  (10 2012): 513. doi:

08/15/2014 34.00  Michael Klibanov, Larisa Beilina. Globally strongly convex cost functional for a coefficient inverse problem,
Preprint,  (12 2013): 0. doi:

   **TOTAL:**      **3**


**Number of Papers published in non peer-reviewed journals:**

---

## (c) Presentations

**Number of Presentations:** 0.00

## Non Peer-Reviewed Conference Proceeding publications (other than abstracts):

Received          Paper

08/14/2014  29.00  Larisa Beilina, Nguyen Thành, Michael Klibanov , John Malmberg. Methods of quantitative reconstruction
                   of shapes and refractive indexes from experimental data,
                   Inverse Problems workshop in Gothenburg, Sweden, 2013. 04-NOV-13, . : ,

      **TOTAL:**        **1**

**Number of Non Peer-Reviewed Conference Proceeding publications (other than abstracts):**

## Peer-Reviewed Conference Proceeding publications (other than abstracts):

Received          Paper

09/06/2012   7.00  . Approximate global convergence in imagig of land mines from backscattering data,
                   Inverse Problems Conference in Chalmers University, Gothenburg, Sweden. 02-MAY-12, . : ,

09/06/2012   8.00  Larisa Beilina , Michael V. Klibanov. Adaptive FEM with relaxation for a hyperbolic coefficient inverse
                   problem,
                   Inverse Problems Conference in Chalmers University, Gothenburg, Sweden. 02-MAY-12, . : ,

      **TOTAL:**        **2**

**Number of Peer-Reviewed Conference Proceeding publications (other than abstracts):**

## (d) Manuscripts

| Received | | Paper |
|---|---|---|

08/14/2014 31.00  Nguyen Trung Thành, Larisa Beilina, Michael V. Klibanov, Michael A. Fiddy. Imaging of buried objects from experimental backscattering radar measurements using a globally convergent inverse method, Preprint (06 2014)

08/14/2014 32.00  Michael Klibanov, Nguyen Trung Thành.  Recovering of dielectric constants of explosives via a globally strictly convex cost functional, Preprint (08 2014)

08/14/2014 33.00  Larisa Beilina, Nguyen Trung Thành, Michael Klibanov, John Bondestam Malmberg. Reconstruction of shapes and refractive indices from backscattering experimental data using the adaptivity, Preprint (04 2014)

08/24/2013 19.00  . Phaseless inverse scattering problems in 3-d, ArXiv e-prints, 1303.0923 (03 2013)

08/24/2013 21.00  Larisa Beilina, Nguyen Trung Thành, Michael V. Klibanov, Michael A. Fiddy. Reconstruction from blind experimental data for an inverse problem for a hyperbolic equation, ArXiv e-prints, 13006.6874 (06 2013)

08/24/2013 20.00  Nguyen Trung Thành, Larisa Beilina, Michael V. Klibanov, Michael A. Fiddy. Reconstruction of the refractive index from experimental backscattering data using a globally convergent inverse method, ArXiv e-prints, 1306.3150 (06 2013)

09/06/2012  9.00  Michael V. Klibanov. Thermoacoustic tomography with an arbitrary elliptic operator, Inverse Problems (08 2012)

09/06/2012 10.00   M.V. Klibanov,  Y. Liu, J. Su,  Z. Lin,  N. Pantong,  H. Liu. Optical imaging of phantoms from real data by an approximately globally convergent inverse algorithm, Inverse Problems in Sience and Engineering (08 2012)

   **TOTAL:**     **8**

**Number of Manuscripts:**

## Books

| Received | | Book |
|---|---|---|

09/06/2012  5.00  Larisa Beilina, Michael V. Klibanov. Approximate Global Convergence and Adaptivity for Coefficient Inverse Problems, New York: Springer,  (04 2012)

   **TOTAL:**     **1**

<u>Received</u>      <u>Book Chapter</u>

**TOTAL:**

# Patents Submitted

# Patents Awarded

# Awards

1. Plenary speaker at the conference: "Inverse Problems Problems: Modelling and Simulation", Turkey.

2. Plenary speaker at the conference on Inverse Problems, Albi, France.

3. Plenary speaker at International Conference on Inverse Problems and Optimal Control, Hong Kong.

## Graduate Students

| NAME | PERCENT_SUPPORTED | Discipline |
|------|-------------------|------------|
| Kirill Golubnichij | 0.66 | |
| **FTE Equivalent:** | **0.66** | |
| **Total Number:** | **1** | |

## Names of Post Doctorates

| NAME | PERCENT_SUPPORTED |
|------|-------------------|
| Nguyen Trung Thanh | 0.92 |
| **FTE Equivalent:** | **0.92** |
| **Total Number:** | **1** |

## Names of Faculty Supported

| NAME | PERCENT_SUPPORTED | National Academy Member |
|------|-------------------|-------------------------|
| Michael Klibanov | 0.28 | |
| **FTE Equivalent:** | **0.28** | |
| **Total Number:** | **1** | |

## Names of Under Graduate students supported

| NAME | PERCENT_SUPPORTED |
|------|-------------------|
| **FTE Equivalent:** | |
| **Total Number:** | |

## Student Metrics
This section only applies to graduating undergraduates supported by this agreement in this reporting period

The number of undergraduates funded by this agreement who graduated during this period: ...... 0.00

The number of undergraduates funded by this agreement who graduated during this period with a degree in science, mathematics, engineering, or technology fields:······ 0.00

The number of undergraduates funded by your agreement who graduated during this period and will continue to pursue a graduate or Ph.D. degree in science, mathematics, engineering, or technology fields:······ 0.00

Number of graduating undergraduates who achieved a 3.5 GPA to 4.0 (4.0 max scale):...... 0.00

Number of graduating undergraduates funded by a DoD funded Center of Excellence grant for Education, Research and Engineering:...... 0.00

The number of undergraduates funded by your agreement who graduated during this period and intend to work for the Department of Defense ...... 0.00

The number of undergraduates funded by your agreement who graduated during this period and will receive scholarships or fellowships for further studies in science, mathematics, engineering or technology fields:...... 0.00

## Names of Personnel receiving masters degrees

| NAME |
|------|
| **Total Number:** |

## Names of personnel receiving PHDs

| NAME |
|------|
| **Total Number:** |

## Names of other research staff

| NAME | PERCENT_SUPPORTED |
|------|-------------------|
| Larisa Beilina, consultant | 0.17 |
| Steven Kitchin, engineer | 0.08 |
| **FTE Equivalent:** | **0.25** |
| **Total Number:** | **2** |

## Sub Contractors (DD882)

## Inventions (DD882)

# Scientific Progress

The main accomplishments of this project are:

1. The analytical proof of the global convergence property using a sophisticated mathematical apparatus.

2. The development of a sophisticated analytical apparatus for establishing the relaxation property of the adaptivity technique.

3. Numerical implementations of resulting algorithms.

4. Numerical verifications of resulting algorithms on computationally simulated data.

5. Assembling an experimental apparatus in Microwave Laboratory of University of North Carolina at Charlotte.

6. Verification of the globally convergent numerical method on backscattering experimental data for targets standing in air. Targets mimic explosives.

7. Verification of the globally convergent numerical method on backscattering experimental data for targets buried in the ground. This case is much more complicated than the case of targets in air.

8. An experimental and numerical reconstruction evidence of the super resolution phenomenon.

9. Addressing a need of the Army via successful work with experimental data collected by the Forward Looking Radar of US Army Research Laboratory (ARL). The globally convergent method of this project was used.

10. Transfer of a ready-to-use software to ARL resulting from item #9. This software works with the real data of the Forward Looking Radar of ARL.

11. The use of experimental data of item #9 for a comparison of performances of the globally convergent numerical method of this project and the classical Krein equation method. It was established that while the first method works well, the second one fails for these data.

12. Four (4) presentations to Mr. Brian Burns, Drs. Anders Sullivan and Lam Nguyen, ARL engineers, and to Dr. Joseph D. Myers, the Program Manager of the Numerical Analysis Program of ARO.

13. Three joint publications with ARL engineers Drs. Anders Sullivan and Lam Nguyen.

14. A new globally convergent numerical method based on the Carleman Weight Function.

15. The first solution of a long standing problem about uniqueness of a phaseless 3-d inverse problem of quantum scattering. This was an open question since the publication of the well known book of K. Chadan and P. Sabatier "Inverse Problems in Quantum Scattering Theory", Springer, New York, 1977.

16. Publication of a book summarizing some results of the project up to 2012. This book was published by Springer, the World most prestigious publisher of the scientific literature.

17. Publication of two survey papers.

# Technology Transfer

1.Addressing a need of the Army via successful work with experimental data collected by the Forward Looking Radar of US Army Research Laboratory (ARL). The globally convergent method of this project was used.

2.Transfer of a ready-to-use software to ARL resulting from item #1. This software works with the real data of the Forward Looking Radar of ARL.

3.The use of experimental data of item #1 for a comparison of performances of the globally convergent numerical method of this project and the classical Krein equation method. It was established that while the first method works well, the second one fails for these data.

4.Four presentations of results were given to Mr. Brian Burns, Drs. Anders Sullivan and Lam Nguyen, ARL engineers, and to Dr. Joseph D. Myers, the Program Manager of the Numerical Analysis Program of ARO.

5.Three joint publications with ARL engineers Drs. Anders Sullivan and Lam Nguyen.

Three joint publications with ARL engineers mentioned in item #5 are:

1. A.V. Kuzhuget, L. Beilina, M.V. Klibanov, A. Sullivan, L. Nguyen and M.A. Fiddy, Blind experimental data collected in the field and an approximately globally convergent inverse algorithm, Inverse Problems, 28, 095007, 2012.

2. A.V. Kuzhuget, L. Beilina, M.V. Klibanov, A. Sullivan, L. Nguyen and M.A. Fiddy, Quantitative image recovery from measured blind backscattered data using a globally convergent inverse method, IEEE Transactions of Geoscience and Remote Sensing, 51, 2937-2948, 2013.

3. A.L. Karchevskii, M.V. Klibanov, N. Pantong, A. Sullivan and L. Nguyen, The Krein method and the globally convergent method for experimental data, Applied Numerical Mathematics, 74, 111-127, 2013.

**Final Report on the ARO grant** W911NF-11-1-0399

**Project Title**: Globally Convergent Methods for Solving Coefficient Inverse Problems for Time Dependent Maxwell Equations

**Proposal Number**: P-60035-MA

**Principal Investigator**: Michael V. Klibanov, Department of Mathematics and Statistics, University of North Carolina at Charlotte, e-mail mklibanv@uncc.edu

**Reportage Period**: September 15, 2011-September 15, 2014

## Abstract

This is an *interdisciplinary* project. The main results of the project are:

1. The analytical proof of the global convergence property using a sophisticated mathematical apparatus.

2. The development of a sophisticated analytical apparatus for establishing the relaxation property of the adaptivity technique.

3. Numerical implementations of resulting algorithms.

4. Numerical verifications of resulting algorithms on computationally simulated data.

5. Assembling an experimental apparatus in Microwave Laboratory of University of North Carolina at Charlotte.

6. Verification of the globally convergent numerical method on backscattering experimental data for targets standing in air. Targets mimic explosives.

7. Verification of the globally convergent numerical method on backscattering experimental data for targets buried in the ground. This case is much more complicated than the case of targets in air.

8. An experimental and numerical reconstruction evidence of the super resolution phenomenon.

9. Addressing a need of the Army via successful work with experimental data collected by the Forward Looking Radar of US Army Research Laboratory (ARL). The globally convergent method of this project was used.

10. Transfer of a ready-to-use software to ARL resulting from item #9. This software works with the real data of the Forward Looking Radar of ARL.

11. The use of experimental data of item #9 for a comparison of performances of the globally convergent numerical method of this project and the classical Krein equation method. It was established that while the first method works well, the second one fails for these data.

12. Four (4) presentations to Mr. Brian Burns, Drs. Anders Sullivan and Lam Nguyen, ARL engineers, and to Dr. Joseph D. Myers, the Program Manager of the Numerical Analysis Program of ARO.

13. Three joint publications with ARL engineers Drs. Anders Sullivan and Lam Nguyen.

14. A new globally convergent numerical method based on the Carleman Weight Function.

15. The first solution of a long standing problem about uniqueness of a phaseless 3-d inverse problem of quantum scattering. This was an open question since the publication in 1977 of the well known book of K. Chadan and P. Sabatier "Inverse Problems in Quantum Scattering Theory", Springer, New York.

16. Publication of a book summarizing some results of the project. This book was published by Springer, the World most prestigious publisher of the scientific literature.

17. Publication of twenty two papers. Two of them are survey papers.

The target application of this project is in the standoff detection and identification of explosives, such as IEDs and antipersonnel land mines, using electric signals propagations. The numerical methods developed in this project use experimental data to image both dielectric constants and shapes of small inclusions buried in a sand box. Inclusions mimic explosives. A *systematic study* of twenty five cases was performed.

Conventional least squares cost functionals for solving Coefficient Inverse Problems (CIPs) face the fundamental obstacle: the phenomenon of multiple local minima and ravines. This results, in turn in the local convergence of conventional numerical methods for CIPs. Therefore, the following question is both the most crucial and the most challenging one in a numerical treatment of any CIP: *How to rigorously obtain a good approximation for the unknown coefficient without any advanced knowledge of a small neighborhood of the solution?* A numerical method providing such an approximation is called *globally convergent.* As soon as this approximation is found, some conventional locally convergent numerical methods can be used as refinement tools.

This project has been focused on the development of a globally convergent numerical method for a hyperbolic CIP. The *crucial advantage* of this method is that it does not need a good first guess for the solution, unlike all existing ones. Both analytical and numerical issues were addressed. It was observed that the best is a two-stage numerical procedure: On the first stage the globally convergent numerical method delivers a good approximation for the solution. And on the second stage the adaptivity technique refines the solution obtained on the first stage.

# Contents

# 1  Introduction

This is an *interdisciplinary* project. It combines analytical studies, studies of computationally simulated data and studies of experimental data.

The target application of this project is detection of explosives, such as IEDs, plastic antipersonnel land mines, etc. using electric signals propagations. Indeed, it is well known from tables of dielectric constants [65, 66] that dielectric constants in explosives are higher than those of regular materials. Hence, the idea is to image both dielectric constants and shapes of small sharp inclusions embedded in an otherwise slowly changing background.

Different imaging methods have been applied to this type of measurements to obtain geometrical information such as shapes, sizes and locations of the targets, see, e.g. [47]. However, the dielectric constants, which characterize the targets in terms of their constituent materials, are much more difficult to estimate. Unlike this, the globally convergent numerical method of the current project can image both dielectric constants and shapes of inclusions mimicking explosives. The *crucial advantage* of this method is that it does not need a good first guess for the solution, unlike all existing ones.

A Coefficient Inverse Problem (CIP) for a Partial Differential Equation (PDE) is a problem of the reconstruction of an unknown coefficient of that PDE from the boundary measurements. Because of many dangers on the battlefield, the Army is interested in the minimal number of measurements. Thus, only CIPs with a single measurement event are considered in this project. In other words, either a single location of the point source or a single direction of the initializing plane wave is considered. It was observed that the best is a two-stage numerical procedure:

**Stage 1**. The globally convergent method provides a good approximation for the solution without any a priori knowledge of a small neighborhood of this solution.

**Stage 2**. The locally convergent Adaptive Finite Element Method (adaptivity)

The first stage gives us accurate values of dielectric constants. The second stage provides accurate images of shapes of targets. It is important that the adaptivity uses the solution of the first stage as its starting point.

# 2  The List of Main Results Of This Project

The first paper about the globally convergent method of this paper was published in 2008 [25]. Since then the authors of [25] have developed this method much further, see items #1-6 in Introduction. Our group has pioneered all main results listed below. The main results of this project are:

1. The analytical proof of the global convergence property using a sophisticated mathematical apparatus [1, 16, 5].

2. The development of a sophisticated analytical apparatus for establishing the relaxation property of the adaptivity technique [1, 7].

5

3. Numerical implementations of resulting algorithms.

4. Numerical verifications of resulting algorithms on computationally simulated data [1, 16].

5. Assembling an experimental apparatus in Microwave Laboratory of University of North Carolina at Charlotte.

6. Verification of the globally convergent numerical method on backscattering experimental data for targets standing in air [2, 3, 4, 6]. Targets mimic explosives.

7. Verification of the globally convergent numerical method on backscattering experimental data for targets buried in the ground [5]. This case is much more complicated than the case of targets in air.

8. An experimental and numerical reconstruction evidence of the super resolution phenomenon [5].

9. Addressing a need of the Army via successful work with experimental data collected by the Forward Looking Radar of US Army Research Laboratory (ARL) [17, 18, 19]. The globally convergent method of this project was used.

10. Transfer of a ready-to-use software to ARL resulting from item #9. This software works with the real data of the Forward Looking Radar of ARL [59].

11. The use of experimental data of item #9 for a comparison of performances of the globally convergent numerical method of this project and the classical Krein equation method [19]. It was established that while the first method works well, the second one fails for these data.

12. Four (4) presentations to Mr. Brian Burns, Drs. Anders Sullivan and Lam Nguyen, ARL engineers, and to Dr. Joseph D. Myers, the Program Manager of the Numerical Analysis Program of ARO.

13. Three joint publications with ARL engineers Drs. Anders Sullivan and Lam Nguyen [17, 18, 19].

14. A new globally convergent numerical method based on the Carleman Weight Function [11].

15. The first solution of a long standing problem about uniqueness of a phaseless 3-d inverse problem of quantum scattering [8, 9, 10]. This was an open question since the publication of the well known book [38] in 1977.

16. Publication of a book summarizing some results of the project [1]. This book was published by Springer, the World most prestigious publisher of the scientific literature.

17. Publication of two survey papers [7, 13].

# 3 The Theory of The Globally Convergent Numerical Method

## 3.1 Statement of the CIP

As the forward problem, we consider the following Cauchy problem

$$\varepsilon_r(x)u_{tt} = \Delta u \text{ in } \mathbb{R}^3 \times (0, \infty), \tag{1}$$

$$u(x, 0) = 0, u_t(x, 0) = \delta(x - x_0). \tag{2}$$

Here $\varepsilon_r(x)$ is the spatially distributed variable dielectric constant. It is well known that equation (1) can be derived from Maxwell's equations only in the 2-d case. Also, even though it cannot be derived in the 3-d case for $\varepsilon_r(x) \neq const.$, it was successfully used to model electric waves propagation in our works with experimental data in [1, 2, 3, 4, 5]. The reason of the success with this equation, instead of the Maxwell's system, for real data was explained numerically in [29]. Namely, it was shown in [29] that if the incident electric field has the form $E_{inc} = (0, E_2, 0)$, then the component $E_2(x, t)$ dominates components $E_1(x, t), E_3(x, t)$ and the propagation of $E_2(x, t)$ is well governed by equation (1).

Let $\Omega \subset \mathbb{R}^3$ be a convex bounded domain with the boundary $\partial\Omega \in C^3$. We assume that the coefficient $\varepsilon_r(x)$ of equation (1) is such that

$$\varepsilon_r(x) \in [1, d], \ \varepsilon_r(x) = 1 \text{ for } x \in \mathbb{R}^3 \backslash \Omega, \tag{3}$$

$$\varepsilon_r(x) \in C^2(\mathbb{R}^3), \tag{4}$$

where $d = const. > 1$ characterized the upper bound of the function $\varepsilon_r(x)$. Since we do not impose any smallness conditions on the number $\widetilde{d} = d - 1$, then our results are not "local" ones.

**Coefficient Inverse Problem 3.1 (CIP3.1).** *Suppose that the coefficient $\varepsilon_r(x)$ satisfies (3), (4). Assume that the function $\varepsilon_r(x)$ is unknown in the domain $\Omega$. Determine the function $\varepsilon_r(x)$ for $x \in \Omega$, assuming that the following function $g(x, t)$ is known for a single source position $x_0 \notin \overline{\Omega}$*

$$u(x, t)|_{\partial\Omega \times (0, \infty)} = g(x, t). \tag{5}$$

The assumption $\varepsilon_r(x) = 1$ for $x \in \mathbb{R}^3 \backslash \Omega$ means that one has air outside of the medium of interest $\Omega$. The inequality $\varepsilon_r(x) \geq 1$ is because the speed of EM waves propagation in the medium is less than one in the air. The function $g(x, t)$ models time dependent measurements of the wave field at the boundary of the domain of interest. The assumption that the function $g(x, t)$ is known on the infinite time interval $t \in (0, \infty)$ rather than on a finite one, is not a serious restriction from the computational point of view. Indeed, we work with the Laplace transform (6) and the kernel $e^{-st}$ of the integral (6) decays very rapidly. Therefore, in fact only values of the function $g(x, t)$ for $t \in (0, a)$ with a small number $a$ are used in our method. Besides, our data pre-processing procedure for experimental data [1, 2, 3, 4, 5] shows that we can work with only a small piece of the time dependent experimental curves.

## 3.2 Integral differential equation

Below $C^{k+\alpha}$ denote Hölder spaces, where $k \geq 0$ is an integer and $\alpha \in (0,1)$. Consider the Laplace transform of the functions $u$,

$$w(x,s) = \int_0^\infty u(x,t)e^{-st}dt, \text{ for } s \geq \underline{s} = const. > 0, \tag{6}$$

where $\underline{s}$ is a sufficiently large number. In our numerical studies we choose $\underline{s}$ numerically. Then (1), (2) and Theorem 2.7.1 of [1] imply that

$$\Delta w - s^2 \varepsilon_r (x) w = -\delta(x - x_0), x \in \mathbb{R}^3, \forall s \geq \underline{s}, \tag{7}$$

$$\lim_{|\mathbf{x}| \to \infty} w(x,s) = 0, \ \forall s \geq \underline{s}. \tag{8}$$

Theorem 3.1 is a reformulation of Theorem 2.7.2 of the book [1]. A similar theorem for the case when the point source in (2) is replaced with an incident plane wave was proven in [5].

**Theorem 3.1**. *Let the source $x_0 \notin \overline{\Omega}$ and the function $\varepsilon_r(x)$ satisfies conditions (3) and also $\varepsilon_r \in C^\alpha(\mathbb{R}^3)$. Let $w_1(x,s)$ and $w_d(x,s)$ be solutions of the problem (7), (8) for $\varepsilon_r \equiv 1$ and $\varepsilon_r \equiv d$ respectively,*

$$w_1(x,s) = \frac{\exp(-s|x-x_0|)}{4\pi|x-x_0|}, w_d(x,s) = \frac{\exp\left(-s\sqrt{d}|x-x_0|\right)}{4\pi|x-x_0|}.$$

*Then for any $s > 0$ there exists unique solution $w(x,s)$ of the problem (7), (8), which is represented in the form*

$$w(x,s) = w_1(x,s) + \overline{w}(x,s), \overline{w} \in C^{2+\alpha}(\mathbb{R}^3). \tag{9}$$

*Furthermore,*

$$w_d(x,s) < w(x,s) \leq w_1(x,s), \forall x \neq x_0. \tag{10}$$

*Also, the Laplace transform (6) $w(x,s)$ of the function $u(x,t)$ satisfies (9), (10) for sufficiently large $\underline{s}$ and $s \geq \underline{s}$.*

Thus, below we consider only those solutions of the problem (7), (8), which satisfy conditions (8), (10). Since by (10) $w > 0$, then we can consider the function $v = \ln w/s^2$. Hence, recalling that $x_0 \notin \overline{\Omega}$, we obtain that (7) leads to

$$\Delta v + s^2 |\nabla v|^2 = \varepsilon_r(x), \quad x \in \Omega, \tag{11}$$

$$v|_{\partial\Omega} = \varphi(x,s), \ s \in [\underline{s}, \overline{s}], \tag{12}$$

where the function $\varphi(x,s)$ is generated by the function $g(x,t)$ in (5). Introduce a new function $q(x,s) = \partial_s v(x,s)$. Then under certain non-restrictive conditions

$$D_x^\alpha(v) = O\left(\frac{1}{s}\right), \ D_x^\alpha(q) = O\left(\frac{1}{s^2}\right), \ s \to \infty; \ |\alpha| \leq 2, \tag{13}$$

$$v(x,s) = -\int_s^\infty q(x,\tau) d\tau. \tag{14}$$

We represent the integral (14) as

$$v(x, s) = -\int_s^{\overline{s}} q(x, \tau) d\tau + V(x, \overline{s}),$$ (15)

where $\overline{s} > \underline{s}$ is a large parameter which should be chosen in numerical experiments. Actually, $\overline{s}$ is one of regularization parameters of our method. We call $V(x, \overline{s})$ the *tail function*,

$$V(x, \overline{s}) = -\int_{\overline{s}}^{\infty} q(x, \tau) d\tau.$$

By (15)

$$V(x, \overline{s}) = \frac{\ln w(x, \overline{s})}{\overline{s}^2}, x \in \Omega.$$ (16)

By (13)

$$\left\| D_{\overline{s}}^k V(x, \overline{s}) \right\|_{C^2(\overline{\Omega})} = O\left( \frac{1}{\overline{s}^{k+1}} \right), k = 0, 1; \overline{s} \to \infty.$$ (17)

We obtain from (11)-(17) the following nonlinear integral differential equation

$$\Delta q - 2s^2 \nabla q \cdot \int_s^{\overline{s}} \nabla q(x, \tau) d\tau + 2s \left[ \int_s^{\overline{s}} \nabla q(x, \tau) d\tau \right]^2$$

$$+ 2s^2 \nabla q \nabla V - 2s \nabla V \cdot \int_s^{\overline{s}} \nabla q(x, \tau) d\tau + 2s(\nabla V)^2 = 0.$$ (18)

Let $\psi(x, s) = \partial_s \varphi(x, s)$. Then (12) implies that

$$q|_{\partial \Omega} = \psi(x, s), s \in [\underline{s}, \overline{s}].$$ (19)

Hence, we need to solve the problem (18), (19). Here the truncation parameter $\overline{s}$ is the regularization parameter of our numerical method. The presence of integrals in (18) implies the nonlinearity, which is the main difficulty here. If both functions $q$ and $V$ are approximated well together with their $x-$derivatives up to the second order, then the target unknown coefficient $\varepsilon_r(x)$ can also be approximated well via (11), where the function $v$ is computed via (15). Equation (18) contains two unknown functions $q$ and $V$. The reason why we can approximate both of them is that we treat them differently: while we approximate the function $q$ via outer iterations, the function $V$ is approximated via inner iterations. Thus, below we focus on the following question: *How to solve the problem (18), (19) numerically?*

## 3.3  Layer stripping with respect to $s$

We approximate the function $q(x, s)$ as a piecewise constant function with respect to the pseudo frequency $s$. That is, we assume consider a partition of the interval $[\underline{s}, \overline{s}]$ with the sufficiently small grid step size $h$,

$$\underline{s} = s_N < s_{N-1} < ... < s_1 < s_0 = \overline{s}, h = s_{i-1} - s_i.$$

We assume that $q(x, s) = q_n(x)$ for $s \in (s_n, s_{n-1}]$. The boundary condition (19) is approximated as

$$q_n|_{\partial\Omega} = \overline{\psi}_n(x). \tag{20}$$

where $\overline{\psi}_n$ is the average of the function $\psi$ over the interval $(s_n, s_{n-1})$. Rewrite (18) for $s \in (s_n, s_{n-1}]$ using this piecewise constant approximation. Then multiply the resulting approximate equation by the $s$-dependent Carleman Weight Function (CWF) of the form

$$\mathcal{C}_{n,\mu}(s) = \exp\left[-\mu|s - s_{n-1}|\right], s \in (s_n, s_{n-1}], \tag{21}$$

and integrate with respect to $s \in (s_n, s_{n-1}]$. Here $\mu \gg 1$ is a large parameter of ones choice. Usually we choose $\mu = 50$. We obtain the following approximate equation in $\Omega$ for the function $q_n(x), n = 1, ..., N$

$$
\begin{aligned}
L_n(q_n) &:= \Delta q_n - A_{1n}\left(h\sum_{j=0}^{n-1}\nabla q_j - \nabla V_n\right)\nabla q_n = \tag{22}\\
&= B_n(\nabla q_n)^2 - A_{2,n}h^2\left(\sum_{j=0}^{n-1}\nabla q_j\right)^2 + 2A_{2,n}\nabla V_n\left(h\sum_{j=0}^{n-1}\nabla q_j\right) - A_{2,n}(\nabla V_n)^2.
\end{aligned}
$$

We have intentionally inserted dependence of the tail function $V_n$ from the iteration number $n$ here because we will approximate these functions iteratively. In (22) $A_{1,n} = A_{1,n}(\mu, h)$, $A_{2,n} = A_{2,n}(\mu, h)$ and $B_n = B_n(\mu, h)$ are certain numbers depending on $\mu$ and $h$, see specific formulas in (22). It is convenient to set in (22)

$$q_0 \equiv 0.$$

Since boundary value problems (20), (22) are actually generated by equation (18), which contains Volterra-like $s$-integrals, then these problems can be solved sequentially starting from $q_1$. As to (22), an important point is that $|B_n(\mu, h)| \leq 8\overline{s}^2/\mu$ for $\mu h \geq 1$ (22). We have used $\mu = 50$ in our computations. Hence, assuming that $\mu \gg 1$, we ignore the nonlinear term in (22) via setting

$$B_n(\nabla q_n)^2 := 0. \tag{23}$$

This allows us to solve a linear problem for each $q_n$.

## 3.4 The algorithm

On each iterative step $n$ we approximate both the function $q_n$ and the tail function $V_n$, see Remark 5.1. Each iterative step requires an approximate solution of the boundary value problem (20), (22). First, we choose an initial tail function $V_{1,1}(x) \in C^2(\overline{\Omega})$. The first choice $V_{1,1}$ for the tail function is described in subsection 3.6. For each $q_n$ we have inner iterations to update tails. On these iterations we compute functions $q_{n,k}, k = 1, ..., m$. Here the number of inner iterations m is chosen in numerical experiments. The criterion for the choice is the stabilization of iteratively computed tail functions $V_{n,k}$ at the iteration $k := m$.

**Step** $n^k$, where $n, k \geq 1$. Recall that $q_0 \equiv 0$. Suppose that functions $q_j \in C^2(\overline{\Omega})$, $j = 1, ..., n-1$ and tails $V_1, ..., V_{n-1}, V_{n,k} \in C^2(\overline{\Omega})$ are constructed. To construct the function $q_{n,k}$, we use the FEM to solve the following Dirichlet boundary value problem for the elliptic equation in $\Omega$

$$\Delta q_{n,k} - A_{1n}\left(h\sum_{j=0}^{n-1}\nabla q_j - \nabla V_{n,k}\right)\nabla q_{n,k} =$$

$$-A_{2,n}h^2\left(\sum_{j=0}^{n-1}\nabla q_j\right)^2 + 2A_{2,n}\nabla V_{n,k}\cdot\left(h\sum_{j=0}^{n-1}\nabla q_j\right) - A_{2,n}\left(\nabla V_{n,k}\right)^2, \tag{24}$$

$$q_{n,k}|_{\partial\Omega} = \overline{\psi}_n(x).$$

To reconstruct an approximation $\varepsilon_r^{(n,k)}(x)$ for the function $\varepsilon_r(x)$, we first use the following discrete analog of (15)

$$v_{n,k}(x, s_n) = -hq_{n,k}(x) - h\sum_{j=1}^{n-1}q_j(x) + V_{n,k}(x). \tag{25}$$

Next, let $\Omega' \subset \Omega$ be a subdomain of $\Omega$ such that

$$\Omega' \subset \Omega, \partial\Omega' \cap \partial\Omega = \varnothing. \tag{26}$$

Consider a function $\chi(x)$,

$$\chi \in C^3(\mathbb{R}^3), \chi(x) = \begin{cases} 1 \text{ in } \Omega', \\ \text{between 0 and 1 in } \Omega\backslash\Omega', \\ 0 \text{ in } \mathbb{R}^3\backslash\Omega. \end{cases} \tag{27}$$

For any function $a \in C^\alpha(\overline{\Omega})$ define

$$\widehat{a}(x) = (1 - \chi(x)) + \chi(x)a(x), x \in \mathbb{R}^3. \tag{28}$$

Hence,

$$\widehat{a}(x) = \begin{cases} 1, x \in \mathbb{R}^3\backslash\Omega, \\ a(x) \text{ in } \Omega', \\ \geq 1 \text{ in } \Omega, \text{ if } a(x) \geq 1 \text{ in } \Omega. \end{cases} \tag{29}$$

11

Next, using (11), (25), (28) and (29), we set

$$f_{n,k}(x) \quad : \quad = \Delta v_{n,k}(x, s_n) + s_n^2 |\nabla v_{n,k}(x, s_n)|^2, n \geq 1, x \in \Omega, \tag{30}$$

$$\varepsilon_r^{(n,k)}(x) \quad : \quad = \widehat{f}_{n,k}(x). \tag{31}$$

Next, we solve the forward problem (7), (8) with $\varepsilon_r(x) := \widehat{\varepsilon}_r^{(n,k)}(x), s := \overline{s}$ and obtain the function $w_{n,k}(x, \overline{s})$ satisfying conditions (9), (10) (Theorem .1). Next, using (16), we set for the new tail

$$V_{n,k+1}(x) = \frac{\ln w_{n,k}(x, \overline{s})}{\overline{s}^2}, x \in \Omega.$$

We continue these iterations with respect to tails for $k = 1, ..., m$.Next, we set

$$\varepsilon_r^{(n)}(x) := \varepsilon_r^{(n,m)}(x), q_n(x) := q_{n,m}(x), V_n(x) := V_{n,m}(x) := V_{n+1,1}(x) \text{ for } x \in \Omega.$$

We stop iterations with respect to $n$ at $n := \overline{N} \in [1, N]$, where $\overline{N}$ is a certain number at which convergence occurs. Stopping criteria are discussed in detail in our publications [1, 16, 2, 3, 4, 5]and they go along well with one of backbone ideas of the theory of ill-posed problems. By this idea, the iteration number can be chosen as a regularization parameter, see pages 156 and 157 of the book [40]. Furthermore, we have constantly observed that results of our numerical studies go along well with convergence criteria.

## 3.5 Estimates of tail functions

The most difficult question on the way of proving our advanced convergence theorem was the question about estimating gradients of tail functions in Hölder norms $C^{1+\alpha}$. This was done in Theorem 2.9.1.2 of the book [1] as well as in Theorem 4.2 of [16]. We now reformulate these theorems.

Let $\Omega_1 \subset \mathbb{R}^3$ be a finite domain with $\partial \Omega_1 \in C^3$ and such that $\Omega \subset \Omega_1, \partial \Omega \cap \partial \Omega_1 = \varnothing$. Let $d > 1$ be the number from (3) and $\overline{d} > d$ be another number. Introduce the set of functions $P(d, \overline{d})$ as

$$P(d, \overline{d}) = \left\{ \varepsilon_r(x) \in C^\alpha(\overline{\Omega}) : \|\varepsilon_r\|_{C^\alpha(\overline{\Omega})} \leq \overline{d} + 1, 1 \leq \varepsilon_r(x) \leq d + 1, \forall x \in \overline{\Omega} \right\}.$$

For each function $\varepsilon_r \in P(d, \overline{d})$ we construct the function $\varepsilon_r(x)$ by the formula (28), where the function $\chi(x)$ is defined in (27). Let $w_{\widehat{\varepsilon}_r}(x, \overline{s})$ be the solution of the problem (7)-(10) with $\varepsilon_r := \widehat{\varepsilon}_r, s := \overline{s}$. Using (16), define

$$V_{\widehat{\varepsilon}_r}(x, \overline{s}) = \frac{\ln w_{\widehat{\varepsilon}_r}(x, \overline{s})}{\overline{s}^2}. \tag{32}$$

Following again one of the main concepts of the theory of Ill-Posed Problems [1], we assume in Theorem 3.2 the existence of the exact solution $\varepsilon_r^*(x)$ for the unperturbed exact data $g^*(x, t)$ in (3).

**Theorem 3.2**. *Let the parameter $\overline{s} > 1$ and $x_0 \notin \overline{\Omega}_1$. Let $\varepsilon_r^* (x) \in P\left(d, \overline{d}\right)$ be the exact solution of CIP3.1 with the noiseless data $g^* (x, t)$ in (3) and $V_{\varepsilon_r^*} (x, \overline{s})$ be the exact tail defined by the formula (32). Then there exists a constant $B = B\left(\Omega, \Omega_1, \chi, x_0, \overline{s}, x_0\right) > 2$ depending only on listed parameters such that the following estimates hold*

$$\left\|\nabla V_{\varepsilon_r^*}\right\|_{C^{1+\alpha}\left(\overline{\Omega}\right)} \leq B, \left\|\nabla V_{\widehat{\varepsilon}_r}\right\|_{C^{1+\alpha}\left(\overline{\Omega}\right)} \leq B, \forall \varepsilon_r \in P\left(d, \overline{d}\right),$$

$$\left\|\nabla V_{\widehat{\varepsilon}_r} - \nabla V_{\varepsilon_r^*}\right\|_{C^{1+\alpha}\left(\overline{\Omega}\right)} \leq B \left\|\varepsilon_r - \varepsilon_r^*\right\|_{C^\alpha\left(\overline{\Omega}\right)}, \forall \varepsilon_r \in P\left(d, \overline{d}\right).$$

## 3.6   The first tail

In the description of the algorithm in subsection 3.4 we have left open the question about the choice of the first tail function $V_{1,1}$. This question is addressed in this subsection. By (16) the asymptotic behavior of the exact tail is

$$V_{\varepsilon_r^*} (x, \overline{s}) = \frac{p^* (x)}{\overline{s}} + O\left(\frac{1}{\overline{s}^2}\right), \overline{s} \to \infty, x \in \overline{\Omega}.$$

for a certain function $p^* (x)$. We truncate the second term of this asymptotic behavior. Thus, our **Approximate Mathematical Model** consists of the following assumption.

   **Assumption.** There exists a function $p^* (x) \in C^{2+\alpha}\left(\overline{\Omega}\right)$ such that the exact tail function $V^* (x, s)$ has the form

$$V_{\varepsilon_r^*} (x, s) := \frac{p^* (x)}{s}, \forall s \geq \overline{s}. \tag{33}$$

Furthermore, by (32) we assume that

$$\frac{p^* (x)}{s} = \frac{\ln w^* (x, s)}{s^2}, \ \forall s \geq \overline{s}. \tag{34}$$

   Since $q^* (x, s) = \partial_s V_{\varepsilon_r^*} (x, s)$ for $s \geq \overline{s}$, we derive from (33) that

$$q^* (x, \overline{s}) = -\frac{p^* (x)}{\overline{s}^2}. \tag{35}$$

Substituting (33) and (35) in the equation (18) and boundary data (19) for the function $q^* (x, s)$ an setting there $s := \overline{s}$, we obtain the following *approximate* Dirichlet boundary value problem for the function $p^* (x)$

$$\Delta p^* = 0 \text{ in } \Omega, \ p^* \in C^{2+\alpha}\left(\overline{\Omega}\right), \tag{36}$$
$$p^*|_{\partial\Omega} = -\overline{s}^2\psi^* (x, \overline{s}), \tag{37}$$

where $\psi^* (x, s)$ is the exact function $\psi (x, s)$, which corresponds to the function $g^* (x, t)$. The approximate equation (36) is valid only within the framework of Assumption. Although this equation is linear, formula (11) for the reconstruction of the target coefficient is nonlinear.

Recall that by (19) $q(x, s) = \psi(x, s)$, $\forall (x, s) \in \partial\Omega \times [\underline{s}, \overline{s}]$. Assume that

$$\psi(x, s) \in C^{2+\alpha}\left(\overline{\Omega}\right), \forall s \in [\underline{s}, \overline{s}]. \tag{38}$$

Consider the solution $p(x)$ of the following boundary value problem

$$\Delta p = 0 \text{ in } \Omega, \ p \in C^{2+\alpha}\left(\overline{\Omega}\right), \tag{39}$$

$$p|_{\partial\Omega} = -\overline{s}^2 \psi(x, \overline{s}). \tag{40}$$

Given (38), the Schauder theorem implies that there exists unique solution $p$ of the problem (39), (40).

As the first guess for the tail function we take

$$V_{1,1}(x) := \frac{p(x)}{\overline{s}}. \tag{41}$$

It follows from (33)-(41) that

$$\left\|V_{1,1} - V_{\varepsilon_r^*}\right\|_{C^{2+\alpha}(\overline{\Omega})} \leq M \left\|\psi(x, \overline{s}) - \psi^*(x, \overline{s})\right\|_{C^{2+\alpha}(\partial\Omega)}, \tag{42}$$

where $M = M(\Omega) = const. > 0.$

**Remarks:**

**1**. We point out that the truncation of the asymptotic series with respect to $1/s$ is done in Assumption *only on the first iteration*, i.e. only for the first tail. No assumptions are imposed on follow up iterations.

**2**. An interesting conclusion which follows immediately from (42) is that we obtain a good approximation for the solution of our CIP already from the first tail. *In other words, a good approximation is obtained already on the first iteration of our method.* And we have constantly observed this computationally. The error of this approximation depends only on the error in the boundary data. It follows from here and from (11), (15) that we obtain a good approximation for the target coefficient already from the *first tail*. Theorem 3.3 guarantees that all other solutions obtained in the above iterative process also provide good approximations, as long as the number of iterations is not too large. This means that we should develop numerically a stopping criterion to stop iterations. Suppose now that iterations are stopped before this stopping criterion is met. In particular, they can be stopped just on the first iteration. In this case we can apply the second stage of our two-stage numerical procedure [1]. Namely, we could apply a locally convergent adaptivity technique to refine solution. We would take the solution obtained on the globally convergent stage as the starting point of iterations.

## 3.7  Global convergence theorem

The proof of Theorem 3.3 was first published in our book [1]: see Theorem 2.9.4 there. Next, it was published in [16]. Theorem 3.3 was extended in [5] to the case when the point source

is replaced by an incident plane wave. The proof of Theorem 3.3 essentially uses Theorem 3.2 and Assumption.

Let $\overline{\psi}_n(x), x \in \partial\Omega$ be the boundary data (20) for the functions $q_n(x)$ generated by the data function $\psi(x), x \in \partial\Omega$ in (19). Let $\psi^*(x), x \in \partial\Omega$ be the function $\psi(x)$ which corresponds to the exact solution $\varepsilon_r^*(x), x \in \Omega$ of CIP3.1, which was introduced in Theorem 3.2. Let $\overline{\psi}_n^*(x), x \in \partial\Omega$ be corresponding exact functions $\overline{\psi}_n(x)$. Let the small number $\sigma \in (0,1)$ represents the level of the error in the data $\psi(x)$. Then it is natural to assume that

$$\left\|\overline{\psi}_n - \overline{\psi}_n^*\right\|_{C^{2+\alpha}(\partial\Omega)} \leq C^*(h+\sigma), C^* = const. \geq 1. \tag{43}$$

**Theorem 3.3**. *Let Assumption be valid. Consider the algorithm of subsection 3.4. Let the parameter $\overline{s} > 1$ and $x_0 \notin \overline{\Omega}_1$. Let $\varepsilon_r^*(x) \in P\left(d,\overline{d}\right)$ be the exact solution of CIP3.1 with the noiseless data $g^*(x,t)$ in (3) and $V_{\widehat{\varepsilon}_r^*}(x,\overline{s})$ be the exact tail defined by the formula (32). Assume that (43) holds. Introduce the error parameter $\eta$,*

$$\eta = 2(h+\sigma).$$

*Assume that the parameter $\mu$ in the Carleman Weight Function (21) is so large that*

$$\mu \geq \frac{8\left(\overline{s}C^*\right)^2}{\eta}.$$

*Also, assume that in that algorithm all functions $\varepsilon_r^{(n,k)}(x) \geq 1, x \in \Omega$. Then there exists a constant $B = B(\Omega, \Omega_1, \chi, x_0, \overline{s}, x_0) > 2$ depending only on listed parameters such that if the parameter $\eta$ is so small that*

$$\eta \in (0, \eta_0) \;\; where \; \eta_0 = \frac{1}{B^{3Nm}}, \tag{44}$$

*then the following estimate holds with a number $\omega = \omega(B,N,m) \in (0,1)$ depending only on listed parameters*

$$\left\|\varepsilon_r^{(n,k)} - \varepsilon_r^*\right\|_{C^\alpha(\overline{\Omega})} \leq \eta^\omega, \forall \eta \in (0,\eta_0).$$

*In other words, the algorithm of subsection 3.4 is globally convergent.*

In particular, (44) requires that the error parameter $\eta$ and the total number of iterations $Nm$ should be connected with each other. We again refer to pages 156 and 157 of the classical book about the theory of Ill-Posed Problems [40]. It follows from there that such connection should be in place even for simpler ill-posed problems.

# 4  The Theory Of the Image Refinement via Adaptive Finite Element Method (Adaptivity)

As it was pointed out in Introduction, we have constantly observed that the best approach is to apply a two-stage numerical procedure. On the first stage the globally convergent

numerical method delivers a function which is sufficiently close to the exact coefficient. In fact, the first stage provides accurate locations and accurate values of refractive indices $n(x) = \sqrt{\varepsilon_r(x)}$ of targets mimicking explosives. On the second stage the locally convergent method, the adaptivity, is applied to refine images. The adaptivity uses the solution of the first stage as its starting point. The adaptivity provides accurate shapes of those targets. Therefore, the two-stage procedure provides all three components of interest of targets:

1. Refractive indices.

2. Locations.

3. Shapes.

The classical Tikhonov functional for solving ill-posed problems, including CIPs is known for a long time, see, e.g. the books [1, 40]. However, what makes the adaptivity attractive is that it minimizes this functional on a *sequence* of locally refined meshes of finite elements rather than on a single mesh. Although the adaptivity for ill-posed problems has been known since 2001, see, e.g. [30]-[35], a rigorous proof of the **key fact** that mesh refinements indeed provide a better accuracy was absent. We call the latter property *relaxation*. The major obstacle for the proof of the relaxation property is the ill-posed nature of inverse problems. The *first rigorous proof* of this fact was obtained in 2010 [28]. Next, this result was refined in the book [1]. A survey was published in [7].

In this section we present our results about the relaxation of the adaptivity. We point out that it was natural to prove first the relaxation property for an abstract operator $F$. However, it is well known in the theory of ill-posed problems that it is usually not easy to transform this result to the case of our specific CIP 3.1. Nevertheless, this was done in [1, 7, 28].

## 4.1   The space of finite elements

As the first step for establishing the relaxation property of the adaptivity, we introduce the space of finite elements. It is worthy to point out that the group led by the PI was the *first* one who has introduced this space in 2010 [28].

Let $\Omega \subset \mathbb{R}^n, n = 2, 3$ be a bounded domain. Consider a discretization of $\Omega$ by an unstructured mesh $T$ using non-overlapping elements $K$. For $\mathbb{R}^2$ the elements $K$ are triangles or quadrilaterals and for $\mathbb{R}^3$ tetrahedrons or hexahedrons such that $T = K_1, ..., K_l$, where $l$ is the number of elements in $\Omega$, and

$$D = \cup_{K \in T} K = K_1 \cup K_2 ... \cup K_l.$$

We obtain a polygonal domain $D$ and assume for brevity that $D = \Omega$.

Following section 76.4 of the book [42], consider piecewise linear functions $\{e_j(x, T)\}_{j=1}^N \subset C(\overline{\Omega})$, which are called *test functions*. Functions $\{e_j(x, T)\}_{j=1}^N$ are linearly independent in

$\Omega$. Here, $N$ is the total number of nodes in the mesh $T$. Let $\{N_i\}$ be the set of nodal points of triangle/tetrahedra $K$ for all $K \in T$. Then

$$e_j(N_i, T) = \begin{cases} 1, i = j, \\ 0, i \neq j. \end{cases}$$

We introduce the finite element space $V_h$ as

$$V_h = \left\{v(x) \in H^1(\Omega) : v \in C(\overline{\Omega}), \ v|_K \in P_1(K) \ \forall K \in T\right\},$$

where $P_1(K)$ denotes the set of piecewise-linear functions on $K$. The finite dimensional finite element space $V_h$ is constructed such that $V_h \subset V$.

Let $h_K$ be the diameter of element $K$ which we define as the longest side of $K$ and $r$ be the radius of the maximal circle/sphere inscribed in $K$. We impose the shape regularity assumption for all triangles/tetrahedra uniformly for all possible triangulations $T$ which we consider. Specifically, we assume that

$$a_1 \leqslant h_K \leqslant ra_2, \quad a_1, a_2 = const. > 0, \ \forall K \in T, \ \forall \ T, \tag{45}$$

where numbers $a_1, a_2$ are independent on the triangulation $T$. Let $h_{\max}(T)$ and $h_{\min}(T)$ be respectively the maximal and minimal diameters of triangles/tetrahedra of the triangulation $T$. We assume everywhere below that

$$\frac{h_{\min}(T)}{h_{\max}(T)} \leq c_T, \forall T \tag{46}$$

for a certain positive constant $c_T$. Obviously, the number of all possible triangulations satisfying (45), (46) is finite. Thus, we introduce the following finite dimensional linear space $H$,

$$H = \bigcup_T V_h(T), \ \forall T \ \text{satisfying (45), (46)}.$$

Hence,

$$\dim H < \infty, \ H \subset \left(C(\overline{\Omega}) \cap H^1(\Omega)\right), \ \partial_{x_i} f \in L_\infty(\Omega), \ \forall f \in H. \tag{47}$$

In (47) "$\subset$" means the inclusion of sets. We equip $H$ with the same inner product as the one in $L_2(\Omega)$. Denote $(,)$ and $\|\cdot\|$ the inner product and the norm in $H$ respectively, $\|f\|_H := \|f\|_{L_2(\Omega)} := \|f\|, \ \forall f \in H$. Everywhere in section 4 $H$ is this space. We view the space $H$ as an "ideal" space of very fine finite elements, which cannot be reached in practical computations. At the same time, all other spaces of finite elements we work with below are subspaces of $H$. In particular, this means that we assume without further mentioning that (45) and (46) are valid for all meshes considered below.

Keeping in mind the mesh refinement process in the adaptivity, we now explain how do we construct triangulations $\{T_n\}$ as well as corresponding subspaces $\{M_n\}$ of the space $H$ which correspond to mesh refinements. Consider the first triangulation $T_1$ with rather coarse mesh. We set $M_1 := V_h(T_1) \subset H$. Suppose that the pair $(T_n, M_n)$ is constructed after $n$

mesh refinements and that the basis functions in the space $M_n$ are $\{e_j(x, T_n)\}_{j=1}^{N_n}$. We now want to refine the mesh again. We define the pair $(T_{n+1}, M_{n+1})$ as follows. We refine the mesh in the standard manner as it is usually done when working with triangular/tetrahedron finite elements. When doing so, we keep (45). Hence, we obtain both the triangulation $T_{n+1}$ and the corresponding test functions $\{e_j(x, T_{n+1})\}_{j=1}^{N_{n+1}}$. It is well known that test functions $\{e_j(x, T_n)\}_{j=1}^{N_n}$ are linearly dependent from new test functions $\{e_j(x, T_{n+1})\}_{j=1}^{N_{n+1}}$. Thus, we define the subspace $M_{n+1}$ as

$$M_{n+1} := \mathrm{Span}\left(\{e_j(x, T_{n+1})\}_{j=1}^{N_{n+1}}\right).$$

Therefore, we have obtained a finite set of linear subspaces $\{M_n\}_{n=1}^{N}$ of the space $H$. Each subspace $M_n$ corresponds to the mesh refinement number $n$, $M_{n+1}\backslash M_n \neq \varnothing$ and

$$M_n \subset M_{n+1} \subset H, n \in [1, N-1].$$

Let $I$ be the identity operator on $H$. For any subspace $M \subset H$, let $P_M : H \to M$ be the orthogonal projection operator of the space $H$ onto its subspace $M$. Denote for brevity $P_n := P_{M_n}$. Let $h_n$ be the maximal grid step size of $T_n$. Hence, $h_{n+1} \leqslant h_n$. Let $f_n^I$ be the standard interpolant of the function $f \in H$ on triangles/tetrahedra of $T_n$, see section 76.4 of [42]. It can be easily derived from formula (76.3) of [42] that

$$\left\|f - f_n^I\right\| \leq K \left\|\nabla f\right\|_{L_\infty(\Omega)} h_n, \forall f \in H, \tag{48}$$

where $K = K(\Omega, r, a_1, a_2) = const. > 0$. Since $f_n^I \in H, \forall f \in H$, then by one of well known properties of orthogonal projection operators,

$$\left\|f - P_n f\right\| \leqslant \left\|f - f_n^I\right\|, \ \forall f \in H. \tag{49}$$

Hence, (48) and (49) imply that with a different constant $K = K(\Omega, r, a_1, a_2) > 0$

$$\left\|f - P_n f\right\| \leqslant K \left\|\nabla f\right\|_{L_\infty(\Omega)} h_n, \forall f \in H. \tag{50}$$

Since $H$ is a finite dimensional space in which all norms are equivalent, it is convenient for us to rewrite (50) with a different constant $K = K(\Omega, r, , a_1, a_2) > 0$ as

$$\left\|x - P_n x\right\| \leqslant K \left\|x\right\| h_n, \ \forall x \in H. \tag{51}$$

For any $a > 0$ and for any $x \in H$ denote $V_a(x) = \{z \in H : \left\|x - z\right\| < a\}$.

## 4.2   Relaxation

Let $H_2$ be another Hilbert space. Let $G \subset H$ be an open bounded set and $F : \overline{G} \to H_2$ be an operator which is continuos, has the Fréchet derivative $F'(x), \forall x \in G$ and the operator

18

$F'(x)$ is Lipschitz continous on the set $G$. For convenience, we assume below that $F$ is one-to-one. Consider the equation

$$F(x) = y, x \in G. \tag{52}$$

As it is usually done in the regularization theory [1, 40], we assume that the right hand side of equation (52) is given with a small error $\delta \in (0,1)$. We also assume that there exists an "ideal" exact solution $x^*$ of (52) with the "ideal" exact data $y^*$. Thus, we assume that

$$F(x^*) = y^*, x^* \in G, \|y - y^*\|_2 \leq \delta. \tag{53}$$

Let $x_0 \in H$ be a first guess for the exact solution $x^*$. Consider the Tikhonov functional $J_\alpha(x)$,

$$J_\alpha(x) = \frac{1}{2}\|F(x) - y\|_2^2 + \frac{\alpha}{2}\|x - x_0\|^2, x \in \overline{G}, x_0 \in G, \tag{54}$$

where $\alpha \in (0,1)$ is the regularization parameter. We impose a rather conventional assumption that

$$\alpha = \alpha(\delta) = \delta^{2\mu}, \mu = const. \in \left(0, \frac{1}{2}\right). \tag{55}$$

A minimizer $x_{\alpha(\delta)}$ of this functional is called regularized solution. Since by (47) $\dim H < \infty$, then the following lemma follows immediately from the Weierstrass theorem.

**Lemma 4.1**. *Let $F$ be the operator defined above in this section. Then there exists a regularized solution $x_{\alpha(\delta)} \in \overline{G}$,*

$$\inf_{\overline{G}} J_\alpha(x) = \min_{\overline{G}} J_\alpha(x) = J_\alpha(x_\alpha). \tag{56}$$

Theorem 4.1 specifies the location of the minimizer $x_{\alpha(\delta)}$ of the functional (54).

**Theorem 4.1**. *Let $V_1(x^*) \subset G$. Let in (54) the first guess $x_0$ for the exact solution $x^*$ be so accurate that*

$$\|x_0 - x^*\| < \frac{\delta^{3\mu}}{3}. \tag{57}$$

*Then there exists a sufficiently small number $\delta_0 = \delta_0(N_1, N_2, \mu) \in (0,1)$ such that for every $\delta \in (0, \delta_0)$ and for $\alpha = \alpha(\delta)$ satisfying (55) there exists unique regularized solution $x_{\alpha(\delta)}$ of equation (52) on the set $G$. Furthermore, $x_{\alpha(\delta)} \in V_{\delta^{3\mu}/3}(x^*)$. In addition, the gradient method of the minimization of the functional $J_{\alpha(\delta)}(x)$, which starts at $x_0$, converges to $x_{\alpha(\delta)}$. In the noiseless case with $\delta = 0$ one should replace "$\delta_0 = \delta_0(F, \mu) \in (0,1)$" with $\alpha_0 = \alpha_0(F) \in (0,1)$ to be sufficiently small and also require that $\alpha \in (0, \alpha_0)$.*

Since we sequentially minimize the Tikhonov functional on subspaces $\{M_n\}_{n=1}^N$ in the adaptivity procedure, then we need to establish first the existence of a minimizer on each of these subspaces. Theorem 4.2 ensures both existence and uniqueness of the minimizer of the functional $J_\alpha$ on each subspace of the space $H$, as long as the maximal grid step size of finite elements, which are involved in that subspace, is sufficiently small.

**Theorem 4.2.** *Let conditions of Theorem 4.1 hold. Let $M \subseteq H$ be a subspace of $H$. Assume that $\|x^*\| \leq B$, where the number $B > 0$ is known in advance. Suppose that the maximal grid step size $\widetilde{h}$ of finite elements of $M$ is so small that*

$$\widetilde{h} \leq \frac{\delta^{4\mu}}{5BRK}, \tag{58}$$

*where $K$ is the constant in (51) and the constant $R > 0$ depends only on the operator $F$. Furthermore, assume that the first guess $x_0$ for the exact solution $x^*$ in the functional $J_{\alpha(\delta)}$ is so accurate that (57) is in place. Then there exists a sufficiently small number $\delta_0 = \delta_0(F, \mu) \in (0, 1)$ such that for every $\delta \in (0, \delta_0)$ there exists unique minimizer $x_{M,\alpha(\delta)} \in G \cap M$ of the functional $J_\alpha$ on the set $G \cap M$. Furthermore, $x_{M,\alpha(\delta)} \in V_{\delta^{3\mu}}(x^*) \cap M$. Let $x_{\alpha(\delta)} \in V_{\delta^{3\mu}/3}(x^*)$ be the regularized solution of equation (52), which is guaranteed by Theorem 4.1. Then the following a posteriori error estimate holds*

$$\left\| x_{M,\alpha(\delta)} - x_{\alpha(\delta)} \right\| \leq \frac{2}{\delta^{2\mu}} \left\| J'_\alpha \left( x_{M,\alpha(\delta)} \right) \right\|. \tag{59}$$

We are now ready to formulate our main result about the adaptivity, which is the relaxation Theorem 4.3

**Theorem 4.3** (relaxation). *Let $M_n \subset H$ be the subspace obtained after $n$ mesh refinements, as described in subsection 4.1. Let $h_n$ be the maximal grid step size of the subspace $M_n$. Suppose that all conditions of Theorem 4.2 hold with the only exception that the subspace $M$ is replaced with $M_n$ and the inequality (58) is replaced with*

$$h_n \leq \frac{\delta^{4\mu}}{5BRK}.$$

*Let $\delta \in (0, \delta_0)$, where the number $\delta_0 \in (0, 1)$ is defined in Theorem 4.2. Let $x_n \in V_{\delta^{3\mu}}(x^*) \cap M_n$ be the unique minimizer of the functional $J_\alpha(x)$ in (54) on the set $G \cap M_n$ (Theorem 4.2). Let $x_{\alpha(\delta)} \in V_{\delta^{3\mu}/3}(x^*)$ be the unique regularized solution (Theorem 4.1). Assume that*

$$x_n \neq x_{\alpha(\delta)},$$

*i.e. $x_{\alpha(\delta)} \notin M_n$, meaning that the regularized solution is not yet reached after $n$ mesh refinements. Let $\eta \in (0, 1)$. Then one can choose the maximal grid size $h_{n+1} = h_{n+1}(F, \delta, B, K, \eta) \in (0, h_n]$ of the mesh refinement number $(n + 1)$ so small that*

$$\left\| x_{n+1} - x_{\alpha(\delta)} \right\| \leq \eta \left\| x_n - x_{\alpha(\delta)} \right\|,$$

*where $x_{n+1} \in V_{\delta^{3\mu}}(x^*) \cap M_{n+1}$ is the unique minimizer of the functional (54) on the set $G \cap M_{n+1}$. Hence,*

$$\left\| x_{n+1} - x_{\alpha(\delta)} \right\| \leq \eta^n \left\| x_1 - x_{\alpha(\delta)} \right\|.$$

Theorems 4.1-4.3 are formulated for an abstract operator $F$. They need to be specified for the case of CIP3.1 (section 3.1), which is a non-trivial task. This specification was done

in [1, 7, 28]. Let $E_{\alpha(\delta)}(\varepsilon_r)$ be the analog of the functional $J_\alpha(x)$ in (54) for the case of this CIP. Let $E'_{\alpha(\delta)}(\varepsilon_r)$ be its Fréchet derivative. Then it was derived from (59) that

$$\left\| \varepsilon_r - \varepsilon_{r,\alpha(\delta)} \right\| \leq \frac{2}{\delta^{2\mu}} \left\| E'_{\alpha(\delta)}(\varepsilon_r) \right\|_{L_2(\Omega)}, \forall \varepsilon_r \in V_{\delta^{3\mu}}(\varepsilon_r^*). \tag{60}$$

In addition, the following relaxation property was derived from Theorem 4.3

$$\left\| \varepsilon_{r,n+1} - \varepsilon_{r,\alpha(\delta)} \right\| \leq \eta \left\| \varepsilon_{r,n} - \varepsilon_{r,\alpha(\delta)} \right\|, \eta \in (0,1),$$

as long as $\varepsilon_{r,n} \neq \varepsilon_{r,\alpha(\delta)}$ and the maximal mesh step size $h_{n+1}$ on the subspace $M_{n+1}$ is sufficiently small. The estimate (60) indicates that one should refine mesh on the refinement step number $n+1$ near those points where the function $\left| E'_{\alpha(\delta)}(\varepsilon_{r,n})(x) \right|$. The explicit form of the function $E'_{\alpha(\delta)}(\varepsilon_{r,n})(x)$ was obtained in a standard way using the adjoint problem method. Thus, we arrive at

**Mesh Refinement Recommendation.** *Let $\beta \in (0,1)$ be the tolerance number, which is chosen numerically. Refine the mesh in such subdomains of $\Omega$ where*

$$\left| E'_{\alpha(\delta)}(\varepsilon_{r,n})(x) \right| \geq \beta_1 \max_{\overline{\Omega}} \left| E'_{\alpha(\delta)}(\varepsilon_{r,n})(x) \right|. \tag{61}$$

In all tests with adaptivity below we have used the mesh refinement recommendation (61).

# 5    The Work With Experimental Data for Targets Placed in Air

In this section we describe our work with backscattering experimental data for targets located in the air. Results of this section are reflected in four publications [2, 3, 4, 6]. The main challenge was a *huge discrepancy* between simulated and experimental data, compare Figures 3-a and 3-b. Therefore, one of key difficulties was to invent a new data preprocessing procedure. The data preprocessing is inevitably a heuristic procedure. This procedure has "moved" the pre-processed data closer to the simulated ones than the raw data. The pre-processed data were used as an input for our globally convergent algorithm. Therefore, the success of our studies of experimental data proves a significant degree of robustness of the globally convergent method of this project.

We point out that in both preprocessing of experimental data and postprocessing of calculated results it is *crucial* to choose such parameters and procedures which would work for all targets without any exceptions. Or at least one should choose one set parameters/procedures for all dielectric and the second one for all metallic targets. If such a choice is possible, then one can claim that such a procedure is both unbiased and stable. This is exactly what is done below.

## 5.1 Data acquisition

Two main pieces of our experimental apparatus are Picosecond Pulse Generator and Textronix Oscilloscope, see Figure 1.
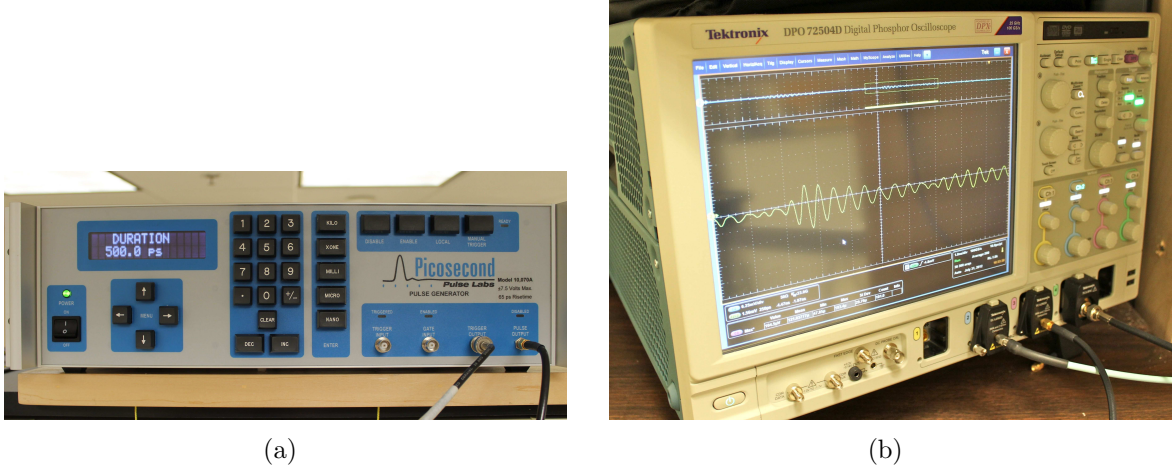


| (a) | (b) |

Figure 1: *Two main pieces of our experimental apparatus. a) Picosecond Pulse Generator 10070A. b) Textronix Oscilloscope.*
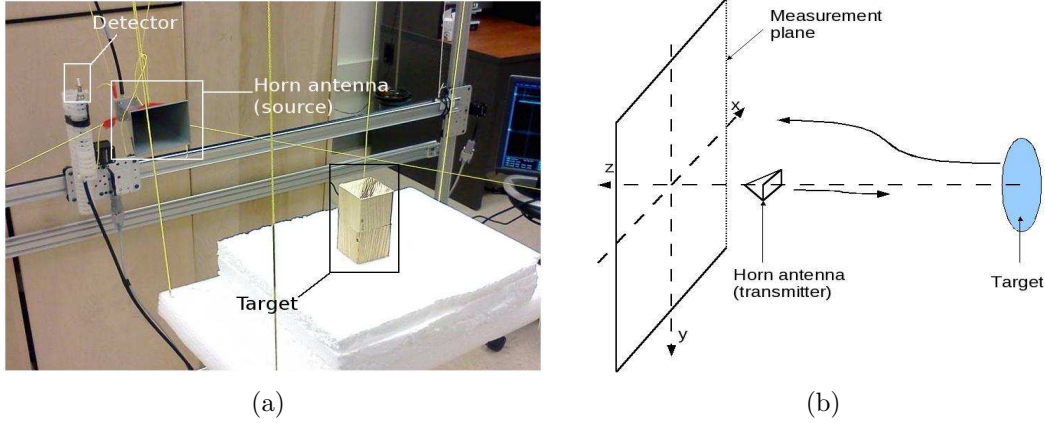


| (a) | (b) |

Figure 2: *(a): A picture of our experiment setup; (b) Diagram of our setup.*

Our experimental configuration is shown in Figure 2. Let $E(x,t) = (E_x, E_y, E_z)(x,t)$ be the vector of the electric field. Then it is clear from Figures 2-a,b that $u(x,t) = E_y(x,t)$, where $u$ is the function in (1). The incident wave field is $E_{inc}(x,t) = (0, \delta(x - x_0)\delta(t), 0)$. It was demonstrated numerically in [29] that in this case $|E_y(x,t)| >> |E_x(x,t)|, |E_z(x,t)|$ and the propagation of the component $E_y(x,t)$ is well governed by equation (1). This and especially the accuracy of our results below justify the use of equation (1).

The setup of our measurements included a horn antenna (transmitter) fixed at a given position and a detector scanned in a square of a vertical plane, which we refer to as the

measurement plane. Consider the Cartesian coordinate system $Oxyz$ as shown in Figure 2b. The scanning area was 1 meter by 1 meter in both horizontal and vertical directions with the step size of 0.02, starting at $(x, y) = (-0.5, -0.5)$, and ending at $(x, y) = (0.5, 0.5)$.

In our mathematical model (1), (2), we assume that the source point $x_0$ is in $\mathbb{R}^3 \setminus \overline{\Omega}$. However, due to some technical difficulties with the mechanical scanning system, the horn antenna was not placed behind but in front of the measurement plane (between the measurement plane and the targets). Therefore a small area in the center of the scanning area on the measurement plane was shaded by the horn. The horn was placed at the distance of about 0.2-0.25 from the measurement plane and the distances from the targets to the measurement plane are about 0.8.

At each position of the detector, a number of electric pulses were emitted by the horn. The detector received two types of signals: the direct signals from the source and the backscatter signals by the targets. The direct signals are used for time reference in data pre-processing. There were also other unwanted signals due to scattering by some objects in the room. To reduce the instability of the recorded signals in terms of magnitude, the measurements were repeated 800 times at each detector position and the recorded signals were averaged. By scanning the detector and repeating the measurements, we obtained essentially the same signals as using one incident signal and multiple detectors at the same time.

Pulses were generated by the Picosecond Pulse Generator 10070A. The scattered signals were measured by a Tektronix DSA70000 series real-time oscilloscope. The emitted pulses were of 300 picoseconds duration. The wavelength of the incident pulses was about 0.03 m. The sampling rate (the step size in time between two consecutive records of captured signals) was $\Delta t = 10$ picoseconds. Each signal was recorded for 10 nanoseconds.

## 5.2   Six steps of data pre-processing

One of the biggest challenges in working with these experimental data is the *huge misfit* between these data and the data produced via computational simulations. There are several causes of this misfit such as:

1. The instability of the amplitude of the emitted signals (incident waves) which causes the instability of the received signals.

2. Unwanted (parasitic) scattered waves caused by the presence of several existing objects around our devices, see Figure 2a.

3. The shadow on the measurement plane caused by the transmitting horn antenna.

4. The difference between the experimental and simulated incident waves.

Figure 3 compares experimental and computationally simulated signals at the same detector.
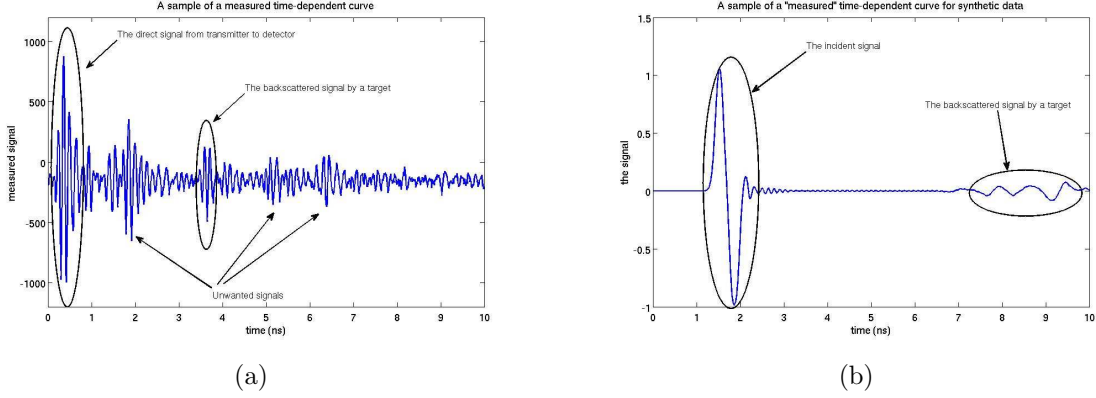
Figure 3: *Experimental and simulated data at the same detector. a) Experimental data. b) Computationally simulated data.*

Figure 3 compares time resolved experimental and simulated data at the same detector. Computational simulations were performed for the model target which has the same properties as the one which produces the signal on Figure 3-a).

Therefore, the *central procedure* before applying inversion methods is the data pre-processing. So that the pre-processed data would look somewhat similar with computationally simulated data. This procedure is heuristic and cannot be rigorously justified. The pre-processed data were used as input for the globally convergent algorithm. Our data pre-processing consists of six steps described below. We do not describe steps 1-3, 6 in detail here, since they are straightforward. However, steps 4-6 are *completely new*.

*Step 1. Off-set correction.* The acquired signals are usually shifted from the zero mean value. This can be corrected by subtracting the mean value from them.

*Step 2. Time-zero correction.* Time-zero refers to the moment at which the signal is emitted from the transmitter. The recorded signals may be shifted in time. We use the direct signals from the transmitter to the detector to correct the time-zero.

*Step 3. Source shift.* As mentioned above, the horn antenna in our experiments is placed between the targets and the measurement plane. However, in data calibration, we need to simulate the data for the case when the measurement plane is between the horn and the targets. Therefore, we artificially "shift" the horn in the positive $z-$direction such that it is 0.4 m further than the measurement plane from the targets. It is done by shifting the whole time-dependent data by a number of samples which corresponds to the shifted distance.

*Step 4. Extraction of scattered signals.* Apart from the signals backscatter by the targets, our measured data also contain various types of signals as mentioned above. What we need, however, is the scattered signals by the targets only. The extraction of these scattered signals for each target is done as follows. First, we exclude the direct signals and the unwanted signals, which come earlier than the scattered signals by the target (see Figures 3-a and 4) by calculating the time of arrival. These unwanted signals are due to the reflection of the direct signals by the metallic structure behind the measurement plane, so we can estimate

24

their times of arrival as we know the distance from the measurement plane to this structure.

We have observed that the scattered signals by the target are the strongest peaks of the remaining ones. Hence, after removing the aforementioned signals, we first detect, for each detector position, the strongest negative peak. Next, we consider the strongest negative peak. Suppose that the amplitude of the first negative peak prior the strongest is less than 80% of the strongest one (see Figure 3-a)). Next, the scattered signals by the target are taken as 7 peaks (4 negative peaks and 3 positive peaks) starting from that first negative peak prior to the strongest one. However, if the amplitude of the first negative peak prior to the strongest one is greater or equals 80% of the strongest negative peak, then we start from the second negative peak prior to the strongest one. The reason for choosing 7 peaks for the scattered signals is due to the fact that the incident pulses also contain 7 strong peaks. We note that having the scattered signals by the target, we can easily determine the distance from its front side to the measurement plane by calculating the time of arrival. We use the resulting signal for data propagation.

The next round of extraction of scattering signals comes after data propagation. In this case we choose the largest negative peak. Next, we choose the closest negative peak to the left of it and set to zero the signal to the left of this second peak. We apply the Laplace transform (6) to the resulting curve to get the boundary data for the function $w(x, s)$.

*Step 5. Data propagation.* After getting the scattered signals, the next step of data pre-processing is to propagate the data closer to the targets, i.e. to approximate the scattered waves on a plane closer to the targets, compared to the measurement plane. There are two reasons for doing this. The first one is that since the Laplace transform decays exponentially in terms of the time delay, which is proportional to the distance from the targets to the measurement plane, then the amplitude of the data after the Laplace transform on the measurement plane is very small and can be dominated by the computational error. The second reason is that this propagation procedure helps to reduce the computational cost substantially as the computational domain $\Omega$ is reduced. We have also observed that the data propagation helps to reduce the noise in the measured data.

*Step 6. Data calibration.* Finally, since the amplitude of the experimental incident and scattered waves are usually quite different from simulations, we need to bring the former to the same level of the amplitude as the latter. This is done using a known target referred to as *calibrating object*.

It is clear from Figure 6 that the Laplace transform of the propagated data looks more concentrated and less noisy than the Laplace transform of the measured data.

## 5.3 Data propagation

We now describe in detail our data propagation procedure of the above Step 5 (section 5.2). Denote by $P_m$ the measurement plane and by $P_p$ the propagation plane, which is closer to the targets than $P_m$. Without a loss of the generality, we denote by $P_m = \{z = a\}$ and $P_p = \{z = 0\}$, where the number $a > 0$. Moreover, denote by $\Gamma = (-0.5, 0.5) \times (-0.5, 0.5)\} \subset \mathbb{R}^2$ the scanning area of the detector on the plane $P_m$. Let $\Gamma_m = \{(x, y, a) \in \mathbb{R}^3 : (x, y) \in \Gamma\}$
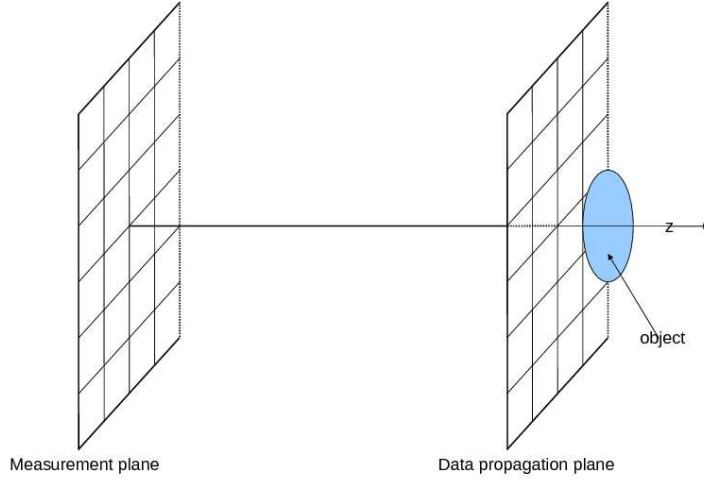
Figure 4: *Schematic diagram of data propagation.*

and $\Gamma_p = \{(x, y, 0) \in \mathbb{R}^3 : (x, y) \in \Gamma\}$. We also denote by $u^s(x, t)$ the scattered wave. Note that the medium between $P_m$ and $P_p$ is homogeneous with $\varepsilon = 1$ and the scattered wave $u^s$ propagates in the direction from $P_p$ to $P_m$. The goal of the data propagation is to approximate $u^s\big|_{\Gamma_p \times (0, \infty)}$ from the measured data $\widetilde{g}(x, y, t) := u^s\big|_{\Gamma_m \times (0, \infty)}$.

To do this, we make use of a time reversal method. Its idea is to reverse the scattered wave in time via solution of an initial boundary value problem for the time-reversed wave function. We proceed as follows.

Consider the domain $D := \{x = (x, y, z) \in \mathbb{R}^3 : (x, y) \in \Gamma, b < z < a\}$ with $b < 0$. Note that $\Gamma_p \subset D$. The reason for choosing this larger domain is that we need to assign boundary conditions at $\partial D$. Since short pulses are used as incident waves, it is reasonable to assume that the scattered wave $u^s$ in the domain between $P_m$ and $P_p$ vanishes along with its time derivative $u^s_t$ after some time $T$, i.e. $u^s(x, t) = 0$ for $x \in D, t > T$. Therefore, in the following we consider only the finite time interval $(0, T)$. Denote $\tau := T - t$. Then the time-reversed wave function $u^r(x, \tau) := u^s(x, t)$ satisfies the homogeneous wave equation. Moreover, it propagates in the negative $z$ direction, i.e. from $P_m$ to $P_p$. We assume that the function $u^r$ satisfies the absorbing boundary condition at $\Gamma_b := \{(x, y, b) : (x, y) \in \Gamma\}$. On $\Gamma_b$, far from our propagation plane, this boundary condition means, heuristically, that we "send back" the original scattered wave $u^s$ recorded at $P_m$. On the other hand, we impose the zero Neumann boundary condition at the rest of the boundary of $D$, except of $\Gamma_m$. Denote $Q_T = D \times (0, T)$ and $\Gamma_3 := \partial D \setminus (\Gamma_m \cup \Gamma_b)$. We obtain the following problem for the function
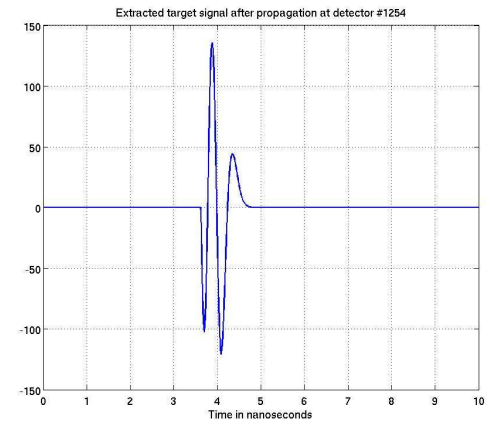
26
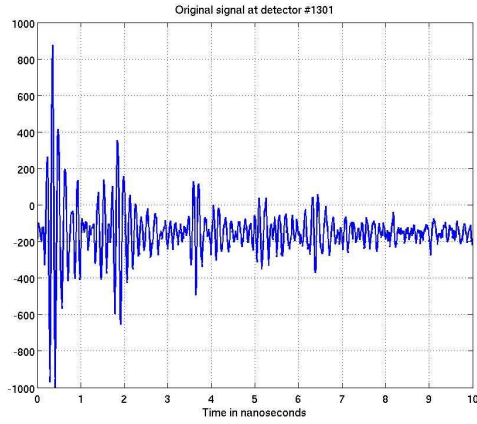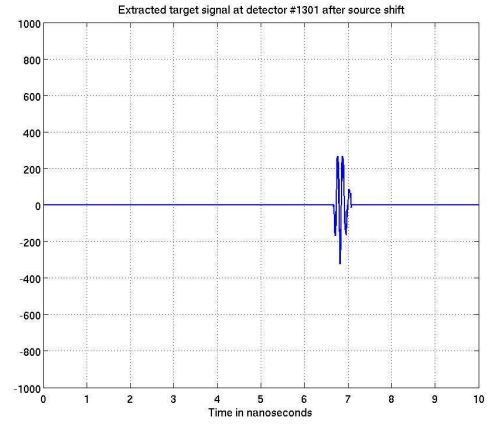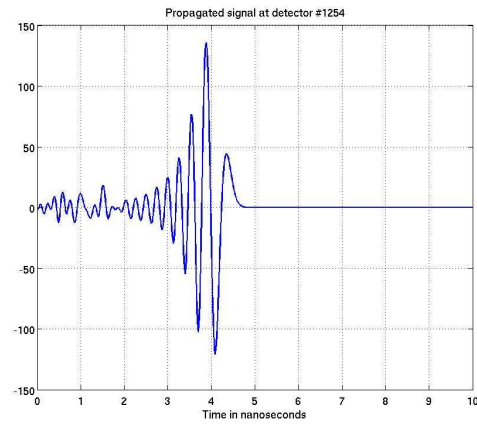
Figure 5: *Extraction of scattered signals. a) Original signal at a detector. b) Signal extracted from a) after shifting the source. c) Propagated signal. In propagation, extracted signals on all detectors were used. c) Propagated signal detected at some point. d) Extracted signal of c)*
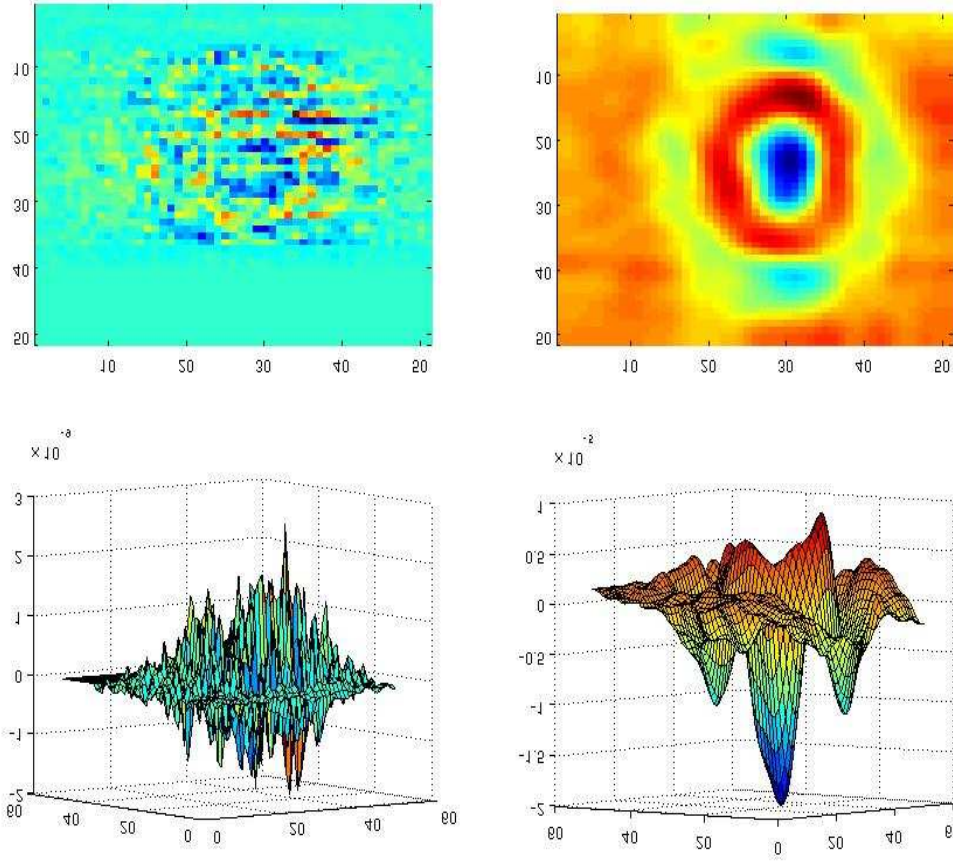
Figure 6: *2D and 3D representations of the Laplace transform (6) at a certain value of $s > 0$ of the data at the measurement plane (left panel) and the propagated plane (right panel). It is clear from this figure that the Laplace transform of the propagated data looks more concentrated and less noisy than the Laplace transform of the measured data.*

$u^r(x, \tau)$

$$u^r_{\tau\tau} = \Delta u^r, (x, \tau) \in Q_T, \tag{62}$$

$$u^r(x, 0) = u^r_\tau(x, 0) = 0, x \in D, \tag{63}$$

$$u^r\big|_{\Gamma_m \times (0,T)} = \widetilde{g}(x, y, T - \tau), \tag{64}$$

$$(\partial_\nu u^r + \partial_\tau u^r)\big|_{\Gamma_b \times (0,T)} = 0, \tag{65}$$

$$\partial_\nu u^r\big|_{\Gamma_3 \times (0,T)} = 0. \tag{66}$$

Theorem 1 below shows the stability of the problem (62)–(66). This theorem is proven via a modification of the energy estimates method [57], and it can be extended to more general domains and more general hyperbolic operators. For brevity we are not concerned here with minimal smoothness assumptions and leave aside the question of existence. We conjecture that it can be addressed via the technique of chapter 4 of [57].

**Theorem 1** *Assume that there exists a solution $u^r \in H^2(Q_T)$ of the problem (62)-(66). Also, assume that the function $\widetilde{g} \in H^2(\Gamma_m \times (0, T))$ and there exists such a function $F \in H^2(Q_T)$ that*

$$F(x, 0) = F_\tau(x, 0) = 0, (\partial_\nu F + F_\tau)\big|_{\Gamma_b \times (0,T)} = 0, \partial_\nu F\big|_{\Gamma_3 \times (0,T)} = 0,$$
$$F\big|_{\Gamma_m \times (0,T)} = \widetilde{g}(x, t), \quad \|F\|_{H^2(Q_T)} \leq C \|\widetilde{g}\|_{H^2(\Gamma_m \times (0,T))},$$

*where $C > 0$ is a certain number. Then that solution $u^r$ is unique and the following stability estimate holds with a constant $C_1 = C_1(C, Q_T) > 0$ depending only on the listed parameters*

$$\|u^r\|_{H^1(Q_T)} \leq C_1 \|\widetilde{g}\|_{H^2(\Gamma_m \times (0,T))}.$$

By solving the problem (62)–(66), we obtain an approximation of $u^r(x, \tau)$ and then obtain an approximation of $u^s$ for $x \in \Gamma_p$. We use the finite difference method to solve this problem.

## 5.4 Data calibration

Usually the experimental data have quite different amplitudes compared to the simulations. Figure 7 shows that the minimal value of the Laplace transform of the propagated measured data is approximately $-2 \times 10^{-5}$, whereas the minimal value for simulated data is about $-5 \times 10^{-9}$. We choose a number, which is called *calibration factor,* to scale the measured data to the same scaling as in our simulations. To do this, we make use of the measured data of a single calibrating object whose location, shape, size and material are known. The word "single" is important here to ensure that the calibration procedure is unbiased, i.e. it remains the same for all targets.

First, we computationally simulate the data on $\Gamma_p$ for the calibrating object by solving the problem (68)–(73), see section 2.6. Next, we compute the Laplace transform (6) of
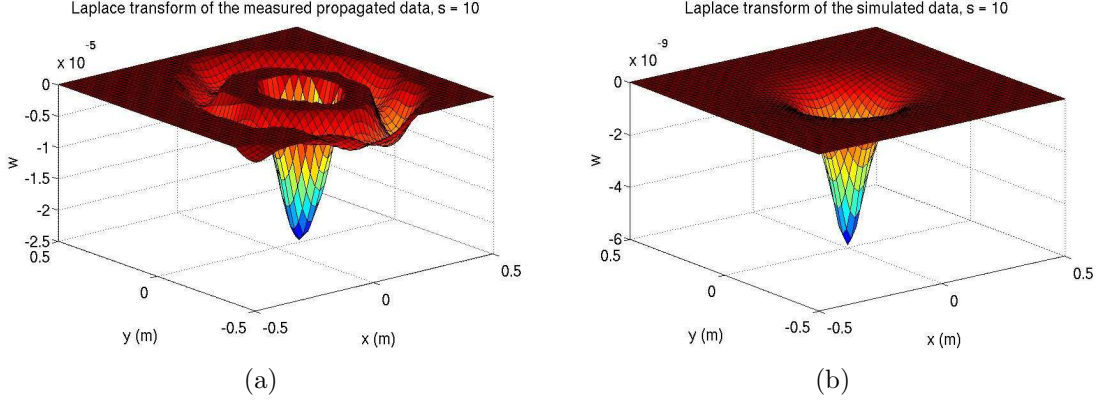
29

Figure 7: *Laplace transform (6) of the scattered wave on the propagation plane $P_p$. a) Measured data. The maximal amplitude of the peak is $2.5 \times 10^{-5}$. b) Simulated data. The maximal amplitude of the peak is $5 \times 10^{-9}$. Thus, the data calibration is necessary.*

this computationally simulated solution. Below we work with $s \in [\underline{s}, \overline{s}]$. Numbers $\underline{s}, \overline{s}$ are chosen numerically. Denote by $w_{sim}^t(x, s)$, $w_{sim}^s(x, s)$ and $w_{sim}^i(x, s)$ respectively the Laplace transforms of the total wave, the scattered wave and the incident wave of the simulated solution for the calibrating object. Clearly, $w_{sim}^s(x, s) = w_{sim}^t(x, s) - w_{sim}^i(x, s)$. It can be proved that $w_{sim}^s(x, s) \leq 0$. Figure 7-b) displays the function $w_{sim}^s(x, s)$ for $x \in \Gamma_p$ and qualitatively this is a typical behavior for all targets. Let

$$d_{sim,s} = \min_{\Gamma_p} w_{sim}^s(x, s).$$

Next, for $x \in \Gamma_p$ let $w_{exp}^s(x, s)$ be the Laplace transform of the propagated experimental data for the calibrating object, see Figure 7-a). Denote

$$d_{exp,s} = \min_{\Gamma_p} w_{exp}^s(x, s).$$

The number $d_{sim,s}/d_{exp,s}$ is used as the calibration factor for all targets at pseudo-frequency $s$. That means, the propagated measured data of all targets are multiplied by this calibration factor before being used in the inversion algorithm.

We have two types of targets: dielectric and metallic targets. We have observed that two different calibration factors should be used for these two types of targets, because the signals from them have different levels of amplitude. First of all, we differentiated these two types of targets by comparing the amplitudes of the recorded signals. Indeed, we have consistently observed that the maximal values of amplitudes of measured signals are at least two times larger for metallic targets than for dielectric ones on those positions of detectors which are most sensitive to the presence of targets. Next, we chose in each type a known object as the calibrating object. In other words, we should use a dielectric calibrating object for all dielectric targets and another metal calibrating object for all metallic targets. As to metallic targets, we have established in [17] that one should use the so-called *appearing dielectric*

30

*constant*, whose values are

$$\varepsilon_r \,(\text{metal}) \in [10, 100]\,. \tag{67}$$

The value of $\varepsilon_r\,(x)$ for the dielectric calibrating object was taken as $\varepsilon_r\,(x) = 4.28$ inside that target and $\varepsilon\,(x) = 1$ outside of it. For the metallic calibrating object, as suggested by (67), we took $\varepsilon_r\,(x) = 12$ inside and $\varepsilon\,(x) = 1$ outside of it.

## 5.5 Dimensionless variables

The spatial dimensions in our experiment were given in meters. Since the scanning step in our measured data was 0.02 m in both $x$ and $y$ directions, we chose the dimensionless spatial variable $x'$ to be $x' = x/1(m)$. Next, to scale the wave speed to be 1 in the homogeneous medium, as in our simulations, we chose the dimensionless time $t'$ by $t' = 0.3t$ where $t$ is the time given in nanoseconds (ns). The factor 0.3 is the speed of light in meters per nanosecond in the free space. For the simplicity of notations, we use $x$ and $t$ again to denote the dimensionless variables.

## 5.6 Data simulation

As it is clear from sections 5.2-5.4, we need to computationally simulate the data via solving the forward problem (1), (2). On the other hand, it is clear that it is impossible to solve equation (1) in the infinite space $\mathbb{R}^3$. Therefore, we have replaced $\mathbb{R}^3$ with a finite prism $G$ and used absorbing boundary conditions on those sides of this prism, which are perpendicular to $z-$axis, and used zero Neumann boundary condition at the rest of the boundary of this prism.

Although a point source is used in the forward model (1), (2) for theoretical analysis, we make use of an incident plane wave in our numerical implementation. The prism $G$ is

$$G := \{x = (x, y, z) \in \mathbb{R}^3 : X_l \le x \le X_u, Y_l \le y \le Y_u, Z_l \le z \le Z_u\}.$$

Denote by $\partial G_z^l := \{z = Z_l\}$, $\partial G_z^u := \{z = Z_u\}$ and $\partial G_{xy} = \partial G \setminus (\partial G_z^l \cup \partial G_z^u)$. An incident plane wave of a short time period is excited at $\partial G_z^u$ and propagates in the negative $z$ direction. At the plane $\partial G_z^l$ we assume that the absorbing boundary condition is satisfied, and at $\partial G_{xy}$ we assign the homogeneous Neumann boundary condition. More precisely, we solve the following problem

$$\begin{align}
\varepsilon_r(x)u_{tt}(x,t) &= \Delta u(x,t), (x,t) \in G \times (0,T), \tag{68}\\
u(x,0) &= 0, \quad u_t(x,0) = 0, x \in G, \tag{69}\\
\partial_\nu u &= f(t), (x,t) \in \partial G_z^u \times (0,t_1), \tag{70}\\
\partial_\nu u &= -u_t, (\mathbf{x},t) \in \partial G_z^u \times (t_1,T), \tag{71}\\
\partial_\nu u &= -u_t, (x,t) \in \partial G_z^l \times (0,T), \tag{72}\\
\partial_\nu u &= 0, (x,t) \in \partial G_{xy} \times (0,T), \tag{73}
\end{align}$$

31

where $\nu$ is the outward unit normal vector of $\partial G$ and $t_1 := 2\pi/\omega$ is the duration of the excitation of the incident plane wave. Function $f$ is the incident waveform chosen by

$$f(t) = \sin(\omega t), 0 \leq t \leq t_1 = 2\pi/\omega.$$

We have chosen $\omega = 30$. The forward problem (68)–(73) is solved via the hybrid FEM/FDM method described in [1].

Because of our specific experimental arrangement, we now specify the domain $G$. We also specify the computational domain $\Omega$ where the inverse problem is solved. Given the estimated distances from the targets to the measurement plane, which were about 0.8 m, we propagated the measured data from the measurement plane $P_m = \{z = 0.8\}$ to the propagated plane $P_p = \{z = 0.04\}$. This means that the distance from the front sides of the targets to the backscattering boundary of our inversion domain was about 0.04 m. The reason for choosing this distance was due to good reconstruction results we have obtained for several non-blind targets. The domain $\Omega$ was chosen by

$$\Omega = \{x = (x, y, z) \in (-0.5, 0.5) \times (-0.5, 0.5) \times (-0.1, 0.04)\}. \tag{74}$$

For solving the forward problem (68)–(73), using the hybrid FDM/FEM method, we choose the domain $G$ as

$$G = \{x = (x, y, z) \in (-0.56, 0.56) \times (-0.56, 0.56) \times (-0.16, 0.1)\}. \tag{75}$$

This domain $G$ was decomposed into two subdomain: $G = \Omega \cup (G \setminus \Omega)$. We recall that $\varepsilon(x) = 1$ in $G \setminus \Omega$. Therefore, it is only necessary to solve the inverse problem in $\Omega$. In $\Omega$ we use a FEM mesh with tetrahedral elements, while in $G \setminus \Omega$ we use a FDM mesh with the mesh size of $0.02 \times 0.02 \times 0.02$ in Test 1 and $0.01 \times 0.01 \times 0.01$ in Test 2 below. The reason for using the FEM mesh in $\Omega$ is that it is possible to refine the reconstruction using adaptive mesh refinement.

The time interval $(0, T)$ in the forward problem (68)–(73) was chosen equal to $(0, 1.2)$. Since the explicit scheme in time was used, the time step size was chosen as $\Delta t = 0.0015$ which satisfies the CFL stability condition. The pseudo frequencies $s_n$ were chosen from $\underline{s} = 8$ to $\bar{s} = 10$ with the step size $h = 0.05$. This pseudo frequency interval was chosen because it gave good reconstructions of the non-blind targets.

## 5.7   Complementing backscattering data

Consider the boundary function $\psi(x, s)$ in (19). We recall that only backscatter signals were measured in our experiments. This means that after data propagation, the function $\psi(x, s)$ was known only on the side $\Gamma_p = \{x \in \partial\Omega : |x|, z = 0.04\}$ of $\Omega$. As in [16], we replace the missing data on the other parts of $\partial\Omega$ by the corresponding solution of the forward problem in the homogeneous medium. In other words, in our computations, function $\psi$ is given by

$$\psi(x, s) = \begin{cases} \psi_{prop}(x, s), x \in \Gamma_p, s \in (\underline{s}, \bar{s}), \\ \psi^i_{unif}(x, s), x \in \partial\Omega \setminus \Gamma_p, s \in (\underline{s}, \bar{s}), \end{cases} \tag{76}$$
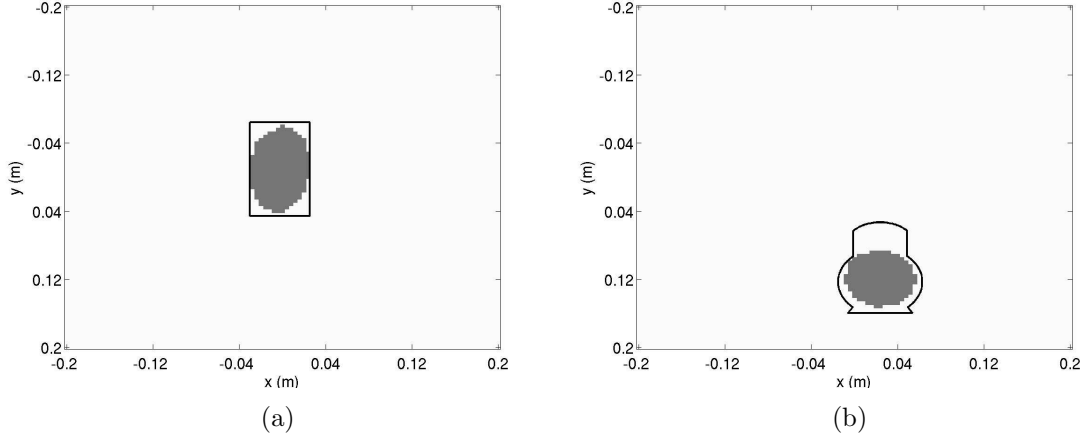
Figure 8: *Estimation of $x, y$ sizes of targets. a) Metallic cylinder. b) Wooden doll whose bottom is filled with the sand and air is in the top.*

where $\psi_{prop}$ is the function $\psi$ computed from the propagated measured data at $\Gamma_p$ and $\psi^i_{unif}$ is computed from the simulated solution of the problem (68)–(73) with $\varepsilon(x) \equiv 1$ in the wave equation (68).

Recall that our measured data were collected with the step size of 0.02 m in $x$ and $y$ directions. To obtain the data at the same grid size as in our computational domain, we applied the linear interpolation to the Laplace transform of the propagated measured data.

## 5.8   Postprocessing

### 5.8.1   Estimation of the $xy$ projection

We have observed that the $xy$ projection of a target can be roughly estimated directly from the propagated data. Let $\bar{s}$ be the upper bound of the pseudo frequency interval on which we apply the globally convergent method. Define $\Gamma_T$ as

$$\Gamma_T = \{(x, y) : v_{prop}(x, y, z_{prop}, \bar{s}) < 0.85 \min v_{prop}(x, y, z_{prop}, \bar{s})\}, \qquad (77)$$

where $z_{prop} = 0.04$ is the value of $z$ on the propagated plane $P_p$ and $v_{prop}$ is the function $v = \ln(w)/s^2$ which is constructed from the propagated measured data on the propagation plane $\Gamma_p$. The truncation value 0.85 was chosen based on trial-and-error tests on some non-blind targets with known sizes. We observed that $\Gamma_T$ provides a good approximation for the $xy$ projection of a target. Note that the same truncation was applied to blind targets as well. Hence, it is not biased.

### 5.8.2   Estimation of the $z-$size and the shape

The thing left to estimate is the size in the $z-$direction, i.e. the depth in the $z-$direction. Along with the above estimates of $x, y-$sizes this is supposed to provide an estimate of the

shape of the target. The $z-$size is more challenging than $x, y-$sizes. At this point of time we have a postprocessing procedure which sometimes gives us a good estimate of the $z-$size and sometimes underestimates it. We keep working on refining this procedure. The current procedure is as follows.

Let $\varepsilon_{rec}(x)$ be the coefficient $\varepsilon_r(x)$ reconstructed by our globally convergent method. Let $P_{z_0} := \{z = z_0\}$ be the plane where the function $\varepsilon_{rec}(x)$ achieves its maximal value. Then we compute the truncated coefficient function $\widetilde{\varepsilon}_{rec}(x)$ as

$$\widetilde{\varepsilon}_{rec}(x) = \begin{cases} \varepsilon_{rec}(x) \text{ if } \varepsilon_{rec}(x, y, z_0) > \gamma \max \varepsilon_{rec}(x, y, z_0), \\ 1 \text{ otherwise,} \end{cases} \tag{78}$$

where $\gamma \in (0, 1)$ is a truncation factor chosen such that the area of $\{\widetilde{\varepsilon}(x, y, z_0) > 1\}$ is the same as that of $\Gamma_T$, see (77) for $\Gamma_T$. Finally, we approximate the depth in the $z$ direction by truncating $\widetilde{\varepsilon}_{rec}(x)$ by 90% of its maximal value. This truncation value is chosen based on the trial-and-error tests with non-blind targets.

## 5.9    Targets in experiments

We have tested both dielectric and metallic targets. Recall that in metallic targets $\varepsilon_r \in [10, 30]$ is the so-called *appearing* dielectric constant of metals, see (67). In some experiments we had only a single target and in others we had two targets simultaneously with the 6 centimeters distance between their surfaces. We had both non-blind and blind targets. "Blind" means that the computational group did not have any information about those targets prior to conducting computations. Data for non-blind targets were used for calibration. Clearly blind cases are the *most challenging* ones. In blind cases we have conducted computations first. And only in a few weeks after this we got the true information about targets. The information was delivered by Mr. Steven Kitchin, an engineer who was working part time on this grant. He has collected these data.

## 5.10    Results of the globally convergent method

Tables 1-5 of this section are quite informative ones. Indeed, they provide the cumulative results of our studies of experimental data.

### 5.10.1    Tables

We had total fourteen (14) targets. Three (3) of them were heterogeneous ones: (a) wooden doll with air inside, (b) the same doll with a piece of metal inside and (c) the same doll, whose bottom part is filled with sand. We believe that these heterogeneous targets model IDEs, since many of IEDs are mixtures of several substances. Table 1 provides a cumulative view on these targets.

Table 1: *Targets*

| Number of targets | Blind | Non-blind | Heterogeneous |
|---|---|---|---|
| 14 | 8 | 6 | 3 |

Table 2: *Targets in detail. The true information about blind targets 7-14 was obtained only after computations were conducted. Blind targets 12,13,14 are heterogeneous ones.*

| target number | details | blind | non-blind |
|---|---|---|---|
| 1 | prism, oak | no | yes |
| 2 | prism, pine | no | yes |
| 3 | prism, pine | no | yes |
| 4 | sphere, metal | no | yes |
| 5 | cylinder, metal | no | yes |
| 6 | cylinder, metal | no | yes |
| 7 | prism, dielectric | yes | no |
| 8 | prism, metal | yes | no |
| 9 | two prisms, metals | yes | no |
| 10 | prism, metal | yes | no |
| 11 | two prisms, dielectrics | yes | no |
| 12 | wooden doll, air inside | yes | no |
| 13 | wooden doll, metal inside | yes | no |
| 14 | wooden doll, sand inside | yes | no |

Table 2 lists all targets of out tests. Target 3 is the same as target 2, but on a different distance from the measurement plane. Target 6 is the same as target 5, but again on a different distance from the measurement plane.

Rerfactive indices $n = \sqrt{\varepsilon_r}$ of dielectric targets were measured directly after computations were conducted. We define the computed refractive index of a target as

$$n_{comp}\left(\text{target}\right) = \max_{\overline{\Omega}} \sqrt{\varepsilon_{r,comp}\left(x\right)}, \tag{79}$$

where $\varepsilon_{r,comp}\left(x\right)$ is the computed function $\varepsilon_r\left(x\right).$ We have observed in our computations that the maximal value in (79) is always reached within the imaged target, which follows from (78). Table 3 gives an information about measured and computed refractive indices of dielectric targets.

Table 3: *Drectly measured and computed refractive indices n of targets. "X/Y" in target 11 means that X corresponds to the upper target and Y corresponds to the lower target. Targets 7,10,11,12,14 are blind ones. Targets 12,14 are heterogeneous. Tests 1,2,3,4 differ from each other by different parameters of the inversion procedure.*

| target number | 1 | 2 | 3 | 7 | 11 | 12 | 14 | Average error |
|---|---|---|---|---|---|---|---|---|
| measured | 3.11 | 1.84 | 1.84 | 3.14 | 1.84/3.14 | 1.89 | 3.1 | |
| error | 19% | 18% | 18% | 28% | 18%/28% | 30% | 26% | 23% |
| test 1 | 1.92 | 1.8 | 1.81 | 1.83 | 1.98/1.96 | 1.86 | 1.92 | |
| error | 9% | 3.2% | 1.6% | 16.9% | 7.6%/9.1% | 1.6% | 9.3% | 7.16% |
| test 2 | 2.08 | 2.01 | 2.07 | 3.22 | 3.21/2.03 | 1.83 | 3.2 | |
| error | 1.4% | 9.2% | 12.5% | 3.7% | 20.1%/5.4% | 3.2% | 4.8% | 7.5% |
| test 3 | 2.03 | 1.96 | 1.65 | 3.1 | 3.2/3.13 | 1.85 | 2.05 | |
| error | 3.9% | 6.5% | 11.5% | 1.9% | 19.5%/0.5% | 3.1% | 2.4% | 6.0% |
| test 4 | 2.02 | 2.01 | 2.02 | 2.03 | 2.08/2.06 | 1.97 | 2.02 | |
| error | 4.4% | 9.2% | 9.8% | 5.4% | 13%/3.9% | 4.2% | 9.6% | 7.43 |

## THREE IMPORTANT OBSERVATIONS FROM TABLE 3:

1. The average error in computations is at least three (3) times less than the average error of direct measurements.

2. Refractive indices of targets are imaged with a good accuracy, including *the most challenging blind cases* 7,11,12,14. This is especially true for cases of a single target: 1,2,3,7,12,14.

3. The most interesting cases 12,14 of *blind heterogenous* targets, which model heterogeneous IEDs, demonstrate a good accuracy: the computational error is between 3.1% and 9.6%.

Table 4: *Computed appearing dielectric constants $\varepsilon_r^{comp} = \max_{\overline{\Omega}} \varepsilon_{r,comp}(x)$ of metallic targets, see (67). "X/Y" in target 9 means that X corresponds to the upper target and Y corresponds to the lower target. Targets 8,9,13 are blind ones. Target 13 is heterogeneous. Tests 1,2,3,4 differ from each other by different parameters of the inversion.*

| target number | 4 | 5 | 6 | 8 | 9 | 10 | 13 |
|---|---|---|---|---|---|---|---|
| test 1 | 14.37 | 16.93 | 16.45 | 25 | 12.66/13.1 | 13.61 | 13.56 |
| test 2 | 15.18 | 23.33 | 25 | 25 | 40.53/41.78 | 14.13 | 14.05 |
| test 3 | 7.59 | 10.76 | 19.5 | 19.5 | 11.07/13.1 | 8.12 | 7.89 |
| test 4 | 15 | 15 | 15 | 15 | 13.53/14.06 | 15 | 14.33 |

### THREE IMPORTANT OBSERVATIONS FROM TABLE 4:

1. We can confidently image large contrasts in inclusions. This is hard to do for locally convergent methods.

2. Comparison of tables 3 and 4 demonstrates that we can confidently distinguish between dielectrics and metals.

3. The *blind heterogeneous* target 13 was a wooden doll with a piece of metal inside. It models the case of an IED in which an explosive is covered by an innocent material. Nevertheless, our calculations clearly demonstrate the presence of a metal.

## 5.11   Some specifications for the adaptivity

As it was pointed out in Introduction and in section 4, we have applied a two-stage numerical procedure. The first stage is the globally convergent numerical method. This stage has provided accurate values of refractive indices $n = \sqrt{\varepsilon_r}$ of dielectric targets and appearing dielectric constants $\varepsilon_r$ of metallic targets. It is important to point out that the theory guarantees that the first stage provides points in a small neighborhood of the exact coefficient. Therefore, the Tikhonov functional does not have local minima in this neighborhood. The second stage is the locally convergent adaptivity method. This method uses the solution obtained on the first stage as the starting point for iterations. Adaptivity refines images via providing accurate shapes of targets. This is done via sequential minimization of the Tikhonov functional on a sequence of locally refined meshes of finite elements.

Data pre-processing procedure for the adaptivity is a little bit different from that of the first stage. This is because the adaptivity works in time domain, whereas the globally convergent method works in Laplace transform domain. In addition, the image postprocessing procedure of the adaptivity is different from the one of the first stage. Thus, we describe in this subsection those procedures. We work with propagated data and $\Omega, G, \Gamma_p$ are the same as in subsections 6.6, 6.7. Other details can be found in our paper [3].

### 5.11.1 Data calibration

Let the function $g_{\text{exper}}(x,t)$, $x \in \Gamma_p, t \in (0,T)$ be our propagated experimental data. This function is given only on grid points $(x_i, t_j)$. We compute the maximal value of this function,

$$g_{max} = \max_{(x_i,t_j)} g_{\text{exper}}(x_i, t_j).$$

Usually the number $g_{max}$ is quite large. Next, let $u_{sim}(x,t)$ be the function which is computed via solving the problem (68)–(73) where $\varepsilon_r(x)$ is the function $\varepsilon_r(x)$ computed by the globally convergent method. Let

$$u_{max} = \max_{\Gamma_p \times [0,T]} u_{sim}(x, t).$$

Define

$$r = \frac{u_{max}}{g_{max}}.$$

Next, we assign

$$u_{incl}(x_i, t_j) := r \cdot g_{\text{exper}}(x_i, t_j)$$

and use the function $g_{incl}(x_i, t_j)$ as our data at $\Gamma_p$.

### 5.11.2 Data immersing

The final step of data preprocessing, the so-called "immersing procedure", which is also heuristic and is done as described below. This procedure does two things:

- immerses the data $g_{incl}(x,t)$ into computationally simulated ones;

- extends the data $g_{incl}(x,t)$ from $\Gamma_p$ to larger rectangle $\Gamma_1$,

$$\Gamma_1 = \{(x,y) \in (-0.56, 0.56) \times (-0.56, 0.56), z = 0.04\}.$$

To explain the necessity of such data extension, we refer to (74), (75) and note that the domain $\Omega$ is smaller than the domain $G$ and $\Gamma_1$ is the orthogonal projection of $G$ on the plane $\{z = 0.04\}$. On the other hand, we need the data at $\Gamma_1$ to solve the so-called adjoint problem which appears in the computation of the gradient of the Tikhonov functional.

We define our immersed function $u_{immers}(x,t)$ for $(x,t) \in \Gamma_1 \times (0,T)$ as

$$u_{immers}(x,t) = \begin{cases} g_{incl}(x,t), & \text{if } x \in \Gamma_p \text{ and } g_{incl}(x,t) \geq \beta \max_{\overline{\Gamma}_p} g_{incl}(x,t), \\ u_{sim}(x,t), & \text{if } x \in \Gamma \text{ and } g_{incl}(x,t) < \beta \max_{\overline{\Gamma}_p} g_{incl}(x,t), \\ u_{sim}(x,t), & \text{if } x \in \Gamma_1 \backslash \Gamma_p. \end{cases} \qquad (80)$$

We choose the parameter $\beta = 0.5$ in (80) in numerical experiments of section 6.12.

Figures 9 and 10 show that, depending on the parameter $\beta$ in (80), the data immersing procedure not only allows to extend the data from $\Gamma_p$ to $\Gamma_1 \backslash \Gamma_p$ but also make the experimental data usable in our inverse algorithm. Indeed, we note that the experimental data

is measured at a very high frequency, say, $\omega \approx 170$, whereas our simulations are done at $\omega = 30$ in order to reduce the computational cost. Therefore, the experimental data are not compatible with the simulations. Our immersing procedure helps to avoid solving the problem at a very high frequency. After this immersing procedure we solve the inverse problem using the adaptivity.
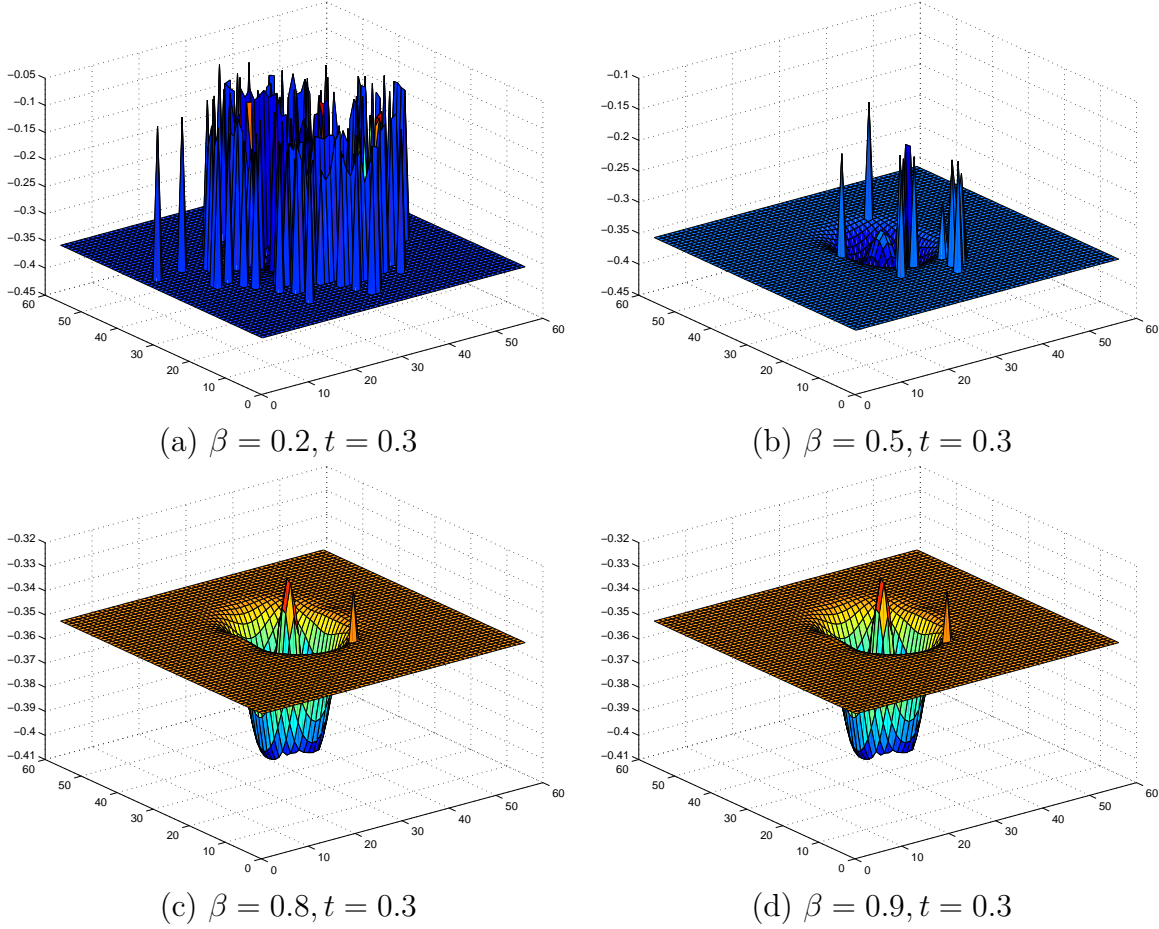


(a) $\beta = 0.2, t = 0.3$

(b) $\beta = 0.5, t = 0.3$

(c) $\beta = 0.8, t = 0.3$

(d) $\beta = 0.9, t = 0.3$

Figure 9: Backscattered immersed data of the second component $E_2$ of electric field for object number 7 (wooden doll, empty inside) of Table 2 for different values of the parameter $\beta$ in (80). Recall that the final time is $T = 1.2$.

### 5.11.3   Postprocessing of results

Let $\varepsilon_r(\mathbf{x})$ be the function obtained in the adaptive algorithm. We form the image of the dielectric targets based on the function $\varepsilon_{r,diel}(\mathbf{x})$,

$$\varepsilon_{r,diel}(x) = \begin{cases} \varepsilon_r(x) & \text{if } \varepsilon_r(x) \geq 0.85 \max_{\overline{\Omega}} \varepsilon_r(x), \\ 1 & \text{otherwise.} \end{cases}$$

40

(a) $\beta = 0.2, t = 0.45$  (b) $\beta = 0.5, t = 0.45$

(c) $\beta = 0.8, t = 0.45$  (d) $\beta = 0.9, t = 0.45$

Figure 10: Backscattered immersed data of the second component $E_2$ of electric field for object 7 (wooden doll, empty inside) of Table 2 for different values of the parameter $\beta$ in (80). Recall that the final time is $T = 1.2$.

As to the metallic targets (i.e., the ones with large computed maximal values of $\varepsilon_r(x)$), we use the function $\varepsilon_{r,metal}(x)$,

$$\varepsilon_{r,metal}(x) = \begin{cases} \varepsilon_r(x) & \text{if } \varepsilon_r(x) \geq 0.3 \max_{\overline{\Omega}} \varepsilon_r(x), \\ 1 & \text{otherwise.} \end{cases}$$
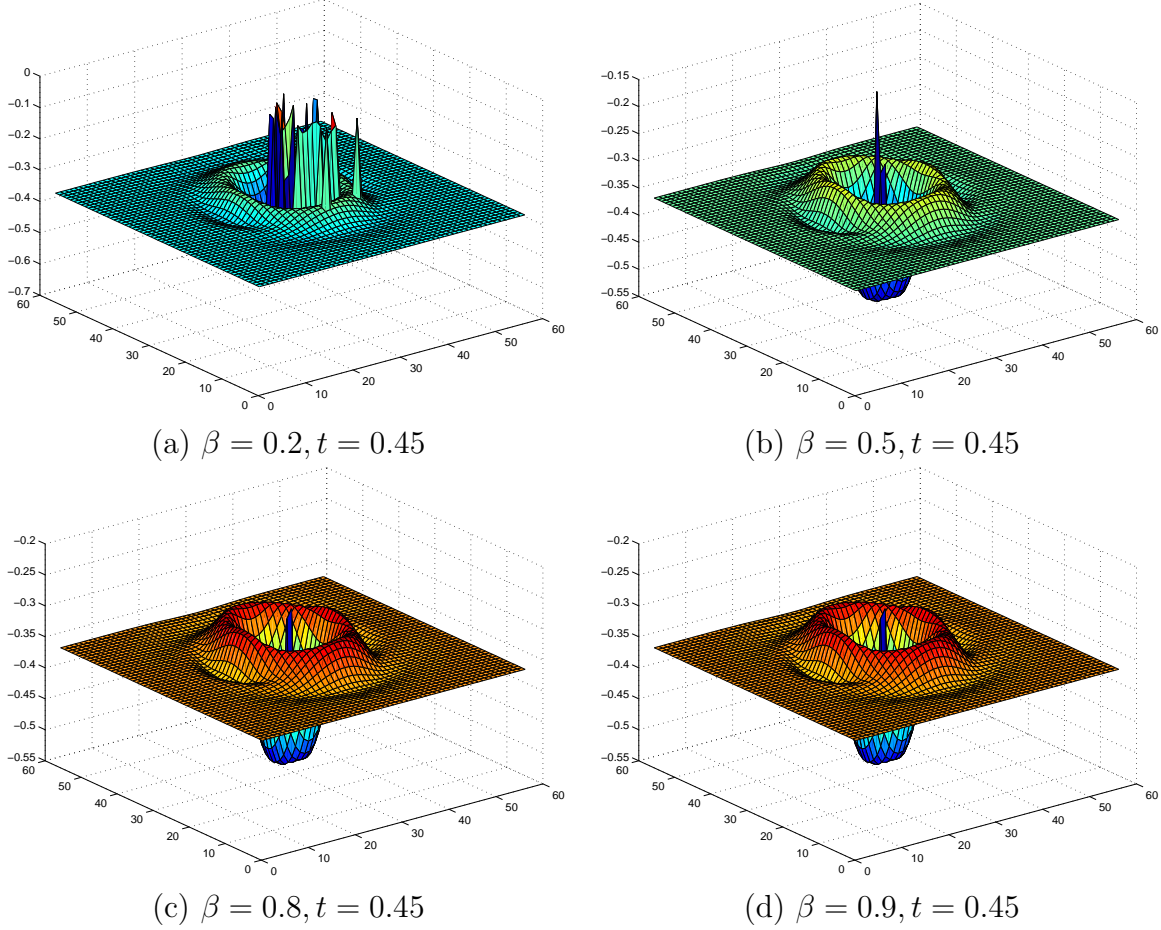
We point out that, in our experience, the adaptive algorithm does not change refractive indices of dielectric targets and appearing dielectric constants of metallic targets.

## 5.12  Images resulting from the two-stage numerical procedure

In this subsection we present some results of our two-stage numerical procedure. The first stage is the globally convergent method and the second stage is the adaptivity. This pro-
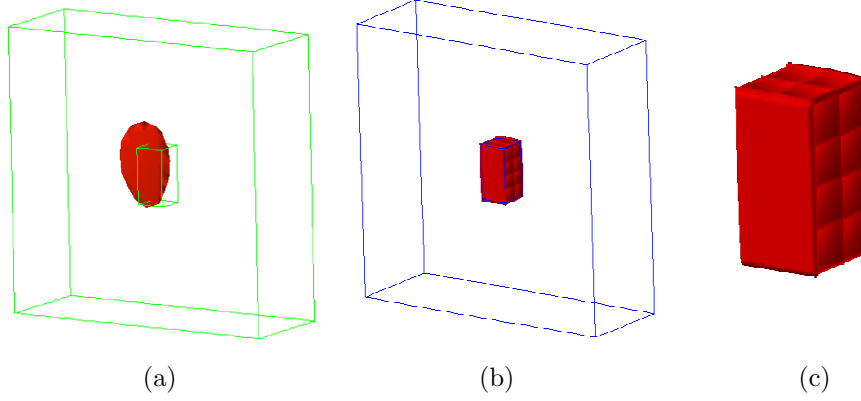
Figure 11: *a) The image of the target #1 (wooden prism, table 2) obtained by the globally convergent method. b) The image of the target #1 obtained by the two-stage numerical procedure. c) Zoomed image of b).*

cedure accurately reconstructs all three components of targets: refractive indices, locations and shapes. In the case of metallic targets refractive indices are replaced with appearing dielectric constants. While refractive indices and appearing dielectric constants were presented above in Tables 3,4, here we present samples of computed images of shapes of targets.

# 6  Targets Buried in the Sand

We have collected some experimental data for the case of targets hidden in the dry sand. Those are both dielectric and metallic targets. The data collection process is continuing. Figure 14 displays our experimental arrangement. Just as in the experimental setup of targets in the air, we have The box on this figure is filled with the dry sand. We have measured the refractive index of sand $n\left(\text{sand}\right) = 2.04$. Hence, $\varepsilon_r\left(\text{sand}\right) \approx 4.16 = \left(2.04\right)^2$. Note that the front surface of the sand box is not flat, which complicates our inversion procedure even more. Targets are immersed in the sand box. The distance between front side of the target and the front side of the sand box varies between 2 cm and 10 cm. Note that we do not know this distance in advance. Rather, we calculate it from our data. To do this, we modify our data pre-processing procedure of section 5 for targets located in the air. The data acquisition process is the same as the one described in subsection 5.1. The data simulation is the same as in section 5.6.

First, we have measured the signal from sand without targets, i.e. the reference signal. Next, we have measure signals for the cases when targets are immersed in the sand, see Figure 14. The major complication here is that the reference signal from the sand is heavily mixed with the signal from the case of targets immersed in the sand. Therefore, the data preprocessing procedure is again the central one here and it should be different from one of the case when targets are placed in air. Just as in section 5, we had six data preprocessing steps:
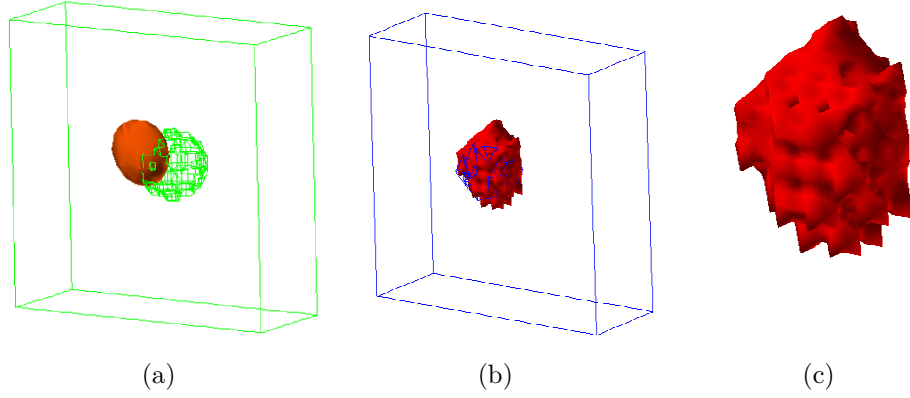
(a)                          (b)                          (c)

Figure 12: *a) The image of the target #4 (metallic sphere, table 2) obtained by the globally convergent method. b) The image of the target #4 obtained by the two-stage numerical procedure. c) Zoomed image of b).*
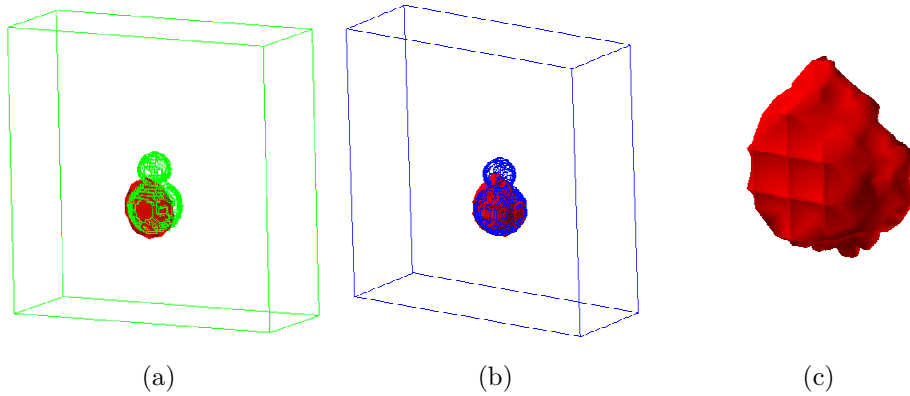


(a)                          (b)                          (c)

Figure 13: *a) The image of the target #12 (wooden doll, table 2) obtained by the globally convergent method. This is a heterogeneous target since air is inside that doll. b) The image of the target #12 obtained by the two-stage numerical procedure. c) Zoomed image of b). One can observe on c) that even the "head" of the doll is appearing, although the shape of this doll is non convex.*
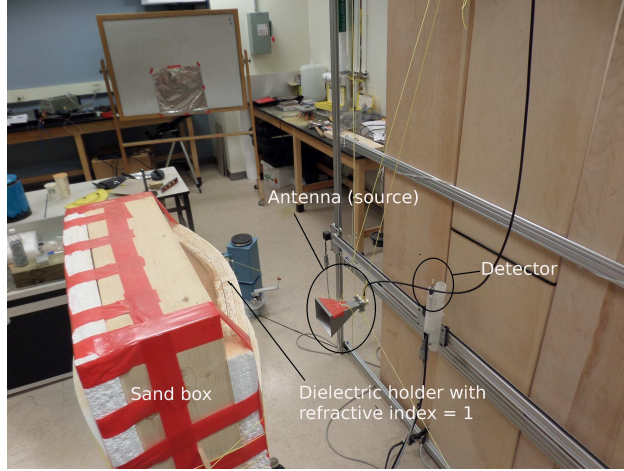
43

Figure 14: *A photograph of the experimental arrangement of the sand box measurements. Targets are immersed in this sand box. The distance between the front side of the target and the front side of the sand box varies between 2 cm and 10 cm. The front surface of the sand box is not flat, which complicates our inversion procedure.*

1. Off-set correction.

2. Time-zero correction.

3. Source shift.

4. Data propagation.

5. Extraction of scattered signals.

6. Data calibration.

While steps #1,2,3,6 were basically the same as ones in section 6, steps 4 and 5 were different and we outline them here. We also note that, unlike targets placed in air, where different calibration factors were found of metallic and dielectric targets, we use here only one calibration factor.

## 6.1 A new idea for data propagation

In section 6 we have used the time reversal method for data propagation, we have observed numerically that it works better than a simpler Stolt migration method on computationally simulated data. However, on experimental data the Stolt migration method works better than the time reversal method. Basically the Stolt migration provides better quality data than time reversal for the case of two targets present simultaneously. The Stolt migration is popular in Geophysics, see [64, 69]. However, in the standard Stolt migration the wave at the initial time is calculated in the whole spatial domain of interest, whereas we calculate

44

the wave only at a plane parallel to the measurement plane but in the whole time interval. This technique is described as follows.

Let $x = (x, y, z)$. We assume that the scattered wave propagates in the positive $z$-direction. Denote by $P_m = \{z = b\}$, $b > 0$, the measurement plane and by $P_p = \{z = a\}$, with $a < b$, the propagated plane, which is closer to the target of interest than $P_m$. We also denote by $u^s(x, t)$ the scattered wave. Our objective here is to determine the function $g(x, y, t) := u^s(x, y, a, t)$, given the measured data $f(x, y, t) := u^s(x, y, b, t)$. We assume that the medium is homogeneous in the half space $z \geq a$ with $\epsilon \equiv 1$. Therefore, $u^s$ is the solution of the following problem:

$$u_{tt}^s - \Delta u^s = 0, \ x \in \mathbb{R}^3, \ z \geq a, \ t \in (0, \infty), \tag{81}$$

$$u^s(x, 0) = u_t^s(x, 0) = 0. \tag{82}$$

Consider the Fourier transform

$$\hat{u}^s(k_x, k_y, z, \omega) = \int\limits_{0}^{\infty} \int\limits_{-\infty}^{\infty} \int\limits_{-\infty}^{\infty} u^s(x, y, z, t) e^{-i(\omega t + x k_x + y k_y)} dx dy dt. \tag{83}$$

It follows from (81) that $\hat{u}^s$ satisfies the equation:

$$\hat{u}_{zz}^s + (\omega^2 - k_x^2 - k_y^2)\hat{u}^s = 0, \ z \geq a, \tag{84}$$

$$\hat{u}(k_x, k_y, z, \omega) = \hat{g}(k_x, k_y, \omega), \tag{85}$$

where $\hat{g}(k_x, k_y, \omega)$ is the Fourier transform (83) of $g(x, y, t)$. We consider two cases:

**Case 1**: $\omega^2 - k_x^2 - k_y^2 < 0$. Keeping in mind that the scattered wave propagates in the positive $z$-direction, the problem (84)–(85) has the following solution

$$\hat{u}_1^s(k_x, k_y, z, \omega) = \hat{g}(k_x, k_y, \omega) \exp\left(-(z - a)\sqrt{k_x^2 + k_y^2 - \omega^2}\right), \ z > a. \tag{86}$$

**Case 2**: $\omega^2 - k_x^2 - k_y^2 \geq 0$. Then the solution $\hat{u}^s$ can be represented as

$$\hat{u}_2^s(k_x, k_y, z, \omega) = \hat{g}(k_x, k_y, \omega) \exp\left(-i(z - a)\sqrt{\omega^2 - k_x^2 - k_y^2}\right), \ z > a. \tag{87}$$

The negative sign in the exponential term in this formula is due to the fact that the scattered wave is out-going in the positive $z$-direction.

Since the solution (86) is exponentially decaying as $z \to \infty$, which represents the evanescent wave, it practically cannot propagate to the measurement plane, which is in the far field zone. Hence,

$$\hat{f}(k_x, k_y, \omega) = \hat{u}_2^s(k_x, k_y, b, \omega) = \hat{g}(k_x, k_y, \omega) \exp\left(-i(b - a)\sqrt{\omega^2 - k_x^2 - k_y^2}\right).$$

Using the inverse Fourier transform, we obtain

$$g(x, y, t) = \iiint\limits_{\omega^2 - k_x^2 - k_y^2 > 0} \hat{f}(k_x, k_y, \omega) e^{i(b-a)\sqrt{\omega^2 - k_x^2 - k_y^2}} e^{i(\omega t + x k_x + y k_y)} dk_x dk_y d\omega. \tag{88}$$

Given the data $f(x, y, t)$ at the measurement plane, we compute $\hat{f}$ as well as $g(x, y, t)$ via (88) using the Fast Fourier Transform.

For each data set, the propagated plane $P_p$ was determined as follows. We first propagated the data to the sand's surface. Using this propagated data, we estimated the burial depths of the targets (subsection 7.2). Next, if the burial depth of the target closest to the sand surface was larger than 4 cm, we propagated the data again from the measurement plane up to the plane $P_p$, whose distance to the front surface of that target was approximately 4 cm. Otherwise, we used the data propagated up to the sand's surface for the next step of data preprocessing. Note that even we propagated the data beyond the sand's surface, we still saw the reflection from the sand's surface in the propagated data since we did not take into account the presence of the sand box in the data propagation, i.e., when propagating the data in the sand, we assumed that $\epsilon = 1$ in the sand. This reflection from the sand's surface was removed when the targets' signals were extracted, see subsection 7.2. Note that the grid points at $P_p$ are the same as the ones at the measurement plane $P_m$. Thus, below we call "detectors" the grid points at the propagated plane $P_p$.
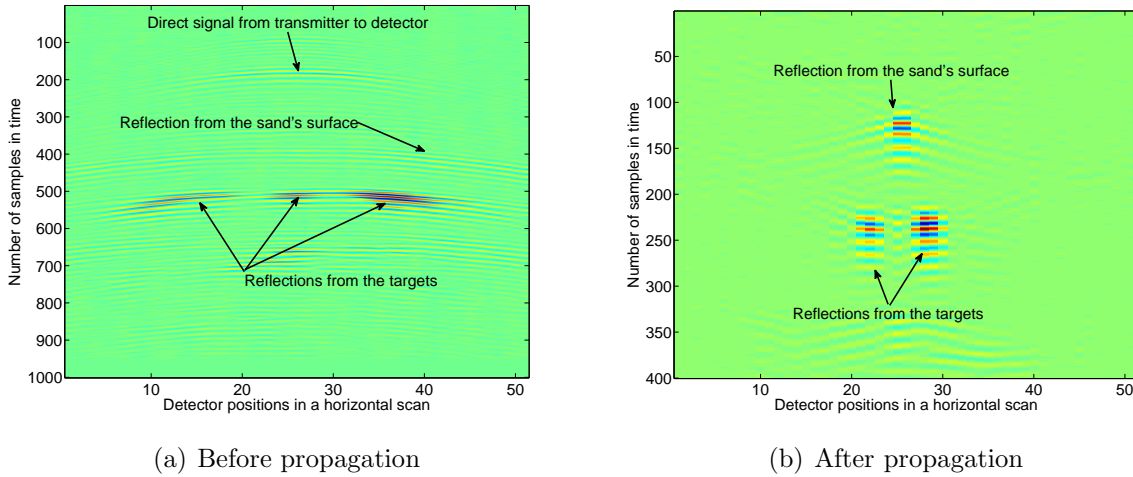


(a) Before propagation

(b) After propagation

Figure 15: Result of the data propagation for signals from two targets buried inside the sand box. The signals of the two targets are well separated from each other as well as from the reflection from the sand's surface after the data propagation.

A result of the data propagation is illustrated in Figure 15. The figure shows a horizontal scan of the sand box containing two buried metallic targets. The horizontal side denotes the indices of the detector's locations and the vertical side denotes time. Time increases from the top to the bottom. The propagation distance, $b - a$, is 0.8 m, which means that the propagated plane $P_p$ almost coincides with the sand's surface. Figure 15(a) shows the original data while Figure 15(b) shows the data after the propagation. As can be seen from these figures, the targets' signals in the original data are smeared out. On the other hand, they are focused after the data propagation making the two targets more clearly distinguished. This is well known for migration methods. Moreover, we can also see that the reflection from

the sand's surface is also more visible after the propagation and is well separated from the targets' signals.

### 6.1.1  Estimation of the burial depth

Since the sand's surface reflects our microwave pulses and these reflected waves arrive at the detectors before the ones reflected from the targets (see Figure 15(b)), the targets' signals are dominated by that of the sand's surface after the Laplace transform. In addition, the measurement noise appearing earlier than the targets' signals also affects the latter after the Laplace transform due to the exponential decay of the kernel, see Figure 17(a). Therefore, an additional important data preprocessing step is needed in order to pick up only the reflection from the targets and remove unwanted signals and noise coming earlier than the targets' signals. This step is applied to the propagated data as described below.

We first define some terms which are used in this subsection. These terms are related only to the propagated plane $P_p$. The *strongest detector* in a data set is defined as the detector at which the recorded signal has the largest amplitude. A *strong target* is either a metallic one or a nonmetallic one whose dielectric constant is larger than that of the sand. If the dielectric constant of a target is smaller than that of the sand, we call it a *weak target*. The *strongest negative (positive) peak* of a time-dependent signal at a certain detector's location is the negative (positive) peak whose amplitude is larger than the amplitudes of other negative (positive) peaks of the same signal.

We first estimate the burial depth of a target in each data set. For this purpose, we took the strongest detector. We first determined the strongest negative peak among the first four peaks, starting from the first negative peak, see Figure 16. This strongest negative peak is considered as the strongest negative peak of the sand's signal. After that, we excluded those first four peaks. The reason for considering those four peaks was due to our observation that those peaks should belong to the reflection from the sand's surface. Moreover, the first two negative (so as two positive) peaks of the incident wave were increasing in amplitude. After that, the negative (so as positive) peaks of the incident wave decreased in amplitude. Therefore any increase in amplitude of the peaks after those first four peaks should be due to the reflection from the target. By detecting the next negative (or positive) peak which was stronger than the previous negative (positive) one, we located the target's signal. Then, we determined the strongest negative peak of the target's signal. Denoting by $\Delta t$ the time delay between the latter peak and the strongest negative peak of the sand's signal, the burial depth of the target was approximated by $n(\text{sand})\Delta t$, where $n(\text{sand}) = \sqrt{\varepsilon_r(\text{sand})} = 2$ is the refractive index of the sand.

## 6.2  Extraction of target's signal: the most difficult step of data preprocessing

After estimating the burial depth, we extracted the target's signal. The extraction of signals of targets in air is quite simple. However, it is *very challenging* in the case of buried objects,
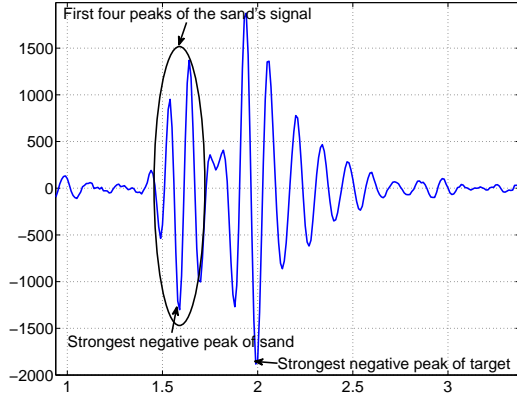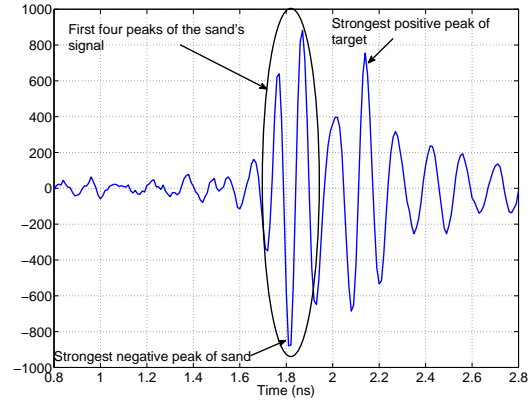
(a) A strong target            (b) A weak target

Figure 16: One-dimensional propagated signals at the strongest detectors of two targets: one strong target and one weak target. The signals consist of the reflection from the sand's surface followed by the reflections from the targets.

especially for weak targets. Indeed, when a weak target is buried at a shallow depth, its signal is merged with the reflection from the sand's surface. When it is buried at a deep depth, its signal is usually too weak to be visible in the data. Our experimental observations have shown that if a weak target is buried at a depth of more than 5 cm, then we cannot detect it. In this case, the target is missed.

As in estimating the burial depth, we also worked with the strongest detector first and excluded the first four peaks. After that, we selected the target's signal as follows: (i) Suppose that either the burial depth was larger than 5 cm, or the strongest negative peak of the target's signal was larger than that of the sand's signal in amplitude. Then we choose as the first peak of the target's signal the strongest negative peak located after the excluded ones; (ii) otherwise, the first peak of the target's signal was determined as the first positive peak which was larger than the previous positive one, provided that such a peak exists, see Figure 16. Since the reconstructed dielectric constants of targets of case (i) (respectively, case (ii)) was always larger (smaller) than that of the sand, we also categorized a target in case (i) (case (ii)) as a strong (weak) target. For all other detectors, we started from those closest to the strongest detector and on each of them assigned as the first peak of the target's signal the one which was time wise closest to that of the strongest detector. For strong targets this one should be a negative peak, while it was a positive peak for weak targets. Next, we continued similarly on all other detectors via sequentially choosing those peaks closest to the one of the previous detector. The reason for choosing a negative (positive) peak as the first peak of the target's signal for strong (weak) targets was due to our observations in numerical simulations and experimental data which have indicated that:

    a. For a strong target, the first peak of the target's signal should be negative.

    b. For a weak target, the first peak of the target's signal should be positive.

Moreover, if a strong target is buried at a depth less than 5 cm, then its signal is stronger than that of the sand in amplitude. If the burial depth is more than 5 cm, then its signal might not be stronger than that of the sand. However, since, as we mentioned above, weak targets are not visible at depths larger than 5 cm, we consider all targets buried at these depths as strong targets.

In all above cases, the data before the chosen first peak of the target's signal were set to zero. Hence, the Laplace transform of the preprocessed data is not affected by values before the first chosen peak. We note that such a choice of starting peaks artificially immerses our targets in air: because we exclude the reflection from the sand's surface. Therefore, what we reconstruct for each target by the globally convergent method is the ratio between its dielectric constant (or the *effective* dielectric constant for metals) and that of the sand, $\varepsilon_r \left(\text{target}\right) / \varepsilon_r \left(\text{sand}\right)$. Next, to obtain the value of the dielectric constant of the target, we multiply this ratio by $\varepsilon_r \left(\text{sand}\right) = 4$.

Figure 16 shows one-dimensional propagated signals at the strongest detectors of a strong target and a weak target. We indicate there the sand's signal and the peaks of the targets. These peaks were chosen as the first peaks of signals from the targets. Samples of the Laplace transform of the data before and after the extraction of the targets' signals are shown in Figure 17, which indicate the necessity of this preprocessing step.

Figure 17 (b) also shows that the preprocessed data allow us to estimate locations of the targets in $x, y$ directions as well as their $xy$-cross sections, see subsection 5.8.1. These types of information help to reduce the domain in which we look for the targets. Indeed, in Test 2 below, we took into account these types of information in choosing the first tail function.
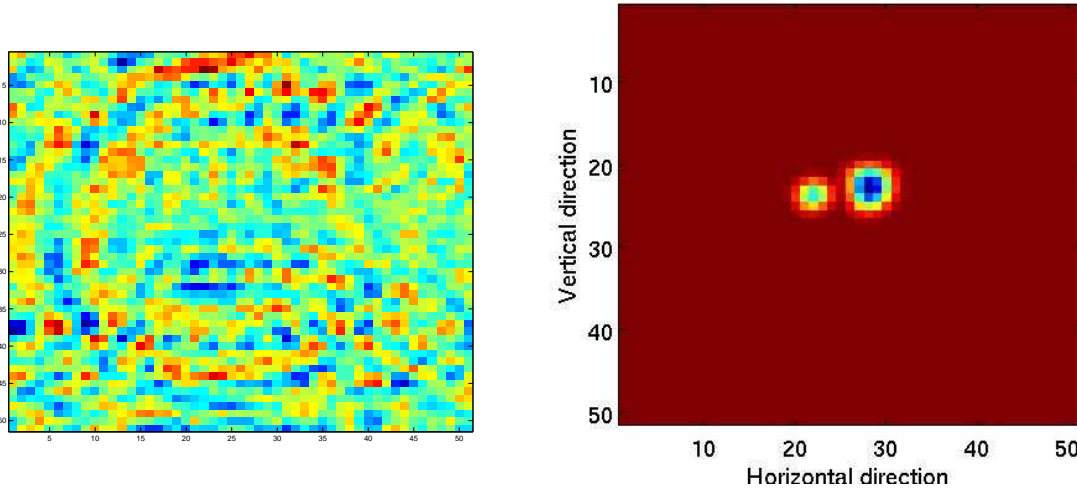


(a) Before the extraction of the targets' signals    (b) After the extraction of the targets' signals

Figure 17: The Laplace transforms of the data on the propagated plane before (a) and after (b) the extraction of the targets' signals. Without the extraction, we cannot see the targets. After the extraction, the two targets show up clearly.

## 6.3 Two tests and stopping criteria

We have analyzed the performance of the proposed algorithm with two different tests: *Test 1* and *Test 2*. In Test 1, we made use of the first tail function as described in subsection 3.6, with which the global convergence is rigorously guaranteed. In Test 2, the estimated burial depth and the $xy$-cross section of the target via the data preprocessing procedure were used to restrict the domain in which the coefficient $\varepsilon_r$ was reconstructed and to choose the first tail function. More precisely, for each target, let $x_{t,min} = \min\{x \in \Gamma_T\}$, $x_{t,max} = \max\{x \in \Gamma_T\}$, where $\Gamma_T$ is the estimated $xy$ cross section of the target, see subsection 5.8.1. The numbers $y_{t,min}$ and $y_{t,max}$ are defined similarly. Then, we define the extended $xy$ cross section by

$$\Gamma_{T,ext} = \{x_{t,min} - 0.03 < x < x_{t,max} + 0.03, \; y_{t,min} - 0.03 < y < y_{t,max} + 0.03\}.$$

Moreover, denote by $z_{t,front}$ the estimated location of the front side of the target in the $z$ direction, given by the burial depth estimation. We then define the following domain $\Omega_{T,ext}$

$$\Omega_{T,ext} := \{x = (x,y,z) \in \Omega : (x,y) \in \Gamma_{T,ext}, \; -0.2 < z < z_{t,front} + 0.02\}.$$

Clearly, $\Omega_{T,ext} \subset \Omega$. Moreover, this domain should contain the unknown target we are looking for. The last number 0.02 was for compensating for possible error in the estimated burial depth of the target. Next, we chose the first tail function $V_{1,1}$ as the function (41), where the function $w(x, \overline{s})$ was computed for the coefficient $\varepsilon_r(x) := \varepsilon_{r,0}(x)$, where

$$\varepsilon_{r,0}(x) = \varepsilon_{r,u}, \text{ for } x \in \Omega_{T,ext}, \; \varepsilon_{r,0}(x) = 1, \text{ for } x \notin \Omega_{T,ext}.$$

The upper bound $\varepsilon_{r,u}$ for the function $\varepsilon_{r,0}(x)$ was chosen as $\varepsilon_{r,u} = 25$.

Although the convergence of the resulting algorithm for Test 2 has not been rigorously proved yet, our numerical results show good reconstructions, see also [4] for accurate results when targets are in air. Note that we did not use a priori information about the targets. Instead, the information used in choosing the first tail function was derived from data pre-processing.

**Stopping criteria**:

*Stopping criterion of Test 1:* The inner iterations with respect to $i$ are stopped at $i = m_n$ such that

$$D_{n,i} \geq D_{n,i-1}, \text{ or } i < i_{max},$$

where $D_{n,i} = ||V_{n,i}|_{\Gamma_p} - V_{prop}||_{L_2(\Gamma_p)}$. Here $\Gamma_p$ is the backscattering side of $\Omega$, $V_{prop}$ is the tail function computed from the propagated data at $\Gamma_p$, and $i_{max}$ is the maximum number of inner iterations. In Test 1, we have chosen $i_{max} = 8$.

The outer iteration with respect to the pseudo frequency $s$ are stopped when the error function $D_{n,1}$ attains the first local minimum with respect to $n$.

*Stopping criterion of Test 2:* The inner iteration are stopped using the same criterion as in Test 1 but with $i_{max} = 5$. The outer iteration is stopped when the error function $D_{n,m_n}$, i.e., the error function at the final inner iteration, attains the first local minimum.

We have observed in our tests that these stopping criteria gave good results for non blind targets.

## 6.4 Results of the globally convergent method and some discussion

In Tables 6 and 7 we summarize reconstruction results of the two tests for the data sets listed in Table 5. Table 6 shows the results for the non metallic targets. For these targets, the refractive index $n(\text{target}) = \sqrt{\varepsilon_r(\text{target})}$ (as above, $\varepsilon_r(\text{target})$ was chosen by $\varepsilon_r(\text{target}) = \max_{x \in \overline{\Omega}} \varepsilon_r(x)$) is shown instead of the dielectric constant $\epsilon$ because $n(\text{target})$ was directly measured after computations were performed. Table 7 shows the burial depths and the effective dielectric constants of the metallic targets.

As described in section 6.2, the burial depth was estimated based on the time delay between the reflection by the sand's surface and the target's signal. Note that our incident signal was not really a short impulse. It is therefore natural to expect some level of error in our estimates. Since we made use of peaks of the signals in estimating the depth, the error we expect is about the distance between two consecutive peaks, which is equal to half of the wavelength (2 cm).

From Tables 6 and 7 we can see that the burial depth was accurately estimated in most cases, with the errors not exceeding 2 cm. There are two cases (#4, 7) in which the errors were about 4 cm. These targets were buried at rather deep depths of about the limiting depth (10 cm) for antipersonnel land mines. This made the estimate less accurate because of possible uncertainty in measuring the refractive index of the sand. Also, there might be an error in recording the exact burial depths during the data acquisition for deeply buried targets.

The estimates of the refractive indices of non-metallic targets with refractive indices larger than that of the sand (water and wet wood) are quite accurate with the average error of about 9.7% for Test 1 and 15.2% for Test 2. Note that the error in our direct measurement of the refractive index of the wet wood was 10%. For water, we were unable to directly measure its refractive index at the used quite high frequency of the signal, which was about 7.5 GHz. Therefore, we have made a separate experiment: we have placed that bottle of water in air, measured the backscattering data and then reconstructed the refractive index using the globally convergent method as in [3, 4]. The result of $n = 4.88$ matches well the experimentally measured refractive index of 4.84 at high frequencies in Table 3.1 of [41]. Moreover, by comparing our computed $n$ for water in Table 6 with this reference value $n = 4.88$, we can see the consistency of our results.

Targets with smaller refractive indices than that of the sand are of interest since they are models of plastic land mines and IEDs. We have observed that we can image these targets only if their burial depths do not exceed 5 cm. The average error shown in Table 6 for these weak targets is about 21.6% for Test 1 and 13% for Test 2. The average measurement error of $n$ for weak targets was about 5.4%.

In our experiments, we have missed some weak targets (not shown here), which had more than 5 cm burial depths. For these weak targets, we have observed that their signals were blended by the reflection from the sand's surface. Therefore, we could not detect any target's signal out of them. Note that, since our current algorithm uses the Laplace transform, it is

Table 5: *Description of the test data sets. Seven of them consist of two targets each (5, 6, 16, 17, 20, 23, 25). Two targets can be considered as heterogeneous (11, 12).*

| Object # | Blind/ Non-blind | Description of target | Material |
|---|---|---|---|
| 1 | Non-blind | A metallic cylinder | Metal |
| 2 | Non-blind | A metallic ball | Metal |
| 3 | Non-blind | A bottle filled with clear water | Water |
| 4 | Non-blind | A wet wooden block | Wet wood |
| 5 | Non-blind | Two metallic blocks at 6 cm separation | Metal/Metal |
| 6 | Non-blind | A metallic cylinder and a teflon bar | Metal/Teflon |
| 7 | Non-blind | A metallic block | Metal |
| 8 | Non-blind | An empty bottle | Air |
| 9 | Non-blind | A bottle filled with teflon bars | Teflon |
| 10 | Blind | A ceramic mug | Ceramic |
| 11 | Blind | A wooden doll filled with metallic screws (heterogeneous, diffuse scattering) | Wood/Metal |
| 12 | Blind | A geode (heterogeneous): two spherical layers and air inside | Rock |
| 13 | Blind | A piece of rock | Rock |
| 14 | Blind | A plastic bottle filled with coffee grounds | Coffee grounds |
| 15 | Blind | A ceramic mug | Ceramic |
| 16 | Blind | A cylinder and a block at 3 cm separation | Metal/Metal |
| 17 | Blind | An aluminum can and a block | Metal/Metal |
| 18 | Blind | A wooden doll with a metallic block inside (heterogeneous) | Wood/Metal |
| 19 | Blind | A bottle of water | Water |
| 20 | Blind | A metallic block and a rock | Metal/rock |
| 21 | Blind | A steel mug | Metal |
| 22 | Blind | A wet wooden block | Wet wood |
| 23 | Blind | A wet wooden block and an empty bottle | Wet wood/air |
| 24 | Blind | A wet wooden block | Wet wood |
| 25 | Non-blind | Two metallic blocks at 1 cm separation | Metal/Metal |

Table 6: *Result of the globally convergent algorithm: the refractive indices $n = \sqrt{\epsilon}$ and the burial depths of non-metallic targets. Object #11 is a heterogeneous target with diffuse scattering, see below. Object #12 is a heterogeneous one with outer and inner layers, the computed $n$ is compared with the average measured $n = 1.28$. Object #23 consists of two targets: wet wood and empty bottle filled with air. "Comp." stands for "Computed". The average error of strong targets is 8.5% for Test 1 and 14.7% for Test 2. The average error of weak targets is 21.6% for Test 1 and 13% for Test 2.*

| Object # | Material | Comp. depth | Exact depth | Comp. $n$, Test 1 | Comp. $n$, Test 2 | Measured $n$ |
|---|---|---|---|---|---|---|
| 3 | Water | 3.6 cm | 4.0 cm | 4.7 | 4.9 | 4.88 |
| 4 | Wet wood | 5.5 cm | 9.8 cm | 4.4 | 4.5 | 4.02 |
| 8 | Air | 2.8 cm | 3.0 cm | 1.0 | 0.98 | 1.0 |
| 9 | Teflon | 2.9 cm | 2.5 cm | 1.0 | 1.18 | 1.0 |
| 10 | Ceramic | 4.0 cm | 5.0 cm | 1.0 | 1.23 | 1.39 |
| 11 | Wood with metal screws | 4.6 cm | 4.0 cm | 1.0 | 1.46 | 1.89 (wood) N/A: diffuse scattering |
| 12 | Geode (two layers) | 3.1 cm | 2.5 cm | 1.0 | 1.52 | 1.31 (outer) 1.25 (inner) 1.28 (average) |
| 13 | Rock | 2.0 cm | 2.3 cm | 1.0 | 1.34 | 1.34 |
| 14 | Coffee grounds | 2.0 cm | 2.5 cm | 1.0 | 1.46 | 1.11 |
| 15 | Ceramic | 2.6 cm | 2.5 cm | 1.0 | 1.51 | 1.39 |
| 19 | Water | 7.5 cm | 9.5 cm | 4.5 | 5.2 | 4.88 |
| 22 | Wet wood | 2.9 cm | 3.0 cm | 4.8 | 5.3 | 4.02 |
| 23 | Wet wood | 5.7 cm | 7.5 cm | 4.0 | 4.1 | 4.02 |
|  | Empty bottle (air) | missed | 7.5 cm | missed | missed | 1.0 |
| 24 | Wet wood | 5.1 cm | 6.8 cm | 3.67 | 3.0 | 4.02 |

Table 7: *Result of the globally convergent algorithm: the estimated effective dielectric constants and the burial depths of metallic targets. Object #18 is a heterogeneous one: a wooden dool with a metallic block inside. Object #20 consists of two targets: a metallic block and a rock. Measured $n\,(rock) = 1.34$. Objects #5, 16, 17 consist of two metallic targets. Object #25 consists of two metallic targets with 1 cm distance between their surfaces: super resolution, see Figure 5.4.*

| Object # | Material | Computed depth | Exact depth | Computed $\epsilon$ Test 1 | Computed $\epsilon$ Test 2 |
|---|---|---|---|---|---|
| 1 | Metal | 2.9 cm | 4.0 cm | 29.9 | 46.4 |
| 2 | Metal | 2.9 cm | 3.0 cm | 24.5 | 31.0 |
| 5 | Metal | 3.0 cm | 3.0 cm | 23.4 | 32.4 |
|   | Metal | 3.6 cm | 3.0 cm | 30.5 | 41.2 |
| 6 | Metal | 2.8 cm | 8.5 cm | 27.8 | 37.5 |
|   | Teflon | missed | 8.5 cm |  |  |
| 7 | Metal | 9.9 cm | 14.0 cm | 47.4 | 65.8 |
| 16 | Metal | 2.5 cm | 4.5 cm | 19.9 | 24 |
|   | Metal | 3.7 cm | 4.5 cm | 33.7 | 47.5 |
| 17 | Metal | 2.0 cm | 3.8 cm | 30.0 | 51.1 |
|   | Metal | 2.7 cm | 3.8 cm | 54.8 | 93.5 |
| 18 | Wood, metal block inside | 7.1 cm | 8.5 cm | 18.3 | 19.9 |
| 20 | Metal | 6.8 cm | 8.5 cm | 30.0 | 48.1 |
|   | Rock | missed | 8.5 cm |  |  |
| 21 | Metal | 5.1 cm | 7.5 cm | 23.1 | 28.2 |
| 25 | Metal | 3.8 cm | 4.0 cm | 70.0 | 99.8 |
|   | Metal | 4.0 cm | 4.0 cm | 40.8 | 56.5 |

54

applicable only when we can detect and extract targets' signals and remove the reflection by the sand's surface as well as noise at earlier times. Otherwise, they will dominate the targets' signals after the Laplace transform, see Figure 17. Thus, these missed cases were not due to the inversion algorithm.

The signals of the metallic targets were strong compared to the sand's signal. Therefore they were quite easy to detect. We recall that metallic targets can be approximated by dielectric ones with large *appearing* dielectric constants. The estimated effective dielectric constants of our metallic test targets are between 20 and 100.

In our tests, there were four cases (#5, 16, 17, 25 in Table 7) in which there were two metallic targets simultaneously. In each case we have accurately imaged both targets.

There were also three data sets (#23 in Table 6 and #6, 20 in Table 7) in which one strong target and one weak target were buried simultaneously. In all these three cases we have accurately imaged the stronger target. However, we missed the weaker ones. The reason why we missed the weak targets was due to the fact that their burial depths were larger than 5 cm, which is our limiting depth for weak targets.

Also of interest are three cases of *heterogeneous* targets (#11, 12 in Table 6 and #18 in Table 7), since explosive devices are heterogeneous sometimes. We successfully estimated the average refractive index of the geode, which consists of two different layers, in data set #12. For the wooden doll containing a metallic block inside in data set #18 the computed dielectric constant is larger than that of the wood but smaller than other metallic targets. It is smaller because the wood covers the metal. Target #11 was a wooden doll with randomly distributed metal screws inside. In this case we observed a weak signal, rather than a strong one from the metal. In fact, we observed a well known phenomenon of *diffuse scattering*, which was described in [62]. This can be explained since the metal screws were randomly oriented and represent a conducting very rough surface to the incident microwave pulse. Multiple scattering combined with the penetration of the microwaves into the gaps between the screws strongly attenuates the incident wave and little scatters back to contribute to a measurable signal.

## 6.5   Some images

In this subsection we present samples of images of buried objects obtained via the application of our two-stage numerical procedure. The first stage is the globally convergent method and the second stage is the adaptivity. Just as above (section 5.12), this procedure accurately reconstructs all three components of targets: refractive indices, locations and shapes. The choice of parameters and calibration procedure here are the same as in subsection 5.11. Left panels of Figures 18-21 are images obtained on the first stage and right panels are images obtained on the second stage. For a better visualization, we zoom images via showing reconstruction results in the box 0.4×0.4×0.24.
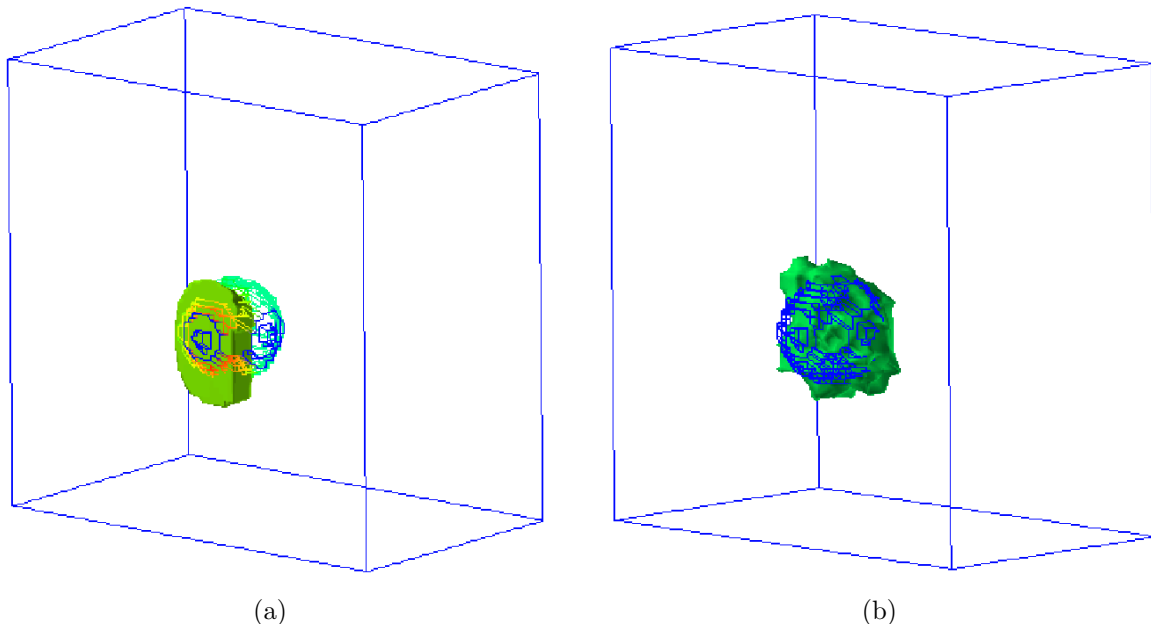
Figure 18: *Reconstruction of a metallic ball (object #2 in Table 5). a) Result of the globally convergent method (stage 1). b) Result of the adaptivity (stage 2). One can observe that the shape is reconstructed rather accurately on b).*

## 6.6 Super resolution the first experimental and numerical observations

In the data set #25, the two metallic blocks were at 1 cm distance, see Figure 21. On the other hand, the wavelength of our device is about 4 cm. Thus, the *super resolution* is achieved, which is of about $\lambda/4$, where $\lambda$ is the wavelength of our incident wave. This is an *unexpected surprise*. From a purely angular spectrum argument, the spread of backscatter angles for a fixed frequency would suggest a resolution of half a wavelength. There has been previous evidence reported that using a nonlinear inverse scattering algorithm for which strong or multiple scattering occurs, that some degree of super resolution (i.e., beyond the ideal diffraction limit of half a wavelength) can occur, see, e.g., [63]. Still, this was done in [63] only for computationally simulated data.

However, we are the *first ones* who has observed this phenomenon experimentally and, at the same time, reconstructed the image numerically.
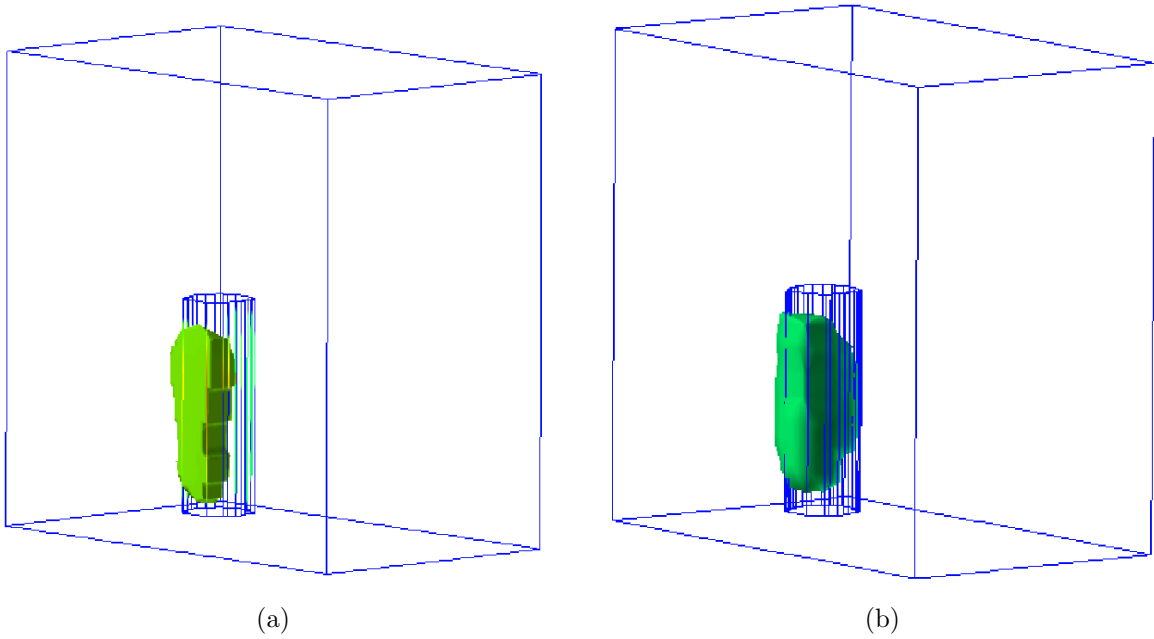
(a)                                (b)

Figure 19: *Reconstruction of a plastic bottle filled with a clean water (object #3 in Table 5). a) Result of the globally convergent method (stage 1). b) Result of the adaptivity (stage 2). Since the target was quite high (about 18 cm tall), then the incident signal was rather weak at the top and bottom of that bottle. This made it hard to reconstruct the shape more accurately. Still, one can observe a stretch in the vertical direction.*
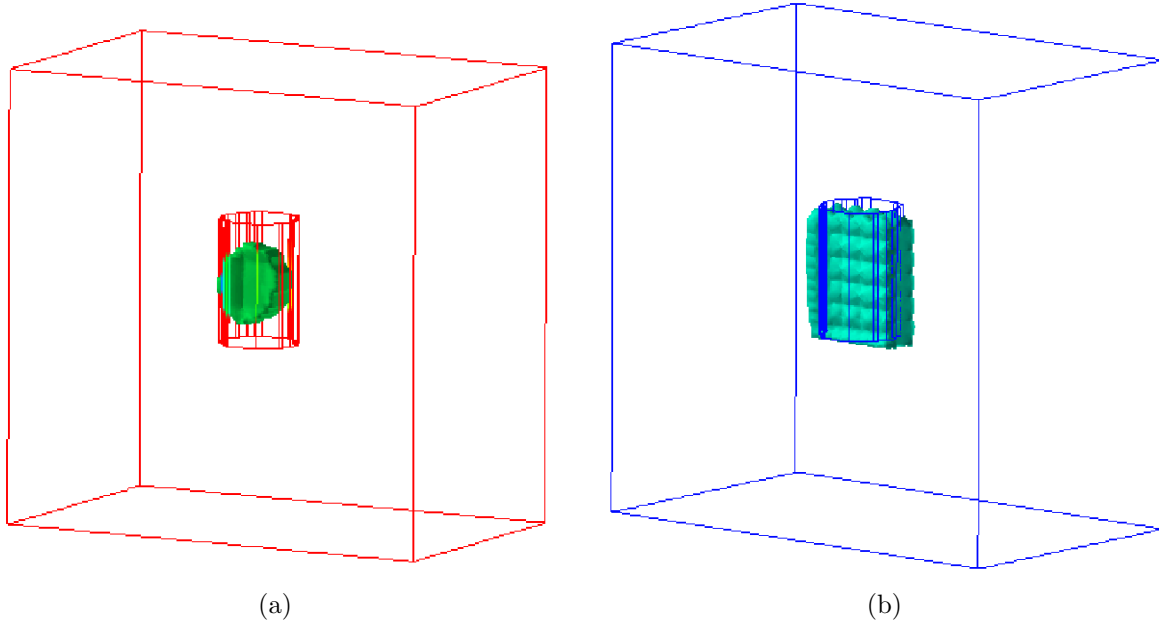
Figure 20: *Reconstruction of a ceramic mug (object #10 in Table 5). a) a) Result of the globally convergent method (stage 1). b) Result of the adaptivity (stage 2). One can observe that the shape is reconstructed rather accurately on b).*

# 7    Joint Research With Engineers of US Army Research Laboratory and Technology Transfer

Publications [17, 18, 19] are joint ones with Doctors Anders Sullivan and Lam Nguyen, engineers of RF Signal Processing and Modeling Branch of Sensors and Electron Devices Directorate of US Army Research Laboratory (ARL). We have obtained the experimental data collected in US Army Research Laboratory (ARL). The data were kindly delivered to us by Drs. Anders Sullivan and Lam Nguyen. These data were collected by the forward looking radar of ARL [59]. The goal of this radar is to detect and possibly identify shallow explosive-like targets, which look like explosives, including IEDs. Shallow targets can either lie on the ground or a few centimeters below the ground. Our goal was to image ratios $R$,

$$R = \frac{\varepsilon_r \, (\text{target})}{\varepsilon_r \, (\text{background})}, \tag{89}$$

using our globally convergent numerical method. If the dielectric constant of the background is known, then the dielectric constant of the target can be calculated from (89), as long as $R$ is known. These were *completely blind* data. In other words, we had no idea what kind of targets were in. The only thing we knew was that a target of interest was located either above the ground or buried in the ground. In addition, there were many other uncertainties in these data. A significant difficulty was that targets were hidden in a *cluttered* background.
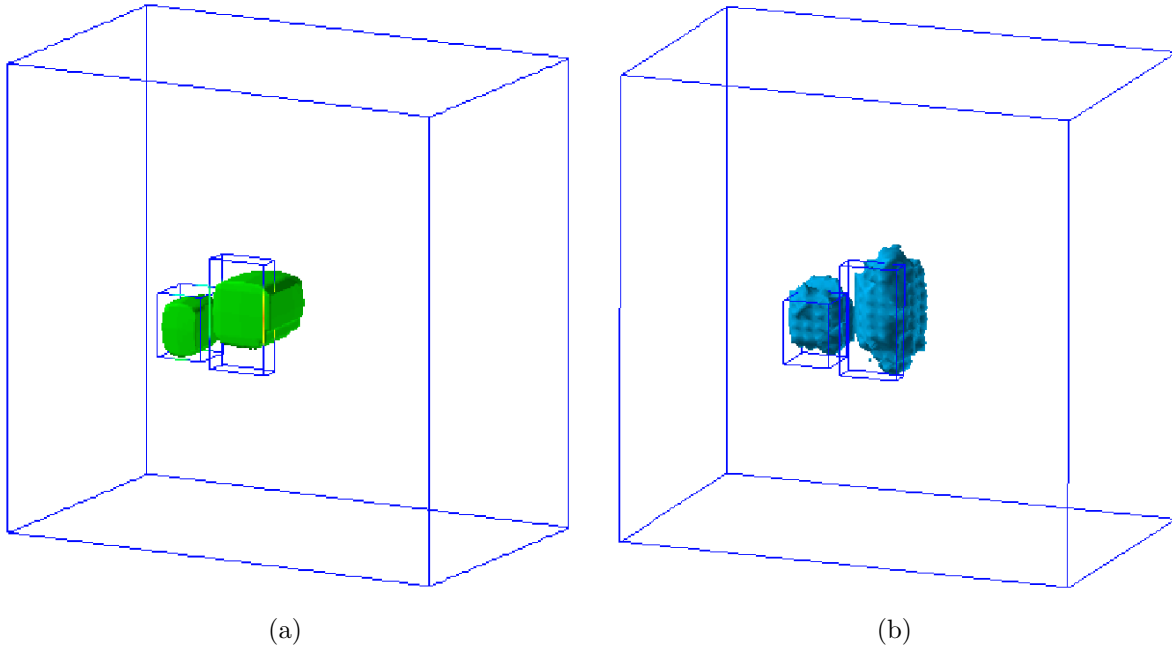
(a)                                                    (b)

Figure 21: **Super resolution**. *Reconstruction of two metallic targets (object #25 in Table 5). a) Result of the globally convergent method (stage 1). b) Result of the adaptivity (stage 2). One can observe that the shapes are reconstructed rather accurately on b). The wavelength of our signal was $\lambda = 4$ cm. On the other hand, the distance between surfaces of these two targets was 1 cm. Therefore, this is a very rare experimental and numerical observation of the super resolution phenomenon.*

In the paper [19] we have compared performances of two numerical methods on the set of experimental data or ARL:

1. The 1D version of the globally convergent method of this project.

2. The classical 1D method of the Krein equation, which is known since 1954 [51].

Detailed explanations of the Krein equation method can be found in [36, 46]. It was demonstrated in [19] that while our method computes the value of $R$ in (89) pretty accurately, the Krein equation method completely fails on the ARL data. Furthermore, the poor performance of the Krein equation method was explained analytically, see subsection 7.4.

## 7.1 Technology transfer to ARL

We have created an easy-to-use software which works with the above ARL data. Next, we have transferred this software to Drs. Sullivan and Nguyen.

## 7.2 Results of [17, 18]

To image ratios (89), we have applied the 1D version of our globally convergent numerical method of this project. Next, Drs. Sullivan and Nguyen have compared our results with those in tables [65, 66] (dielectric constants were not measured in experiments). After these comparisons, both mathematical and engineering teams were quite happy that computational results were within tabulated limits, see Table 8. This points towards both the adequacy and the robustness of our algorithm.

The recovered dielectric constant by itself is not a sufficient information to distinguish one target from another. The purpose of estimating the dielectric constant is to provide one extra piece of information about the target. Indeed, up to this point, most of the radar community relies solely on the intensity of the radar image for doing detection and discrimination of targets. It is hoped therefore that when the intensity information is coupled with the new dielectric information, algorithms could then be designed that will ultimately provide better performance in terms of probability of detection and false alarm rate. As it is clear from Table 8, some targets will have dielectric values that tend to group together, but even that is a useful information. For example, if the estimated dielectric value is consistent with a plastic land mine, then this would be another clue to uncovering the target.

Let $x \in \mathbb{R}$ be the free variable in the 1D case of this study. In our mathematical model the ratio $R$ in (89) depends on $x$, $R = R(x)$, since we treat $R(x)$ as the unknown coefficient $\varepsilon_r(x)$ in the 1D analog of equation (1). Let $R_{comp}(x)$ be function $R(x)$ computed by our globally convergent method. Then we define the target/background contrast $\overline{R}$ as

$$\overline{R} = \left\{ \begin{array}{l} \max R_{comp}(x) \ \text{if} \ R_{comp}(x) > 1, \\ \min R_{comp}(x) \ \text{if} \ R_{comp}(x) < 1. \end{array} \right.$$

Table 8: *Blindly computed by the globally convergent method dielectric constants for five available data sets of targets immersed in* cluttered *backgrounds [17, 18]. "tabulated $\varepsilon_r$ (target)" means either $\varepsilon_r$ from (89) for metallic targets, or $\varepsilon_r$ from tables [65, 66] for dielectrics, or $\varepsilon_r$ from [39] for bush. "1" in the second column means that the target was in the air, and "[3,5]" means that it was buried in the dry sand whose $\varepsilon_r$ (dry sand) $\in [3,5]$ [65].*

| target | $\overline{R}$ | $\varepsilon_r$ (background) | computed $\varepsilon_r$ (target) | tabulated $\varepsilon_r$ (target) |
|---|---|---|---|---|
| metal cylinder | 4.3 | $[3,5]$ | $[12.9, 21.4]$ | $[10, 30]$ |
| metal box | 3.8 | $[3,5]$ | $[11.4, 19]$ | $[10, 30]$ |
| wood stake | 3.8 | 1 | 3.8 | [2,6] |
| bush (clutter) | 6.4 | 1 | 6.4 | [3,20] |
| plastic cylinder | 0.28 | [3,5] | [0.84,1.4] | 1.2 |

**CONCLUSION FROM TABLE 8**:

Dielectric constants were not measured in these experiments. Therefore, the **crucial conclusion** from this table is that all computed values of dielectric constants of targets are within tabulated limits. **This was done for the most challenging case of blind experimental data for targets immersed in cluttered backgrounds.**

## 7.3 Data pre-processing

To obtain results listed in Table 8, a new data preprocessing procedure was applied in [18, 17]. This was necessary, because the experimental data look very much different from simulated ones, just as in sections 5,6. So that the pre-processed data would look somewhat similar with computationally simulated data. The pre-processed data were used as input for the globally convergent algorithm.

The data processing consisted of the following two stages:

*Stage 1.* Selection of a single peak out of the entire experimental curve by the following rule: this should be the earliest peak of the largest amplitude

$$\text{out of } \begin{cases} \text{all peaks for a target buried in the ground,} \\ \text{all downwards looking peaks for a target above the ground.} \end{cases}$$

*Stage 2.* The choice of the calibration factor $CF$. This was necessary because the amplitudes of the experimental data were of the order of $10^4$ whereas amplitudes of computationally simulated data were less than 1. We have chosen $CF$ in such a way that the Laplace transform of the simulated data was rather close to the Laplace transform of the those selected peaks of experimental data, when those peaks were multiplied by $CF$. Thus, we got $CF = 10^{-7}$ and our pre-processed data were

$$\text{pre-processed data} = 10^{-7} \cdot (\text{data pre-processed on the first stage}). \qquad (90)$$

**Remark**. The contrast $\overline{R}$ of a target heavily depends on the calibration factor $CF$. Therefore, it is *very important* to have a *single* calibration factor for *all* targets. Otherwise,

Stage 2 would be biased. We point out that we did not know $\overline{R}$ in advance because of the blind study case.
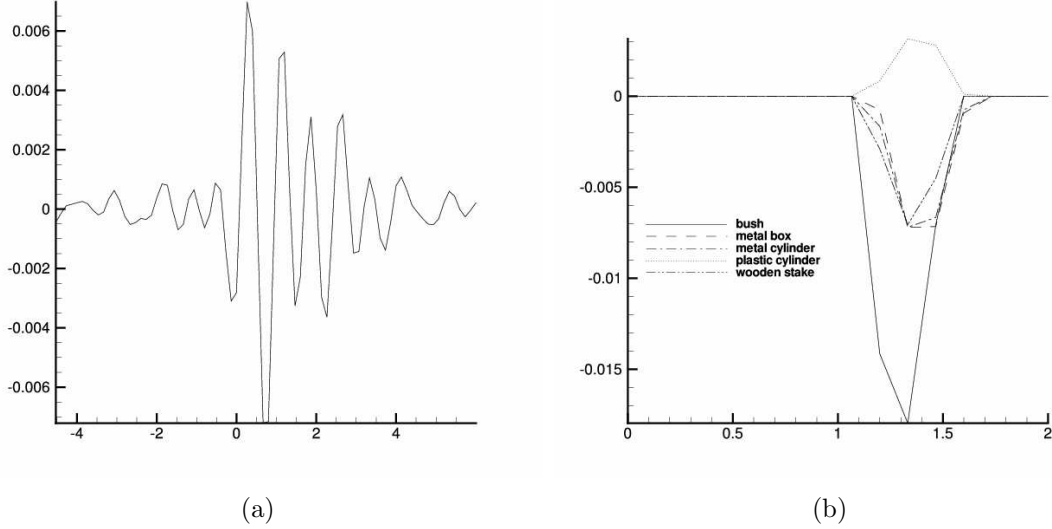
Figure 22 shows original and pre-processed data.



(a)  (b)

Figure 22: *Original and pre-processed Army Research Laboratory data. a) A sample of the original time resolved data data. b) Pre-processed data for all five available targets (superimposed). The data pre-processing was done as described in Stages 1 and 2.*

## 7.4   Comparison with the classical Krein equation method [19]

The classical Krein integral equation is

$$2f(+0)p(z,t) + \int\limits_{-z}^{z} f'(t-\lambda)p(z,\lambda)d\lambda = -1. \tag{91}$$

Here $z$ is a free variable, which is connected with the original variable $x$ via $z = z(x)$, where $z(x)$ is a one-to-one function. Next, $f(t)$ is the data function which is extended as an odd function from $\{t > 0\}$ into $\{t < 0\}$. The function $p(z,t)$ depends on $z$ as on a parameter. So that equation (91) is solved for each $z > 0$. As soon as the function $p(z,t)$ is found, the unknown coefficient $R(x)$ can be easily reconstructed.

We took the preprocessed data of the above Stage 1 and have tried to find a calibration factor $CFK$ for them, in such a way that, similarly with (90), we would have for *all five targets*

pre-processed data $= f(t) = CFK \cdot (\text{data pre-processed on the first stage})$, (92)

see Remark in subsection 7.3. To find the number $CFK$, we have selected any of above five targets. We call it *calibration target*. Then have found a "temporary" $CFK(\text{target})$ in such

62

Table 9: *Computed values of $\overline{R}_K$ for Case 1. Wood stake is the calibration target.* **Bold faced** *are values of $\overline{R}_K$ which lead to values of $\varepsilon_r\,(target)$ outside of tabulated intervals.*

| target | $\overline{R}_K$ | $\varepsilon_r\,(bckgr)$ | computed $\varepsilon_r\,(target)$ | tabulated $\varepsilon_r\,(target)$ |
|---|---|---|---|---|
| metal cylinder | 3.25 | [3,5] | [9.75,16.25] | [10,30] |
| metal box | 3.97 | [3,5] | [11.91,19.85] | [10,30] |
| bush | **42.5** | 1 | 42.5 | [3,20] |
| plastic cylinder | **0.6** | [3,5] | [1.8,3] | 1.2 |

Table 10: *Computed values of $\overline{R}_K$ for Case 2. Plastic cylinder is the calibration target.* **Bold faced** *are values of $\overline{R}_K$ which lead to values of $\varepsilon_r\,(target)$ outside of tabulated intervals.*

| target | $\overline{R}_K$ | $\varepsilon_r\,(bckgr)$ | computed $\varepsilon_r\,(target)$ | tabulated $\varepsilon_r\,(target)$ |
|---|---|---|---|---|
| metal cylinder | 9.8 | [3,5] | [29.4,49] | [10,30] |
| metal box | 13.9 | [3,5] | [41.7,69.5] | [10,30] |
| wood stake | **17** | 1 | 17 | [2,6] |
| bush | **>>100** | 1 | >>100 | [3,20] |

a way that the value of $\overline{R} := \overline{R}_K$ for this target computed via equation (91) would be the same as the one listed in Table 9. Next, we have multiplied the data for four other targets by the same number $CFK(\text{target})$ and have solved Krein equation (91) for so pre-processed data. Next, we have done the same for another target and repeated this five times.

We have found that it is impossible to choose a proper number $CFK(\text{target})$ in such a way that resulting values of $\overline{R}_K$ would be within tabulated limits for *all five targets*. More precisely, for each out of five possible $CFK(\text{target})$ there existed at least one target for which the value of $\overline{R}_K$ was outside the tabulated limit. Below are three cases illustrating this conclusion. In the case when metal box was chosen as the calibration target, our calculations led to the same results as those in Table 6. This is because $\overline{R}(\text{wood stake}) = \overline{R}(\text{metal box}) = 3.8$. Also, $\overline{R}(\text{metal cylinder}) = 4.3 \approx 3.8 = \overline{R}(\text{metal box})$. Hence, the calculation for the case when the metal cylinder was chosen as the calibration target again led to results, which are similar with those of Table 9.

**Case 1.** Wood stake is the calibration target. We have obtained $CFK\,(\text{wood stake}) = 10^{-5}$.

**Case 2**. Plastic cylinder is the calibration target. We have obtained $CFK(\text{plastic cylinder}) = 1.8 \cdot 10^{-5}$.

**Case 3.** Bush is the calibration target. We have obtained $CFK(\text{bush}) = 0.6 \cdot 10^{-5}$.

To see how the changes in the calibration factor affect the reconstructed values of $\overline{R}$ and $\overline{R}_K$, we present Figure 23. The visual analysis of these curves shows that the increase of the calibration factor affects $\overline{R}$ linearly, and it affects $\overline{R}_K$ exponentially. This explains results of above Cases 1-3.

We now explain Figure 23 as well as results of tables 9,10,11. To do this, we use (92) to

Table 11: *Computed values of* $\overline{R}_K$ *for Case 3. Bush is the calibration target.* **Bold faced** *are values of* $\overline{R}_K$ *which lead to values of* $\varepsilon_r$ *(target) outside of tabulated intervals.*

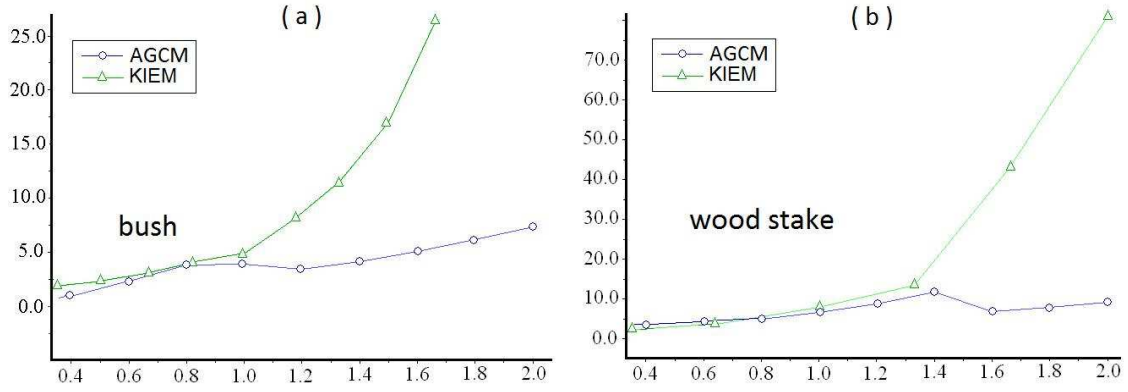| target | $\overline{R}_K$ | $\varepsilon_r$ (bckgr) | computed $\varepsilon_r$ (target) | tabulated $\varepsilon_r$ (target) |
|---|---|---|---|---|
| metal cylinder | 2.0 | [3,5] | [6,10] | [10,30] |
| metal box | **1.16** | [3,5] | [3.48,5.8] | [10,30] |
| wood stake | 3.2 | 1 | 3.2 | [2,6] |
| plastic cylinder | **0.74** | [3,5] | [3.22,3.7] | 1.2 |



Figure 23: *Dependencies of* $\overline{R}$ *and* $\overline{R}_K$ *from the calibration factor for bush and wood stake are displayed. In both a),b) "1" on the* $y-axis$ *for AGCM (the globally convergent method) corresponds to* $CF = 10^{-7}$ *in (90). a) "1" on the* $y-axis$ *in KIEM (Krein method) corresponds to* $CFK(bush) = 0.6 \cdot 10^{-5}$ *(Case 3). b) "1" on the* $y-axis$ *in KIEM (Krein method) corresponds to* $CFK(wood\ stake) = 10^{-5}$ *(Case 1).*

present the Krein equation (91) as

$$p(z,t) - \frac{CFK}{2} \int_{-z}^{z} \overline{f}'(t-\tau)p(z,\tau)d\tau = \frac{1}{2}, \quad t \in [-z, z], \quad \forall z \in [0, T/2]. \tag{93}$$

In (93) $\overline{f}(t)$ is the pre-preprocessed data as in Stage 1 and $f(+0) = 1$ as on Figure 23. Denote $\beta := z \cdot CFK \sup_{|t|<z} \left| \overline{f}'(t) \right|$. If $\beta \in (0,1)$, then one can solve integral equation (93) via the classical resolvent series. It is clear from this series that the solution $p(z,t)$ changes almost with an exponential speed when the calibration factor $CFK$ changes.

On the other hand, taking into account the calibration factor $CF$ for the globally convergent method, the function $q(x,s)$ in (18) can be represented as

$$q(x,s) = \frac{\partial}{\partial s} \left[ \frac{\ln(CF \cdot w(x,s))}{s^2} \right] = \frac{2}{s^2} \left[ -\frac{\ln(CF \cdot w(x,s))}{s} + \frac{w_s(x,s)}{w_s(x,s)} \right].$$

Since we work with large values of $s > 1$, then $q(x,s)$ changes logarithmically with the change of $CF$. This is a much slower rate of change than the exponential one of the Krein equation.

# 8 Global Convergence via a Carleman Weight Function

The statement of the CIP3.1 in section 3.1 uses only the Dirichlet boundary condition (19). However, using the procedure, which is a simple generalization of the data complementing in (76), it is possible to prove that one can approximately find both Dirichlet and Neumann boundary conditions for the function $q(x,s)$ on the entire boundary $\partial\Omega$. Thus, by (18), we should solve the following problem for the function $q(x,s)$

$$\Delta q - 2s^2 \nabla q \int_{s}^{\infty} \nabla q(x,\tau)\,d\tau + 2s \left| \int_{s}^{\infty} \nabla q(x,\tau)\,d\tau \right|^2 = 0, x \in \Omega, s \geq \underline{s}, \tag{94}$$

$$q\mid_{\partial\Omega} = \psi(x,s), \partial_\nu q\mid_{\partial\Omega} = \varphi(x,s), s \geq \underline{s}. \tag{95}$$

Since the first work of Beilina and Klibanov [25] on the topic of global convergence, the approach to the problem (94), (95), which has been pursued so far and which is the focus of the effort of this project, by the PI is based on the truncation of the integral in (94) at a high value of the pseudo frequency $s := \overline{s}$. In other words, it has been assumed so far that

$$\int_{s}^{\infty} q(x,\tau)\,d\tau = \int_{s}^{\overline{s}} q(x,\tau)\,d\tau + V(x,\overline{s}), s \in (\underline{s}, \overline{s}).$$

Next, the function $V(x, \overline{s})$, which is called "the tail function", and the function $q(x, s)$ were approximated separately in an iterative procedure. In particular, the first approximation $V_{1,1}(x)$ for the function $V(x, \overline{s})$ was found via truncation of an asymptotic series with respect to $1/\overline{s}, \overline{s} >> 1$ and solution of the resulting Dirichlet boundary value problem (39), (40) for the Laplace equation.

Unlike the above, it was figured out in the recent work [11] how to work out a globally convergent numerical method without any truncation of the integrals in (94). Instead, a significantly new idea is used, Namely, a weighted cost functional is constructed in [11]. The weight is the Carleman Weight Function (CWF), which is involved in the Carleman estimate for the Laplace operator. Let $H$ be a certain Hilbert space. Given a bounded set $G \subset H$ of an arbitrary size, one can choose a parameter of CWF in such a way that that functional becomes strictly convex on $G$. The strict convexity, in turn guarantees the global convergence of the gradient descent method, i.e. this method can start from any point of $G$ and still will converge to the exact solution.

Thus, the work [11] represents a new globally convergent numerical method for CIP3.1. Another new approach to the issue of the global convergence via another CWF was recently proposed in [12].

Globally strictly convex cost functionals with Carleman Weight Functions in them were constructed by the PI in his previous publications of 1997 [49, 50]. However, those functionals were constructed in the time domain for CIPs for hyperbolic [49] and parabolic [50] PDEs. Equation (94), which is in the Laplace transform domain, was not considered in these references and the problem of tails was not addressed.

## 8.1 Outline of the new globally convergent numerical method of [11]

We represent the function $q(x, s)$ as a series with respect to an orthonormal basis of $L_2(\underline{s}, \infty)$. Using this representation, the integral over the infinite interval $(s, \infty)$ in (94) can be easily computed. Let $\{f_n(s)\}_{n=0}^{\infty} \subset L_2(\underline{s}(d), \infty)$ be an orthonormal basis in $L_2(\underline{s}(d), \infty)$ such that $\{f_n(s)\}_{n=0}^{\infty} \subset L_1(\underline{s}(d), \infty)$. As an example, one can consider Laguerre functions [24]

$$L_n(s) = e^{-s/2} \sum_{k=0}^{n} (-1)^k C_n^k \frac{s^k}{k!}, \ s \in (0, \infty), \ C_n^k = \frac{n!}{(n-k)!k!}.$$

Next, we set $f_n(s) := L_n(s - \underline{s}(d)), s \in (\underline{s}(d), \infty)$. It can be verified that $q(x, s) \in L_2(\underline{s}(d), \infty), \forall x \in \overline{\Omega}$. Hence, one can represent the function $q(x, s)$ as

$$q(x, s) = \sum_{n=0}^{\infty} q_n(x) f_n(s) \approx \sum_{n=0}^{N-1} q_n(x) f_n(s), \ s \geq \underline{s}(d), \tag{96}$$

where $N$ is a sufficiently large integer which should be chosen in numerical experiments. Consider the vector of coefficients in the truncated series (96) $Q(x) = (q_0, ..., q_{N-1})(x) \in \mathbb{R}^N$.

Substituting the truncated series (96) in (94), we obtain

$$
\sum_{n=0}^{N-1} \Delta q_n(x) f_n(s) - 2s^2 \sum_{m=0}^{N-1} \sum_{n=0}^{N-1} \nabla q_m(x) \nabla q_n(x) f_m(s) \int_s^\infty f_n(\tau) d\tau
$$

$$
+ 2s \sum_{m=0}^{N-1} \sum_{n=0}^{N-1} \nabla q_m(x) \nabla q_n(x) \int_s^\infty f_m(\tau) d\tau \int_s^\infty f_n(\tau) d\tau = 0. \tag{97}
$$

To be precise, one should have "$\approx$" instead of "$=$" in (97) due to the truncation (13). Multiplying both sides of (97) by $f_k(s)$, integrating over $(\underline{s}(d), \infty)$ and keeping in mind the fact that $\{f_n(s)\}_{n=0}^\infty$ is an orthonormal basis in $L_2(\underline{s}, \infty)$, we obtain the following system of coupled nonlinear elliptic equations:

$$
\Delta q_k(x) + \sum_{m=0}^{N-1} \sum_{n=0}^{N-1} F_{kmn} \nabla q_m(x) \nabla q_n(x) = 0, \ k = 0, \dots, N-1, \ x \in \Omega, \tag{98}
$$

where the numbers $F_{kmn}, \ k, m, n \in \{0, \dots, N-1\}$, are given by

$$
F_{kmn} = \int_{\underline{s}(d)}^\infty 2s f_k(s) \Big( \int_s^\infty f_m(\tau) d\tau \int_s^\infty f_n(\tau) d\tau \Big) ds - \int_{\underline{s}(d)}^\infty 2s^2 f_k(s) f_m(s) \Big( \int_s^\infty f_n(\tau) d\tau \Big) ds.
$$

The boundary conditions for $q_n$ are obtained by substituting again the truncated series (96) into (95). For the convenience of the following analysis, we rewrite system (98) together with the boundary conditions as the following boundary value problem with over-determined boundary conditions. Note that we have both Dirichlet and Neumann boundary conditions

$$
\Delta Q + F(\nabla Q) = 0, \tag{99}
$$

$$
Q \mid_{\partial\Omega} = \Phi(x), \partial_n Q \mid_{\partial\Omega} = \Psi(x), \tag{100}
$$

where the boundary vector functions $\Phi(x), \Psi(x) \in \mathbb{R}^N$ are computed from the functions $\varphi(x, s), \psi(x, s)$ and $F : \mathbb{R}^{3N} \to \mathbb{R}^N$, $F = (F_0, \dots, F_{N-1}) \in C^\infty(\mathbb{R}^{3N})$ with

$$
F_k(\nabla Q) = \sum_{m=0}^{N-1} \sum_{n=0}^{N-1} F_{kmn} \nabla q_m(x) \nabla q_n(x), \ k = 0, \dots, N-1.
$$

If we can find an approximate solution of the problem (99)–(100), then we can find an approximation for the function $q$ via the truncated series (96). Therefore, we focus below on the method of approximating the vector function $Q(x)$.

Let $\widetilde{F}(x) = (\widetilde{F}_0, \dots, \widetilde{F}_{N-1})(x), x \in \Omega$, be a vector function and $H$ be a Hilbert space. Below any statement that $\widetilde{F} \in H$ means that every component of the vector $\widetilde{F}$ belongs to $H$. The norm $\left\| \widetilde{F} \right\|_H$ means

$$
\left\| \widetilde{F} \right\|_H = \Big( \sum_{n=0}^{N-1} \left\| \widetilde{F}_n \right\|_H^2 \Big)^{1/2}.
$$

Our ultimate goal is to apply this method to the inversion of above experimental data of [2, 3, 4, 5]. Thus, just as in these references, below $\Omega$ is chosen to be a rectangular parallelepiped. Without loss of generality, it is convenient to assume that

$$\Omega = \{x = (x_1, x_2, x_3) : (x_1, x_2) \in (-A, A), x_3 \in (0, 1/2)\},$$

where $A > 0$ is a number. Thus, $\partial\Omega = \Gamma_1 \cup \Gamma_2 \cup \Gamma_3$, where

$$\Gamma_1 = \{x \in \partial\Omega | x_3 = 0\}, \quad \Gamma_2 = \{x \in \partial\Omega | x_3 = 1/2\}, \quad \Gamma_3 = \Omega \setminus (\Gamma_1 \cup \Gamma_2).$$

As in [2, 3, 4, 5], $\Gamma_1$ is considered as the backscattering side, where the data are measured. Although measurements were not performed on $\Gamma_2 \cup \Gamma_3$, it was demonstrated in these references that assigning

$$w(x, s) \mid_{\Gamma_2 \cup \Gamma_3} := w_0(x, s) \mid_{\Gamma_2 \cup \Gamma_3} \tag{101}$$

does not affect the accuracy of the reconstruction via the technique of [1]. Thus, we now relax conditions (100), assuming that the normal derivative is given only on $\Gamma_1$, the Dirichlet condition is given on $\Gamma_1 \cup \Gamma_3$ and no boundary condition is given on $\Gamma_2$,

$$Q \mid_{\Gamma_1 \cup \Gamma_3} = \Phi(x), \, \partial_n Q \mid_{\Gamma_1} = \Psi(x). \tag{102}$$

Let us introduce a CWF for the Laplace operator which is suitable for this domain $\Omega$ and for boundary conditions (102). Let $a, \xi \in (0, 1/2)$ be two arbitrary numbers. Let $\lambda, \nu > 1$ be two large parameters which we will choose later. Then the CWF has the form

$$\varphi_{\lambda,\nu}(x_3) = e^{\lambda(x_3+\xi)^{-\nu}} e^{-\lambda(a+\xi)^{-\nu}}. \tag{103}$$

Hence,

$$\lim_{\lambda \to \infty} \varphi_{\lambda,\nu}(1/2) = 0.$$

Lemma 9.1 establishes a Carleman estimate for the operator $\Delta$ in the domain $\Omega$ with the weight function (103).

**Lemma 9.1**. *There exist sufficiently large numbers $\lambda_0 = \lambda_0(\Omega) > 1, \nu_0 = \nu_0(\Omega, a, \xi) > 1$ depending only on the listed parameters such that for an arbitrary function $u \in H^2(\Omega)$ satisfying $u \mid_{\Gamma_3} = 0$ the following Carleman estimate holds for all $\lambda \geq \lambda_0$ and with a constant $C = C(\Omega) > 0$ depending only on the domain $\Omega$*

$$\int_\Omega (\Delta u)^2 \varphi^2_{\lambda,\nu_0} dx + C \left( \|u \mid_{\Gamma_1}\|^2_{H^1(\Gamma_1)} + \|\partial_n u \mid_{\Gamma_1}\|^2_{L_2(\Gamma_1)} \right) e^{2\lambda\xi^{-\nu_0}}$$

$$\geq C \int_\Omega \left( \lambda |\nabla u|^2 + \lambda^3 u^2 \right) \varphi^2_{\lambda,\nu_0} dx - C\varphi^2_{\lambda,\nu_0}(1/2) \int_{\Gamma_2} \left( |\nabla u|^2 + u^2 \right) dx_2 dx_3.$$

Below $C = C(\Omega) > 0$ denotes different constants depending only on the domain $\Omega$. Let $R > 0$ be an arbitrary number. Define the set $G$ of vector functions $Q$ as

$$G = G(R, \Phi, \Psi) = \left\{ \begin{array}{l} Q = (q_0, ..., q_{N-1})^T \in H^3(\Omega) : \|Q\|_{H^3(\Omega)} < R, \\ Q \mid_{\Gamma_1 \cup \Gamma_3} = \Phi(x), \, \partial_n Q \mid_{\Gamma_1} = \Psi(x). \end{array} \right.$$

Then $G$ is an open set in $H^3(\Omega)$. Also, Embedding Theorem implies that

$$G \subset C^1(\overline{\Omega}), \|Q\|_{C^1(\overline{\Omega})} < CR, \forall Q \in G.$$

Let $\nu_0 = (\Omega, a, \xi) > 1$ be the number in Lemma 9.1. Denote $\Omega_a = \Omega \cap \{x_3 < a\}$. We seek the solution $Q$ of the problem (99), (102) on the set $G$ via minimizing the following Tikhonov-like cost functional with the CWF $\varphi_{\lambda,\nu_0}^2$ and with the regularization parameter $\alpha \in (0,1)$

$$J_{\lambda,\alpha}(Q) = \frac{1}{2} \int_{\Omega} [\Delta Q + F(\nabla Q)]^2 \varphi_{\lambda,\nu_0}^2 dx + \frac{\alpha}{2} \|Q\|_{H^3(\Omega)}^2, Q \in G(R, \Phi, \Psi).$$

**Theorem 9.2**. *There exists a sufficiently large number $\lambda_1 = \lambda_1(\Omega, G, F) > 1$ depending only on $\Omega, G, F$ such that if $\lambda \geq \lambda_1$ and $\alpha \in [\varphi_{\lambda,\nu_0}^2(1/2), 1)$, then the functional $J_{\lambda,\alpha}(Q)$ is strictly convex on the set $G$, i.e., there exists a constant $C_1 = C_1(\Omega, G, F) > 0$ depending only on $\Omega, G, F$ such that for all $Q_1, Q_2 \in G$*

$$J_{\lambda,\alpha}(Q_2) - J_{\lambda,\alpha}(Q_1) - J'_{\lambda,\alpha}(Q_1)(Q_2 - Q_1)$$
$$\geq C_1 \|Q_2 - Q_1\|_{H^1(\Omega_a)}^2 + \frac{\alpha}{2} \|Q_2 - Q_1\|_{H^3(\Omega)}^2,$$

*where $J'_{\lambda,\alpha}(Q_1)$ is the Fréchet derivative of the functional $J_{\lambda,\alpha}$ at the point $Q_1$.*

## 8.2 Global convergence of the gradient descent method

It is well-known that the gradient descent method is globally convergent for functionals which are strictly convex on the entire space. However, the functional $J_{\lambda,\alpha}$ is strictly convex only on the bounded set $G(R, \Phi, \Psi)$. Therefore, we need to prove the global convergence of this method on this set. Suppose that a minimizer $Q_{\min}$ of $J_{\lambda,\alpha}$ exists on $G(R, \Phi, \Psi)$. In the regularization theory $Q_{\min}$ is called *regularized solution* of the problem (99), (102) [1]. Theorem 9.2 guarantees that such a minimizer is unique. First, we estimate in this section the distance between regularized and exact solutions, depending on the level of error in the data. Next, we establish that Theorem 9.2 implies that the gradient descent method of the minimization of the functional $J_{\lambda,\alpha}$ converges to $Q_{\min}$ if starting at any point of the set $G(R/4, \Phi, \Psi)$, i.e., it converges globally. In addition, we estimate the distance between points of the minimizing sequence of the gradient descent method and the exact solution of the problem. In principle, global convergence of other gradient methods for the functional $J_{\lambda,\alpha}$ can also be proved. However, we are not doing this for brevity.

Following one of concepts of Tikhonov for ill-posed problems (see, e.g., section 1.4 in [1]), we assume that there exist noiseless boundary data $\Phi^*(x)$ and $\Psi^*(x)$ which correspond to the exact solution $Q^*$ of the problem (99), (102). Also, we assume that functions $\Phi(x)$ and $\Psi(x)$ at the part $\Gamma_1$ of the boundary contain an error of the level $\delta$,

$$\|\Phi - \Phi^*\|_{H^1(\Gamma_1)} \leq \delta, \|\Psi - \Psi^*\|_{L_2(\Gamma_1)} \leq \delta. \tag{104}$$

69

On the other hand, we do not assume any error in the function $\Phi$ at $\Gamma_2 \cup \Gamma_3$, see a heuristic condition (101), which was justified numerically in [2, 3, 4, 5]. Theorem 9.3 estimates the distance between $Q_{\min}$ and $Q^*$ in the norm of $H^1(\Omega_a)$, which might be sufficient for computations. Note that while in Theorem 9.2 we have compared functions $Q_1$ and $Q_2$ satisfying the same boundary conditions, functions $Q_{\min}$ and $Q^*$ in Theorem 9.3 satisfy different boundary conditions, because of the error in the data.

**Theorem 9.3**. *Assume that conditions of Theorem 9.2 hold and $\lambda \geq \lambda_1$. In addition, assume that conditions (104) are satisfied and also $\Phi \mid_{\Gamma_3} = \Phi^* \mid_{\Gamma_3}$. Suppose that there exists an exact solution $Q^*$ of the problem (99), (102) and $Q^* \in G(R, \Phi^*, \Psi^*)$. In addition, assume that there exists a minimizer $Q_{\min} \in G(R, \Phi, \Psi)$ of the functional $J_{\lambda,\alpha}$. Let the number $\delta_0 = \delta_0(\Omega, G, F, a, \xi) \in (0, 1)$ be so small that*

$$\delta_0^{-\xi^{-\nu_0}/2} > \lambda_1.$$

*Let $\delta \in (0, \delta_0)$. Choose the regularization parameter $\alpha$ as $\alpha = \alpha(\delta) = \delta^{2\gamma}$, where*

$$2\gamma = \frac{\xi^{\nu_0}}{2(a+\xi)^{\nu_0}} \left[ 1 - \frac{\xi^{\nu_0}}{(a+\xi)^{\nu_0}} \right] \in \left( 0, \frac{1}{2} \right).$$

*Then $\alpha \in \left( \varphi_{\lambda,\nu_0}^2(1/2), 1 \right)$ (as in Theorem 9.2) and*

$$\|Q^* - Q_{\min}\|_{H^1(\Omega_a)} \leq C_1 \delta^\gamma, \ \forall \delta \in (0, \delta_0).$$

We now formulate the gradient descent method with the constant step size $\beta$ for the problem of the minimization of the functional $J_{\lambda,\alpha}$. For brevity we do not indicate the dependence of functions $Q_n$ on parameters $\lambda, \alpha, \beta$. Let $Q_1 \in G(R/4, \Phi, \Psi)$ be an arbitrary point of the set $G(R/4, \Phi, \Psi)$. Consider the sequence $\{Q_n\}_{n=1}^{\infty}$ of the gradient descent method,

$$Q_{n+1} = Q_n - \beta J_{\lambda,\alpha}'(Q_n), n = 1, 2, ... \tag{105}$$

Theorem 9.4 establishes the global convergence of the sequence (105) on the set $G(R, \Phi, \Psi)$. In addition, it estimates the distances between points of this sequence and the exact solution, depending on the level $\delta$ of the noise in the data in (104).

**Theorem 9.4**. *Choose parameters $\lambda_1, \nu_0, \alpha$ as in Theorem 9.2 and let $\lambda \geq \lambda_1$. Assume that the functional $J_{\lambda,\alpha}$ achieves its minimal value on the set $G(R, \Phi, \Psi)$ at a point $Q_{\min} \in G(R/4, \Phi, \Psi)$. Consider the sequence (105), in which the starting point $Q_1$ is an arbitrary point of the set $G(R/4, \Phi, \Psi)$. Then there exists a sufficiently small number $\beta = \beta(\lambda, \alpha, G(R, \Phi, \Psi)) \in (0, 1)$ and a number $\theta = \theta(\beta) \in (0, 1)$, both dependent only on the listed parameters, such that the sequence (105) converges to the point $Q_{\min}$,*

$$\|Q_{n+1} - Q_{\min}\|_{H^3(\Omega)} \leq \theta^n \|Q_1 - Q_{\min}\|_{H^3(\Omega)}, n = 1, 2, ...$$

*In addition, assume that there exists an exact solution $Q^* \in G(R/5, \Phi^*, \Psi^*)$ of the problem (14), (45) and that all conditions of Theorem 9.3 hold. Then for all $\delta \in (0, \delta_0)$ the following estimate holds*

$$\|Q_{n+1} - Q^*\|_{H^1(\Omega_a)} \leq \theta^n \|Q_1 - Q_{\min}\|_{H^3(\Omega)} + C_1 \delta^\gamma, n = 1, 2, ..$$

70

## 8.3  Numerical examples

In this subsection we present a limited testing of the above algorithm for some numerically simulated data. We also compare its performance with the above locally convergent method alone using the coefficient of the homogeneous medium as the first guess. Numerical results for experimental data in both 1-d and 3-d cases are under consideration and will be reported in future work.
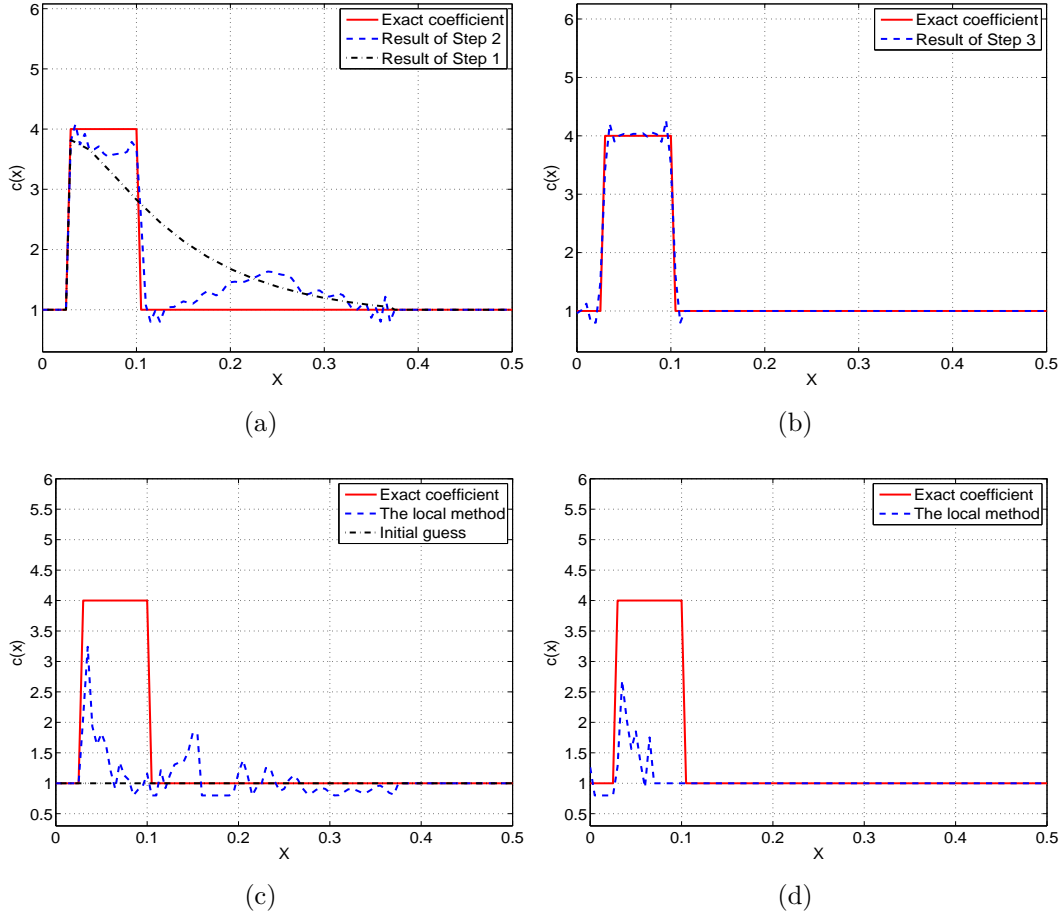


Figure 24: Reconstruction of the coefficient of Example 1. (a) Result of Steps 1 and 2, (b) Result of Step 3, (c) Result of Step 2 starting from the homogeneous medium as the first guess, (d) Result of Step 3 applied to the result of (c).

Since our target application is in imaging of an abnormal object placed in a homogeneous medium, we mainly test the proposed algorithm with a discontinuous coefficient. The locations of the discontinuities represent the location of the target. It is hard to obtain accurate reconstructions at locations far away from the measurement point. However, this is not a serious restriction from the practical standpoint. Indeed, our experience of working with 3-d time resolved backscattering experimental data [2, 3, 4, 5] tells us that, using the

so-called data propagation procedure in data pre-processing, we can approximate quite well both the distance from the measurement point to the target and the Dirichlet and Neumann backscattering data near the target. Thus, we assume below that the target is close to the measurement point.

In the following examples, the parameters were chosen as follows: The pseudo frequencies were $s \in [4, 15]$ with the integration step size in (97) $\Delta s = 0.05$. The number of Laguerre's functions was $N = 11$. The coefficients $\lambda$ in the CWF was $\lambda = 3$. The regularization parameter $\alpha = 0.001$ and the truncation value $\epsilon = 0.2$.
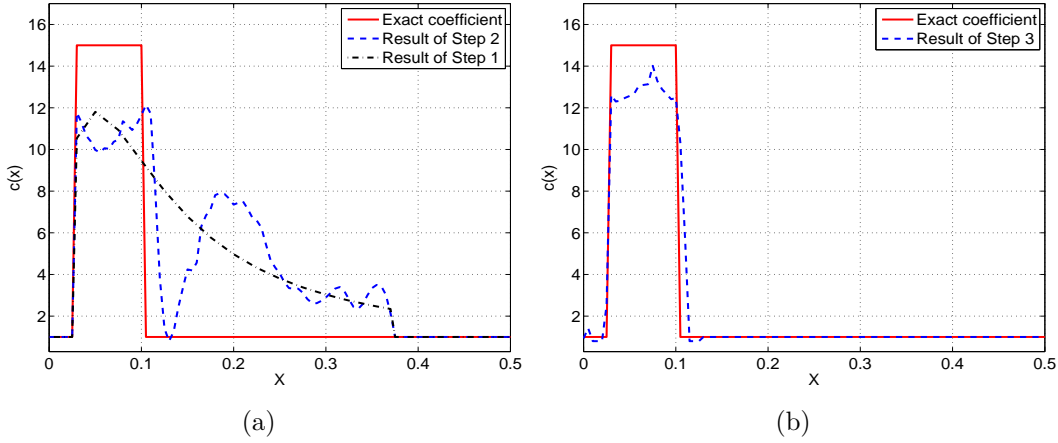


(a)                                    (b)

Figure 25: Reconstruction of the coefficient of Example 2. (a) Result of Steps 1 and 2, (b) Result of Step 3.

**Example 1.** Consider a piecewise constant coefficient given by $c(x) = 1 + 3\chi[0.03, 0.1]$, where $\chi$ is the characteristic function. Figure 24 (a) compares the computed coefficient values of Steps 1 and 2 with the exact one and Figure 24 (b) depicts the result of Step 3. To compare with the performance of the above locally convergent method alone, we plot in Figure 24 (c), (d) the results of Steps 2 and 3, respectively, starting from the homogeneous medium as the initial guess. We can see that our hybrid algorithm provided accurate results, whereas the locally convergent method alone failed.

**Example 2.** In this example, we consider another piecewise constant coefficient with a larger jump $c(x) = 1 + 14\chi[0.03, 0.1]$. The results of Steps 1 - 3 are shown in Figure 25. Even though the jump of the coefficient is high in this case, we still can see the good accuracy of the reconstruction using our hybrid algorithm.

**Example 3.** Consider the exact coefficient $c(x) = 1 - 0.5\chi[0.03, 0.15]$. This coefficient mimics the case the case when the dielectric constant of an explosive is less than the one of a homogeneous background. Figure 26 shows the reconstruction results of Steps 1 - 3 of the algorithm. Again, we obtained an accurate reconstruction.

**Example 4.** Finally, we consider a continuous coefficient given by $c(x) = 1 + 3e^{-(x-0.1)^2/(0.04)^2}$. The results are shown in Figure 27. Comparing Figure 27 (a) with Figure 27 (c), one can see that the combination of Step 1 and Step 2 provided much better result than Step 2 starting
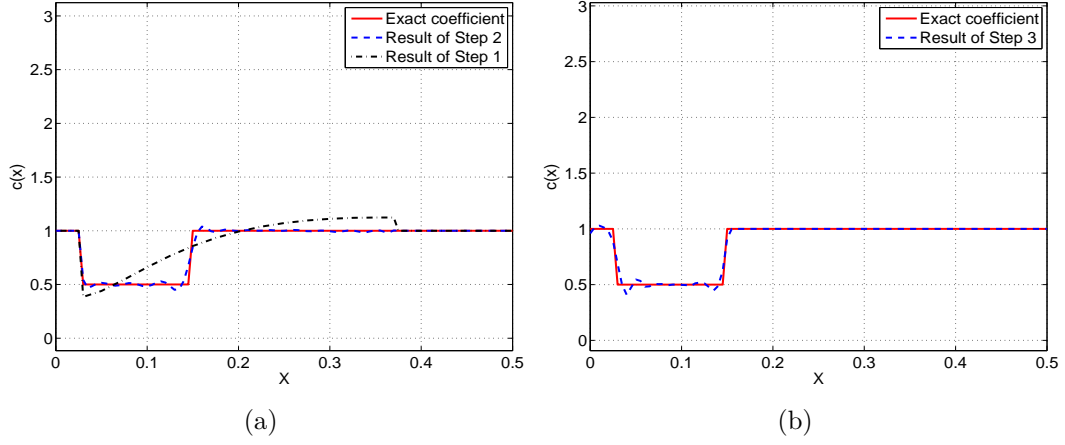
Figure 26: Reconstruction of the coefficient of Example 3. (a) Result of Steps 1 and 2, (b) Result of Step 3.

from the homogeneous medium as the first guess. However, results of Step 3 of both cases are accurate.

From Figure 24 (d) and Figure 27 (d) we see that the above locally convergent method, taking alone, is unstable in the sense that, depending on the type of the target, it provides either bad or good quality images. Meanwhile, the proposed hybrid algorithm provides accurate results in all four examples.
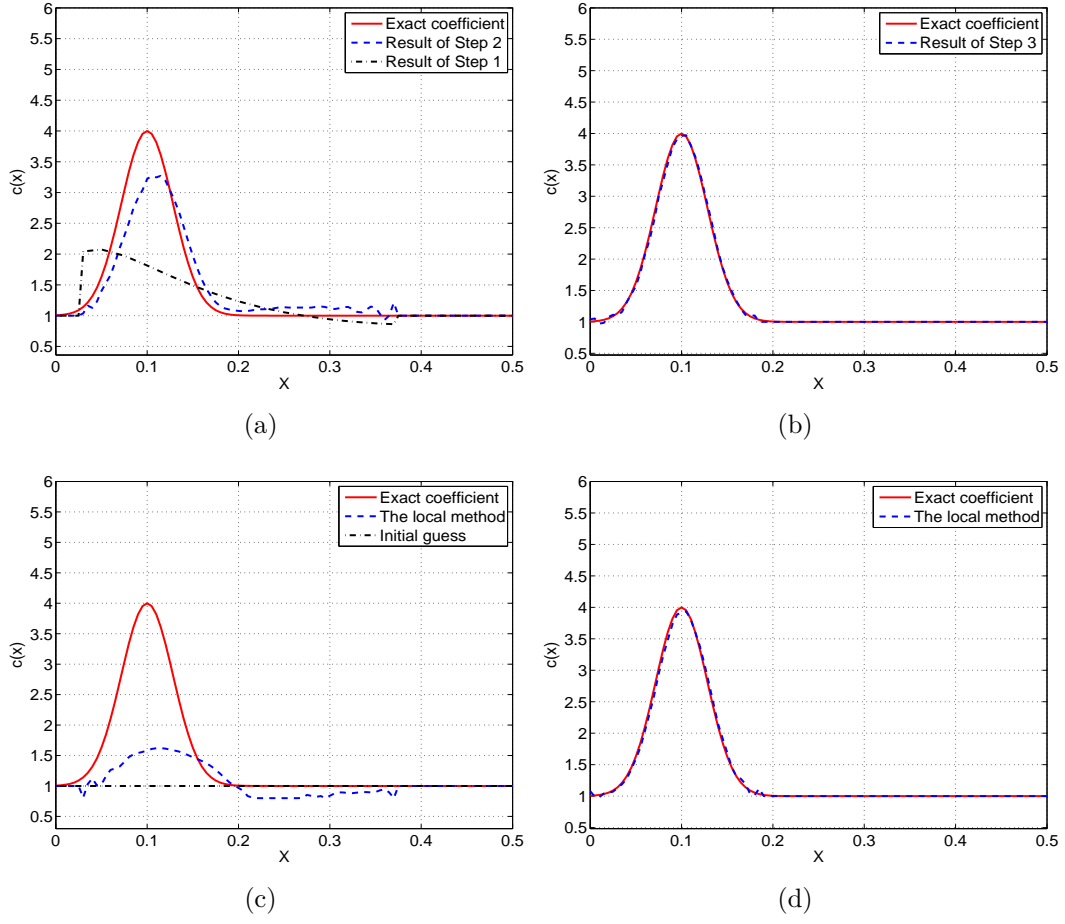
Figure 27: Reconstruction of the coefficient of Example 4. (a) Result of Steps 1 and 2, (b) Result of Step 3, (c) Result of Step 2 starting from the homogeneous medium as the first guess, (d) Result of Step 3 applied to the result of (c).

# 9 The First Solution of a Long Standing Problem [8, 9, 10]

In the paper [8] the PI has solved, for the first time, a long standing problem posed in 1977 by French mathematicians Chadan and Sabatier in their famous book [38]. However, only after the paper [8] was published, the PI has realized that the result of this paper indeed represents the first solution of that problem. Thus, the PI has published a short paper [9], where he has pointed out to this fact. A generalization of the result of [8] to the case of the acoustics equation in $\mathbb{R}^3$ was published in the paper of the PI [10].

When considering Coefficient Inverse Problems in the frequency domain, it was assumed in all previous publications that both the modulus and the phase of the complex valued function representing the wave field is known on a certain set, see, e.g. [60, 61] for global uniqueness results and reconstruction methods. However, in quantum inverse scattering, which is the main interest of the book [38], only the differential cross-section is measured. This means that only the modulus of the scattering wave is measured in quantum inverse scattering. On the other hand, the entire theory of the quantum inverse scattering uses the assumption that both the modulus and the phase of the scattering complex valued wave field are measured. This caused the authors of the book [38] to pose in 1977 in chapter 10 the question about the uniqueness of the inverse scattering problem in the case when only the modulus of the scattering complex valued wave field is measured outside of the scatterer. As it was mentioned above, this question was, for the first time, addressed by the PI in 2014 in [8]. Unlike the current 3-d case, in the past, uniqueness of the phaseless Coefficient Inverse Problem was proven only for the case of the 1-d Schrödinger equation by Klibanov and Sacks in 1992 [53].

Inverse problems without the phase information are well known in optics, since it is often impossible to measure the phase of the optical signal, unlike its amplitude. In optics, such a problem is usually formulated as the problem about the recovery of a compactly supported complex valued function from the modulus of its Fourier transform. The latter is called the "phase retrieval problem" [43, 44]. Uniqueness theorems for the phase retrieval problem can be found in [52, 54, 55].

## 9.1 The first solution of the Chadan-Sabatier problem

Below $C^{s+\alpha}$ are Hölder spaces, where $s \geq 0$ is an integer and $\alpha \in (0,1)$. Let $\Omega, G \subset \mathbb{R}^3$ be two bounded domains, $\Omega \subset G$. For an arbitrary point $y \in \mathbb{R}^3$ and for an arbitrary number $\omega \in (0,1)$ denote $B_\omega(y) = \{x : |x-y| < \omega\}$ and $P_\omega(y) = \mathbb{R}^3 \backslash B_\omega(y)$. For any two sets $M, N \subset \mathbb{R}^3$ let $dist(M, N)$ be the Hausdorff distance between them. Let $G_1 \subset \mathbb{R}^3$ be a convex bounded domain with its boundary $S \in C^1$. Let $\varepsilon \in (0,1)$ be a number. We assume that $\Omega \subset G_1 \subset G$, $dist(S, \partial G) > 2\varepsilon$ and $dist(S, \partial\Omega) > 2\varepsilon$. Hence,

$$dist(\partial B_\varepsilon(y), \partial\Omega) > \varepsilon, \forall y \in S, \tag{106}$$

$$dist(\partial B_\varepsilon(y), \partial G) > \varepsilon, \forall y \in S. \tag{107}$$

Below either $m = 2$ or $m = 4$, and we will specify this later. We impose the following conditions on the potential $q(x)$

$$q(x) \in C^m(\mathbb{R}^3), q(x) = 0 \text{ for } x \in \mathbb{R}^3 \backslash G, \tag{108}$$
$$q(x) \geq 0. \tag{109}$$

Let $x_0 = (x_{0,1}, x_{0,2}, x_{0,3})$ be the source position. Consider the following problem

$$\Delta_x u + k^2 u - q(x) u = -\delta(x - x_0), x \in \mathbb{R}^3, \tag{110}$$

$$\sum_{j=1}^{3} \frac{x_j - x_{j,0}}{|x - x_0|} \partial_{x_j} u(x, x_0, k) - iku(x, x_0, k) = o(1), |x| \to \infty. \tag{111}$$

Here the radiation condition (111) is valid for every fixed source position $x_0$. To establish existence and uniqueness of the solution of the problem (110)-(111), we refer to Theorem 6 of Chapter 9 of the book [68] as well as to Theorem 3.3 of the paper [67]. As to the smoothness of the solution of the problem (110)-(111), we refer to Theorem 6.17 of the book [45]. Thus, combining these results, we obtain that for each pair $(k, x_0) \in \mathbb{R} \times \mathbb{R}^3$ there exists unique solution $u(x, x_0, k)$ of the problem (110), (111) such that

$$u(x, x_0, k) = u_0(x, x_0, k) + u_s(x, x_0, k), \tag{112}$$

$$u_0 = \frac{\exp(ik|x - x_0|)}{4\pi|x - x_0|}, \quad u_s \in C^{m+1+\alpha}(P_\omega(x_0)), \forall \alpha, \omega \in (0, 1). \tag{113}$$

In (112), (113) $u_0(x, x_0, k)$ is the incident spherical wave and $u_s(x, x_0, k)$ is the scattered wave.

**Phaseless Inverse Problem 1 (PIP1).** Let $m = 2$ in (108). Suppose that the function $q(x)$ satisfying (108), (109) is unknown for $x \in \Omega$ and known for $x \in \mathbb{R}^3 \backslash \Omega$. Also, assume that the following function $f_1(x, x_0, k)$ is known

$$f_1(x, x_0, k) = |u(x, x_0, k)|, \forall x_0 \in S, \forall x \in B_\varepsilon(x_0), x \neq x_0, \forall k \in (a, b),$$

where $(a, b) \subset \mathbb{R}$ is an arbitrary interval. Determine the function $q(x)$ for $x \in \Omega$.

We now outline the main difficulty, which did not allow one to prove uniqueness results for phaseless 3-d inverse scattering problems so far. As an example, consider IP1. Analogous difficulties take place all other phaseless Coefficient Inverse Problems formulated in this report. In PIP1 one should work with a complex valued function $r(k), k \in \mathbb{R}$ such that its modulus $|r(k)|$ is known for all $k \in (a, b)$. The function $r(k)$ admits the analytic continuation from the real line $\mathbb{R}$ in the half-plane $\{k \in \mathbb{C} : \operatorname{Im} k > -\gamma\}$ for a certain number $\gamma > 0$. Since $|r(k)|^2 = r(k)\overline{r}(k)$, then the function $|r(k)|^2$ is analytic for $k \in \mathbb{R}$ as the function of the real variable $k$. Here $\overline{r}(k)$ is the complex conjugate of $r(k)$. Hence, the modulus $|r(k)|$ is known for all $k \in \mathbb{R}$. Denote $\mathbb{C}_+ = \{k \in \mathbb{C} : \operatorname{Im} k \geq 0\}$. Proposition 4.2 of [54] implies that if $r(k)$ would not have zeros in $\mathbb{C}_+$, then this function would be uniquely reconstructed for all $k \in \mathbb{R}$ from the values of $|r(k)|$ for $k \in \mathbb{R}$. However, the *main difficulty* is to properly

76

account for zeros of $r(k)$ in the upper half-plane $\mathbb{C}_+\backslash\mathbb{R}$. Indeed, let $z_1, ..., z_n \in \mathbb{C}_+\backslash\mathbb{R}$ be some of such zeros of $r(k)$. Consider the function $\widehat{r}(k)$ defined as

$$\widehat{r}(k) = \left(\prod_{j=1}^{n}\frac{k - \overline{z}_j}{k - z_j}\right)r(k).$$

Hence, $|\widehat{r}(k)| = |r(k)|, \forall k \in \mathbb{R}$. Furthermore, the function $\widehat{r}(k)$ is analytic in the half-plane $\{k \in \mathbb{C} : \operatorname{Im} k > -\gamma\}$. Therefore, in order to prove uniqueness, one needs to figure out how to combine the knowledge of $|r(k)|$ for $k \in \mathbb{R}$ with a linkage between the function $r(k)$ and the originating differential operator.

This difficulty was handled in [53] in the 1-d case, using the fact that the function $r(k)$ depends only on one variable $k$ in this case. Unlike [53], the function $r(x, x_0, k) = u(x, x_0, k)$ depends on $x, x_0, k$ in the 3-d case. Hence, the above zeros depend now on both $x$ and $x_0$, i.e. $z_j = z_j(x, x_0)$. Thus, compared with the 1-d problem, the main difficulty of the 3-d case is that it is necessary to figure out how to take into account the dependence of zeros $z_j(x, x_0)$ from $x$ and $x_0$. To do this, we essentially use here properties of the solution of the Cauchy problem for an associated hyperbolic PDE

$$v_{tt} = \Delta v - q(x)v, (x, t) \in \mathbb{R}^3 \times (0, \infty), \tag{114}$$

$$v(x, 0) = 0, v_t(x, 0) = \delta(x - x_0). \tag{115}$$

Indeed, it follows from Lemma 6 of Chapter 10 of the book [68] as well as to Remark 3 after that lemma that the function $u$ is the Fourier transform of the function $v$,

$$u(x, x_0, k) = \int_0^\infty v(x, x_0, t)e^{ikt}dt, \ \forall x, x_0 \in \mathbb{R}^3, x \neq x_0, \forall k \in \mathbb{R}. \tag{116}$$

**Theorem 9.1.** *Consider PIP1. Let two potentials $q_1(x)$ and $q_2(x)$ satisfying conditions (108), (109) be such that $q_1(x) = q_2(x) = q(x)$ for $x \in \mathbb{R}^3\backslash\Omega$. Let $u_1(x, x_0, k)$ and $u_2(x, x_0, k)$ be corresponding solutions of the problem (110)-(111) satisfying conditions (112), (113). Assume that*

$$|u_1(x, x_0, k)| = |u_2(x, x_0, k)|, \forall x_0 \in S, \forall x \in B_\varepsilon(x_0), x \neq x_0, \forall k \in (a, b). \tag{117}$$

*Then $q_1(x) \equiv q_2(x)$.*

In PIP1 the modulus of the total wave field $u = u_0 + u_s$ is known on a certain set, see (112), (113) for $u_0$ and $u_s$. We now consider the case when only the modulus of the scattered wave is known.

**Phaseless Inverse Problem 2 (PIP2).** Let $m = 2$ in (108). Suppose that the function $q(x)$ satisfying (108), (109) is unknown for $x \in \Omega$ and known for $x \in \mathbb{R}^3\backslash\Omega$. Also, assume that the following function $f_2(x, x_0, k)$ is known

$$f_2(x, x_0, k) = |u_s(x, x_0, k)|, \forall x_0 \in S, \forall x \in B_\varepsilon(x_0), x \neq x_0, \forall k \in (a, b).$$

Determine the function $q(x)$ for $x \in \Omega$.

**Theorem 9.2**. *Consider IP2. Assume that all conditions of Theorem 5.1 hold, except that (117) is replaced with*

$$|u_{s,1}(x, x_0, k)| = |u_{s,2}(x, x_0, k)|, \forall x_0 \in S, \forall x \in B_\varepsilon(x_0), x \neq x_0, \forall k \in (a, b), \quad (118)$$

*where $u_{s,j} = u_j - u_0, j = 1, 2$. In addition, assume that $q(x) \neq 0, \forall x \in S$. Then $q_1(x) \equiv q_2(x)$.*

Theorems 5.1 and 5.2 are formulated only for the over-determined data. Indeed, in both PIP1 and PIP2 the number of free variables in the data exceeds the number of free variables in the unknown coefficient. The reason of this is that even if the phase is known, still all current uniqueness results for 3-d inverse scattering problems in the case when the $\delta-$function is the source function are valid only if the data are over-determined ones, see, e.g. [60, 61] for the frequency domain and §1 of chapter 7 of [56] for an inverse scattering problem in the time domain.

Suppose now that the function $\delta(x - x_0)$ in (110) is replaced with such a function $p(x)$ that $p(x) \neq 0$ in $\overline{\Omega}$. And consider the inverse problem of the reconstruction of the potential $q(x)$ from values of the function $u(x, k)$ for all $x \in S, k \in \mathbb{R}$. Then uniqueness theorem for this problem can be proved for the non-overdetermined case. This proof can be handled by the method, which was introduced in the originating paper [37]. Also, see, e.g. [13] about this method. This technique is based on Carleman estimates.

Consider the function $\chi(x) \in C^\infty(\mathbb{R}^3)$ such that $\chi(x) = 1$ in $G_1$ and $\chi(x) = 0$ for $x \notin G$. Let $x_0 \in S$. For a number $\sigma > 0$ consider the function $\delta_\sigma(x - x_0)$,

$$\delta_\sigma(x - x_0) = C \frac{\chi(x)}{(2\sqrt{\pi\sigma})^3} \exp\left(-\frac{|x - x_0|^2}{4\sigma}\right),$$

where the number $C > 0$ is such that

$$\int_G \delta_\sigma(x - x_0) \, dx = 1.$$

The function $\delta_\sigma(x - x_0)$ approximates the function $\delta(x - x_0)$ in the distribution sense for sufficiently small values of $\sigma$. The function $\delta_\sigma(x - x_0)$ is acceptable in Physics as a proper replacement of $\delta(x - x_0)$, since there is no "true" delta-function in the reality. On the other hand, the above mentioned method of [37] is applicable to the case when $\delta(x - x_0)$ is replaced with $\delta_\sigma(x)$. The function $\delta_\sigma(x - x_0)$ is acceptable in Physics as a proper replacement of $\delta(x - x_0)$, since there is no "true" delta-function in the reality. On the other hand, the above mentioned method of [37] is applicable to the case when $\delta(x - x_0)$ is replaced with $\delta_\sigma(x)$. Therefore, it seems to be worthy from the Physics standpoint to consider Inverse Problems 3,4 below.

Let in (108) $m = 4$. To apply results, which follow from the method of [37], consider the function $g(x)$ such that

$$g \in C^4(\mathbb{R}^3), g(x) = 0 \text{ in } \mathbb{R}^3 \backslash G, \quad (119)$$

$$g(x) \neq 0 \text{ in } \overline{G}_1. \tag{120}$$

Consider the following problem

$$\Delta w + k^2 w - q(x) w = -g(x), x \in \mathbb{R}^3, \tag{121}$$

$$\sum_{j=1}^{3} \frac{x_j}{|x|} \partial_{x_j} w(x,k) - ikw(x,k) = o(1), |x| \to \infty., |x| \to \infty. \tag{122}$$

The same results of [45, 67, 68] as ones cited above in this section guarantee that for each $k \in \mathbb{R}$ there exists unique solution $v(x,k) \in C^{5+\alpha}(\mathbb{R}^3), \forall \alpha \in (0,1)$ of the problem (121), (122).

**Phaseless Inverse Problem 3 (PIP3)**. Let $m = 4$ in (108). Suppose that the function $q(x)$ satisfying conditions (108), (109) is unknown for $x \in \Omega$ and known for $x \in \mathbb{R}^3 \backslash \Omega$. Assume that the following function $f_3(x,k)$ is known

$$f_3(x,k) = |w(x,k)|, \forall x \in S, \forall k \in (a,b). \tag{123}$$

Determine the function $q(x)$ for $x \in \Omega$.

**Theorem 9.3**. *Consider PIP3. Let the function $g(x)$ satisfies conditions (119), (120). Consider two functions $q_1(x), q_2(x)$ satisfying conditions (108), (109) and such that $q_1(x) = q_2(x) = q(x)$ for $x \in \mathbb{R}^3 \backslash \Omega$. For $j = 1, 2$ let $w_j(x,k) \in C^{5+\alpha}(\mathbb{R}^3)$ be the solution of the problem (121)-(122) with $q(x) = q_j(x)$. Assume that*

$$|w_1(x,k)| = |w_2(x,k)|, \forall x \in S, \forall k \in (a,b). \tag{124}$$

*Then $q_1(x) \equiv q_2(x)$.*

We now pose an analog of PIP2. Let $w_0(x,k)$ be the solution of the problem (121)-(122) for the case $q(x) \equiv 0$,

$$w_0(x,k) = \int\limits_{G} \frac{\exp(ik|x - \xi|)}{4\pi |x - \xi|} g(\xi) d\xi.$$

Hence, one can interpret the function $w_0(x,k)$ as the solution of the problem (121)-(122) for case of the background medium.

**Phaseless Inverse Problem 4 (PIP4)**. Let $m = 4$ in (108). Suppose that the function $q(x)$ satisfying (108), (109) is unknown for $x \in \Omega$ and known for $x \in \mathbb{R}^3 \backslash \Omega$. Let $w_s(x,k) = w(x,k) - w_0(x,k)$. Assume that the following function $f_4(x,k)$ is known

$$f_4(x,k) = |w_s(x,k)|, \forall x \in S, \forall k \in (a,b).$$

Determine the function $q(x)$ for $x \in \Omega$.

**Theorem 9.4**. *Consider PIP4. Let all conditions of Theorem 9.3 hold, except that (124) is replaced with*

$$|w_{s,1}(x,k)| = |w_{s,2}(x,k)|, \forall x \in S, \forall k \in (a,b), \tag{125}$$

*where $w_{s,j}(x,k) = w_j(x,k) - w_0(x,k), j = 1, 2$. Assume that $q(x) \neq 0, \forall x \in S$. Then $q_1(x) \equiv q_2(x)$.*

## 9.2 Uniqueness of some phaseless coefficient inverse problems for the acoustic equation in 3D

We now formulate uniqueness theorems of the paper [10] for some phaseless inverse problems for the 3D acoustics equation. The main difficulty of proofs of these theorems is the same as the one indicated in section 5.3.2 for the case of the Schrödinger equation. We keep notations of the previous section for domains and surfaces.

Let $c(x)$ be the variable sound speed satisfying the following conditions

$$c \in C^5\left(\mathbb{R}^3\right), c(x) = 1 \text{ for } x \in \mathbb{R}^3 \backslash G, \tag{126}$$

$$c(x) \geq c_0 = const. > 0, \forall x \in G. \tag{127}$$

In addition, we assume that there exists a point $x_0 \in \Omega$ such that

$$\left(x - x_0, \nabla c^{-2}(x)\right) \geq 0, \forall x \in \overline{G}. \tag{128}$$

Condition (128) can be interpreted as the monotonicity condition of the function $c^{-2}(x)$ along rays of straight lines passing through the point $\{x_0\}$, and $\{x_0\}$ is the beginning of any such ray. We use (128) quite essentially. First, we use it in Lemma 1. This lemma is applied, in turn to establish the exponential decay with respect to the time $t$ of the solution of the Cauchy problem for the acoustic equation in the time domain using results of the book [68]. Second, (128) guarantees the existence of the Carleman estimate for the operator $\partial_t^2 - c^2(x)\Delta$, see Theorem 2.6 in [13]. This Carleman estimate, in turn allows us to apply Theorem 3.1 of [13] in the final step of the proof of Theorems 9.5 and 9.6 below.

**Lemma**. *Assume that conditions (126)-(128) are in place. Then the family of geodesic lines generated by the function $c(x)$ satisfies the non-trapping property in $\mathbb{R}^3$.*

Consider the function $g(x)$ satisfying the following conditions

$$g \in C^7\left(\mathbb{R}^3\right), g(x) = 0 \text{ in } \mathbb{R}^3 \backslash G, \tag{129}$$

$$g(x) \neq 0, x \in S. \tag{130}$$

$$\Delta g(x) \neq 0, \forall x \in \overline{G}_1. \tag{131}$$

Let the number $k \in \mathbb{R}$. Consider the following problem

$$\Delta u + \frac{k^2}{c^2(x)}u = -g(x), x \in \mathbb{R}^3, \tag{132}$$

$$\sum_{j=1}^3 \frac{x_j}{|x|}\partial_{x_j}u(x, k) - iku(x, k) = o(1), |x| \to \infty. \tag{133}$$

Equation (132) is the acoustic equation in the frequency domain. Just as in the previous section 5.3.2, we now refer to Theorem 6 of Chapter 9 of the book [68], Theorem 3.3 of the paper [67] as well as to Theorem 6.17 of the book [45]. Combining these results with Lemma,

we obtain that for each $k \in \mathbb{R}$ there exists unique solution $u(x, k) \in C^{6+\alpha}(\mathbb{R}^3), \forall \alpha \in (0, 1)$ of the problem (132), (133).

**Phaseless Inverse Problem 5 (PIP5).** Suppose that the function $c(x)$ satisfying conditions (126)-(128) is unknown for $x \in \Omega$ and known for $x \in \mathbb{R}^3 \backslash \Omega$. Assume that the following function $f_5(x, k)$ is known

$$f_5(x, k) = |u(x, k)|, \forall x \in S, \forall k \in (a, b). \tag{134}$$

Determine the function $c(x)$ for $x \in \Omega$.

**Theorem 9.5**. *Consider PIP5. Let the function $g(x)$ satisfies conditions (129)-(131). Consider two functions $c_1(x), c_2(x)$ satisfying conditions (126)-(128) and such that $c_1(x) = c_2(x) = c(x)$ for $x \in \mathbb{R}^3 \backslash \Omega$. For $j = 1, 2$ let $u_j(x, k) \in C^{6+\alpha}(\mathbb{R}^3), \forall \alpha \in (0, 1)$ be the solution of the problem (132), (133) with $c(x) = c_j(x)$. Assume that*

$$|u_1(x, k)| = |u_2(x, k)|, \forall x \in S, \forall k \in (a, b). \tag{135}$$

*Then $c_1(x) \equiv c_2(x)$.*

IP1 is about the case when the modulus of the total wave field is measured for $x \in S, k \in (a, b)$. Consider the function $u_0(x, k)$,

$$u_0(x, k) = \int\limits_{G} \frac{\exp(ik |x - \xi|)}{4\pi |x - \xi|} g(\xi) \, d\xi.$$

This function is the solution of the problem (132), (133) for the case $c(x) \equiv 1$. Since $c(x) = 1$ for $x \in \mathbb{R}^3 \backslash G$, then one can consider $u_0(x, k)$ as the solution of the problem (132), (133) for the background medium. Hence, the function $u_s(x, k) = u(x, k) - u_0(x, k)$ can be considered as the wave, which is scattered due to the inhomogeneous structure of the coefficient $c(x)$ for $x \in G$. This is our motivation for posing Phaseless Inverse Problem 6.

**Phaseless Inverse Problem 6 (PIP6).** Suppose that the function $c(x)$ satisfying conditions (126)-(128) is unknown for $x \in \Omega$ and known for $x \in \mathbb{R}^3 \backslash \Omega$. Let $u_s(x, k) = u(x, k) - u_0(x, k)$. Assume that the following function $f_6(x, k)$ is known

$$f_6(x, k) = |u_s(x, k)|, \forall x \in S, \forall k \in (a, b).$$

Determine the function $c(x)$ for $x \in \Omega$.

**Theorem 9.6**. *Consider PIP6. Assume that*

$$c^2(x) \neq 1, \forall x \in S.$$

*Let all conditions of Theorem 5.5 hold, except that (130) is not imposed. In addition, let (135) be replaced with*

$$|u_{s,1}(x, k)| = |u_{s,2}(x, k)|, \forall x \in S, \forall k \in (a, b),$$

*where $u_{s,j}(x, k) = u_j(x, k) - u_0(x, k), j = 1, 2$. Then $c_1(x) \equiv c_2(x)$.*

# 10   Presentations

Below is the list of our presentations of above results during the reportage period.

**A. Presentations to engineers of the Army Research Laboratory (ARL):**

1. Presentation at the Army Research Laboratory (ARL) to Mr. Brian Burns, an engineer of ARL, Dr. Joseph D. Myers, Program Manager of Numerical Analysis Program of ARO and to Drs. Anders Sullivan and Lam Nguyen, engineers of RF Signal Processing and Modeling Branch of Sensors and Electron Devices Directorate of ARL and to (2012).

2. Presentation to Mr. Brian Burns and to Dr. Joseph D. Myers during their visit of our campus (2012).

3. Presentation to Drs. Joseph D. Myers and Anders Sullivan during their visit of our campus (2012).

4. Presentation over the phone to Mr. Brian Burns and Drs. Joseph D. Myers and Anders Sullivan (2013).

**B. Other presentations:**

1. Colloquium talk at Department of Mathematical Sciences of University of Delaware.

2. Colloquium talk at Department of Mathematics of University of Virginia.

3. Colloquium talk at Department of Mathematics of Georgia Institute of Technology.

4. Colloquium talk at Department of Mathematics of Wichita State University (Wichita, Kansas).

5. Inverse Problems workshop in Ecole Polytechnique, Paris.

6. Plenary speaker at the conference: "Inverse Problems Problems: Modelling and Simulation", Turkey.

7. Plenary speaker at the conference on Inverse Problems, Albi, France.

8. Conference "Applied Inverse Problems", Korea, organizer of a minisimposium and presenter of a talk.

9. Presentation at the Conference dedicated to the 30st anniversary of the journal "Inverse Problems", Bristol, UK.

10. Presentation at the 6th International Conference on Advanced Computational Methods in Engineering, Gent, Belgium.

11. Plenary speaker at International Conference on Inverse Problems and Optimal Control, Hong Kong.

# 11 Book and Survey Papers

The book [1] is published by Springer, the World most prestigious publisher of the scientific literature. Results of Beilina and Klibanov since their first joint publication [25] in 2008 and up to 2012 are summarized there. The book discusses both the theory and numerical studies of the globally convergent numerical method of section 3 and of the adaptivity of section 4. Although this book was published only two years ago, it was cited more than 97 times by now, see

http://scholar.google.com/citations?user=pFmp7LMAAAAJ&hl=en.

The paper [7] is the survey of the relaxation property for the adaptivity technique (section 4) . The paper [13] is the survey on the applications of Carleman estimates to inverse problems, starting from the work [37] in 1981. It is worthy to point out that both globally convergent numerical methods for CIPs, presented above, have roots in the idea of [37]. Currently there are more than 50 publications of authors, other than the ones of [37], which cite this paper. In accordance with

http://scholar.google.com/citations?user=pFmp7LMAAAAJ&hl=en,

the paper [37] was cited more than 314 times.

# 12 Publications

Publications [1]-[23] acknowledge the support of this grant. The paper [27] is a featured article of *Inverse Problems.*

# References

[1] L. Beilina and M.V. Klibanov, *Approximate Global Convergence and Adaptivity for Coefficient Inverse Problems*, Springer, New York, 2012.

[2] L. Beilina, N.T. Thanh, M.V. Klibanov and M.A. Fiddy, Reconstruction from blind experimental data for an inverse problem for a hyperbolic equation, *Inverse Problems*, 30, 025002, 2014.

[3] L. Beilina, N.T. Thanh, M.V. Klibanov and J.B. Malmberg, Reconstruction of shapes and refractive indices from backscattering experimental data using the adaptivity, *Inverse Problems*, accepted for publication, available online, *arxiv:* 1404.5862v1, 2014.

[4] N.T. Thành, L. Beilina, M.V. Klibanov and M.A. Fiddy, Reconstruction of the refractive index from experimental backscattering data using a globally convergent inverse method, *SIAM J. Sci. Comp.*, 36, B273-B293, 2014.

[5] N. T. Thành, L. Beilina, M. V. Klibanov, and M. A. Fiddy, Imaging of buried objects from experimental backscattering radar measurements using a globally convergent

inverse method, *arxiv*: 1406.3500v1, submitted for publication in *SIAM J. Imaging Sciences*, 2014.

[6] L. Beilina, N.T. Thành, M.V. Klibanov and J.B. Malmberg, Methods of quantitative reconstruction of shapes and refractive indexes from experimental data, Proceedings: *Inverse Problems and Applications*, published by Springer, to appear in 2014.

[7] L. Beilina and M.V. Klibanov, Relaxation property for the adaptivity for ill-posed problems, *Applicable Analysis*, 93, 223-253, 2014.

[8] M.V. Klibanov, Phaseless inverse scattering problems in three dimensions, *SIAM J. Appl. Math.*, 74, 392-410, 2014.

[9] M.V. Klibanov, On the first solution of a long standing problem: uniqueness of the phaseless quantum inverse scattering problem in 3-d, *Applied Mathematics Letters*, 47, 82-85, 2014.

[10] M.V. Klibanov, Uniqueness of two phaseless non-overdetermined inverse acoustics problems in 3-d, *Applicable Analysis*, 93, 1135-1149, 2014.

[11] M.V. Klibanov and N.T. Thành, Recovering of dielectric constants of explosives via a globally strictly convex cost functional, *arxiv*: 1408.0583v1, 2014, submitted for publication to *SIAM J. Appl. Math.*

[12] L. Beilina and M.V. Klibanov, Globally strongly convex cost functional for a coefficient inverse problem, accepted for publication in *Nonlinear Analysis-B: Real World Applications*, 2014, *arxiv*: 1313.2886v1.

[13] M.V. Klibanov, Carleman estimates for global uniqueness, stability and numerical methods for coefficient inverse problems, survey, *J. Inverse and Ill-Posed Problems*, 21, 477-560, 2013.

[14] M.V. Klibanov, Thermoacoustic tomography with an arbitrary elliptic operator, *Inverse Problems,* 29, 025014, 2013.

[15] J. Su, M.V. Klibanov, Y. Liu, Z. Lin, N. Pantong and H. Liu, Optical imaging of phantoms from real data by an approximately globally convergent inverse algorithm, *Inverse Problems in Science and Engineering,* 21, 1125-1150, 2013.

[16] L. Beilina and M.V. Klibanov, A new approximate mathematical model for global convergence for a coefficient inverse problem with backscattering data, *J. Inverse and Ill-Posed Problems*, 20, 513-565, 2012.

[17] A.V. Kuzhuget, L. Beilina, M.V. Klibanov, A. Sullivan, L. Nguyen and M.A. Fiddy, Blind experimental data collected in the field and an approximately globally convergent inverse algorithm, *Inverse Problems*, 28, 095007, 2012.

[18] A.V. Kuzhuget, L. Beilina, M.V. Klibanov, A. Sullivan, L. Nguyen and M.A. Fiddy, Quantitative image recovery from measured blind backscattered data using a globally convergent inverse method, *IEEE Transactions of Geoscience and Remote Sensing*, 51, 2937-2948, 2013.

[19] A.L. Karchevskii, M.V. Klibanov, N. Pantong, A. Sullivan and L. Nguyen, The Krein method and the globally convergent method for experimental data, *Applied Numerical Mathematics*, 74, 111-127, 2013.

[20] L. Beilina and M.V. Klibanov, The philosophy of the approximate global convergence for multidimensional coefficient inverse problems, *Complex Variables and Elliptic Equations*, 57, 277-299, 2012.

[21] A.V. Kuzhuget, L. Beilina and M.V. Klibanov, Approximate global convergence and quasi-reversibility for a coefficient inverse problem with backscattering data, *J. Mathematical Sciences*, 181, 126-163, 2012.

[22] L. Beilina and M.V. Klibanov, Approximate global convergence in imaging of land mines from backscattering data, *Springer Proceedings in Mathematics*, 23 pages, 2012.

[23] L. Beilina and M.V. Klibanov, Adaptive FEM with relaxation for a hyperbolic coefficient inverse problem, *Springer Proceedings in Mathematics,* 24 pages, 2012.

[24] M. Abramowitz and I. A. Stegun, *Handbook of Mathematical Functions with Formulas, Graphs, and Mathematical Tables*, volume 55 of *National Bureau of Standards Applied Mathematics Series*. 1964.

[25] L. Beilina and M. V. Klibanov, A globally convergent numerical method for a coefficient inverse problem, *SIAM Journal on Scientific Computing*, 31, 382–402, 2008.

[26] M.V. Klibanov, A.B. Bakushinskii and L. Beilina, Why a minimizer of the Tikhonov functional is closer to the exact solution than the first guess, *J. Inverse and Ill-Posed Problems*, 19, 83-105, 2011.

[27] L. Beilina and M.V. Klibanov, Reconstruction of dielectrics from experimental data via a hybrid globally convergent/adaptive inverse algorithm, *Inverse Problems*, 26, 125009, 2010.

[28] L. Beilina, M.V. Klibanov and M.Yu. Kokurin, Adaptivity with relaxation for ill-posed problems and global convergence for a coefficient inverse problem, *Journal of Mathematical Sciences,* 167, 279-325, 2010.

[29] L. Beilina, Energy estimates and numerical verification of the stabilized domain decomposition finite element/finite difference approach for the Maxwell's system in time domain, *Central European Journal of Mathematics*, 11, 702-733, 2013.

[30] R. Becker and R. Rannacher, An optimal control approach to *a posteriori* error estimation in finite element method, *Acta Numerica*, 10, 1-102, 2001.

[31] L. Beilina and C. Johnson, A hybrid FEM/FDM method for an inverse scattering problem. In *Numerical Mathematics and Advanced Applications - ENUMATH 2001*, Springer-Verlag, Berlin, 2001.

[32] L. Beilina, Adaptive finite element/difference method for inverse elastic scattering waves, *Applied and Computational Mathematics*, 1, 158-174, 2002.

[33] L. Beilina and C. Johnson, *A posteriori* error estimation in computational inverse scattering, *Mathematical Models and Methods in Applied Sciences*, 15, 23-37, 2005.

[34] L. Beilina and C. Clason, An adaptive hybrid FEM/FDM method for an inverse scattering problem in scanning acoustic microscopy, *SIAM J. Sci. Comp.*, 28, 382-402, 2006.

[35] L. Beilina, Adaptive finite element method for a coefficient inverse problem for the Maxwell's system, *Applicable Analysis*, 90, 1461-1479, 2011.

[36] A.S. Blagoveshenskii, On a local method of solving a non-stationary inverse problem for inhomogeneous string, *Proceedings of Mathematical Steklov Institute* 115, 28-38, 1971.

[37] A.L. Bukhgeim and M.V. Klibanov, Uniqueness in the large of a class of multidimensional inverse problems, *Sov. Math. Dokl.*, 17, 244-247, 1981.

[38] K. Chadan and P.C. Sabatier, *Inverse Problems in Quantum Scattering Theory*, Springer, New York, 1977.

[39] H.T. Chuah, K.Y. Lee and T.W. Lau, Dielectric constants of rubber and oil palm leaf samples at X-band, *IEEE Trans. on Geoscience and Remote Sensing,* 33, 221-223, 1995.

[40] H.W. Engl, M. Hanke and A. Neubauer, *Regularization of Inverse Problems*, Kluwer Academic Publishers, Boston, 2000.

[41] E. Farr and C. Frost. Impulse propagation measurements of dielectric properties of water, dry sand, moist sand and concrete. 1997. *Measurement Note* 52. Farr Research.

[42] K. Eriksson, D. Estep and C. Johnson, *Calculus in Several Dimensions*, Springer, Berlin, 2004.

[43] J.R. Fienup, Phase retrieval algorithms: a personal tour [invited], *Applied Optics*, 52, 45-56, 2013.

[44] J.R. Fienup, J.C. Maron, T.J. Schulz and J.H. Seldin, Hubble space telescope characterization by using phase retrieval algorithms, *Applied Optics*, 32, 1747-1768, 1993.

[45] D. Gilbarg and N.S. Trudinger, *Elliptic Partial Differential Equations of Second Order*, Springer, New York, 1984.

[46] S. I. Kabanikhin and M.A. Shishlenin, Boundary control and Gel'fand-Levitan-Krein methods in inverse acoustic problem, *J. Inverse and Ill-Posed Problems* 12, 125-144, 2004.

[47] V. Isakov, Inverse obstacle problems, *Inverse Problems*, 25,123002, 2009.

[48] M. V. Klibanov and A. Timonov, *Carleman Estimates for Coefficient Inverse Problems and Numerical Applications*, VSP, Utrecht, 2004.

[49] M.V. Klibanov, Global convexity in a three-dimensional inverse acoustic problem, *SIAM J. Math. Analysis*, 28, 1371-1388, 1997.

[50] M.V. Klibanov, Global convexity in diffusion tomography, *Nonlinear World*, 4, 247-265, 1997.

[51] M.G. Krein, A method of efficient solution of an inverse boundary value problem, *Dokl. Acad. Nauk USSR,* 94, 1954, 987-990.

[52] M.V. Klibanov, Determination of a function with compact support from the absolute value of its Fourier transform, and an inverse scattering problem, *Differential Equations*, 22, 1232-1240, 1987.

[53] M.V. Klibanov and P.E. Sacks, Phaseless inverse scattering and the phase problem in optics, *J. Math. Physics*, 33, 3813-3821, 1992.

[54] M.V. Klibanov, P.E. Sacks and A.V. Tikhonravov, The phase retrieval problem. Topical Review. *Inverse Problems*, 11, 1-28, 1995.

[55] M.V. Klibanov, On the recovery of a 2-D function from the modulus of its Fourier transform, *J. Mathematical Analysis and Applications*, 323, 818-843, 2006.

[56] M.M. Lavrentiev, V.G. Romanov and S.P. Shishatskii, *Ill-Posed Problems of Mathematical Physics and Analysis*, AMS, Providence, R.I., 1986.

[57] O.A. Ladyzhenskaya, *Boundary Value Problems of Mathematical Physics*, Springer, New York, 1985.

[58] B.M. Levitan, *Inverse Sturm-Liouville Problems*, VSP, Utrecht, The Netherlands, 1987.

[59] L. Nguyen, D. Wong, M. Ressler, F. Koenig, B. Stanton, G. Smith, J. Sichina and K. Kappra, Obstacle avoidance and concealed target detection using the Army Research Lab ultra-wideband synchronous impulse Reconstruction (UWB SIRE) forward imaging radar, *Proc. SPIE,* 6553, 65530H (1)-65530H (8), 2007.

[60] R.G. Novikov, The inverse scattering problem on a fixed energy level for the two-dimensional Schrödinger operator, *J. Functional Analysis*, 103, 409-463, 1992.

[61] R.G. Novikov, $\partial-$bar approach to approximate inverse scattering at fixed energy in three dimensions, *International Math. Research Peports*, 6, 287-349, 2005.

[62] A. Sentenac, H. Giovannini, and M. Saillard, Scattering from rough inhomogeneous media: splitting of surface and volume scattering. *J. Opt. Soc. Am. A*, 19, 727–736, 2002.

[63] F. Simonetti, Localization of pointlike scatterers in solids with subwavelength resolution, *Applied Physics Letter*, 89, 094105, 2006.

[64] R. Stolt, Migration by fourier transform. *Geophysics*, 43:23–48, 1978.

[65] Tables of dielectric constants at http://www.asiinstr.com/technical/Dielectric0Constants.htm.

[66] Tables of dielectric constants at http://www.krohne.com/Dielectric_Constants.6840.0.html.

[67] B.R. Vainberg, Principles of radiation, limiting absorption and limiting amplitude in the general theory of partial differential equations, *Russian Math. Surveys*, 21, 115-193, 1966.

[68] B.R. Vainberg, *Asymptotic Methods in Equations of Mathematical Physics*, Gordon and Breach Science Publishers, New York, 1989.

[69] O. Yilmaz. *Seismic Data Imaging.* Society of Exploration Geophysicists, Tulsa Oklahoma, 1987.